

1999

Thermoelastic and photoelastic full-field stress measurement

Deonna Faye Woolard

College of William & Mary - Arts & Sciences

Follow this and additional works at: <https://scholarworks.wm.edu/etd>



Part of the [Condensed Matter Physics Commons](#), and the [Electromagnetics and Photonics Commons](#)

Recommended Citation

Woolard, Deonna Faye, "Thermoelastic and photoelastic full-field stress measurement" (1999).

Dissertations, Theses, and Masters Projects. Paper 1539623969.

<https://dx.doi.org/doi:10.21220/s2-x5mm-jq08>

This Dissertation is brought to you for free and open access by the Theses, Dissertations, & Master Projects at W&M ScholarWorks. It has been accepted for inclusion in Dissertations, Theses, and Masters Projects by an authorized administrator of W&M ScholarWorks. For more information, please contact scholarworks@wm.edu.

INFORMATION TO USERS

This manuscript has been reproduced from the microfilm master. UMI films the text directly from the original or copy submitted. Thus, some thesis and dissertation copies are in typewriter face, while others may be from any type of computer printer.

The quality of this reproduction is dependent upon the quality of the copy submitted. Broken or indistinct print, colored or poor quality illustrations and photographs, print bleedthrough, substandard margins, and improper alignment can adversely affect reproduction.

In the unlikely event that the author did not send UMI a complete manuscript and there are missing pages, these will be noted. Also, if unauthorized copyright material had to be removed, a note will indicate the deletion.

Oversize materials (e.g., maps, drawings, charts) are reproduced by sectioning the original, beginning at the upper left-hand corner and continuing from left to right in equal sections with small overlaps.

Photographs included in the original manuscript have been reproduced xerographically in this copy. Higher quality 6" x 9" black and white photographic prints are available for any photographs or illustrations appearing in this copy for an additional charge. Contact UMI directly to order.

**Bell & Howell Information and Learning
300 North Zeeb Road, Ann Arbor, MI 48106-1346 USA
800-521-0600**

UMI[®]

**THERMOELASTIC AND PHOTOELASTIC FULL-FIELD
STRESS MEASUREMENT**

A Dissertation

Presented to

**The Faculty of the Department of Physics
The College of William & Mary in Virginia**

In Partial Fulfillment

**Of the Requirements for the Degree of
Doctor of Philosophy**

By

Deonna Faye Woolard

1999

UMI Number: 9975024



UMI Microform 9975024

Copyright 2000 by Bell & Howell Information and Learning Company.

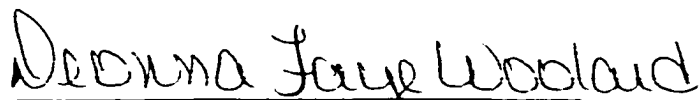
All rights reserved. This microform edition is protected against
unauthorized copying under Title 17, United States Code.

Bell & Howell Information and Learning Company
300 North Zeeb Road
P.O. Box 1346
Ann Arbor, MI 48106-1346

APPROVAL SHEET


This dissertation is submitted in partial fulfillment of
the requirements for the degree of

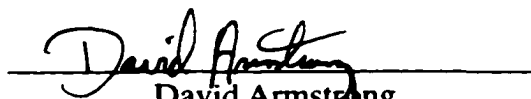
Doctor of Philosophy


Deonna Faye Woolard

Approved, July 1999


Mark Hinder (Advisor)


Gina Hoatson


David Armstrong


Anne Reilly

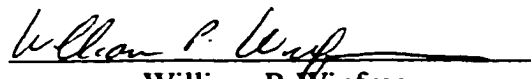

William P. Winfree
(NASA)

Table of Contents

Acknowledgments	v
List of Tables	vi
List of Figures	vii
Abstract	xi
Chapter 1 Introduction	2
1.1 History of Photoelasticity	2
1.2 History of Thermoelasticity	22
1.1.1 Design of the Polariscope	5
1.1.2 Advances in Photoelastic Analysis	10
1.3 Motivation to Combine Thermo- and Photoelasticity	32
1.4 Dissertation overview	34
Chapter 2 Photo-Thermoelastic Coating	35
2.1 Measurement Systems Overview	35
2.2 Coating Characteristics	38
2.3 Dual-Use Coating	43
2.4 Reflective Backing	48
Chapter 3 Photoelastic Theories	54
3.1 One-Dimensional Theory	54

3.2 Modern Optics	58
3.3 Electromagnetic Wave Theory	62
3.4 Electromagnetic Wave Theory	62
Chapter 4 Anisotropic Electromagnetic Boundary Value Problem	68
4.1 Isoclinic Model	68
4.2 Ischromatic Model	76
4.3 Experimental Versus Theoretical Comparison	80
4.4 Combining Thermoelasticity and Photoelasticity	91
Chapter 5 Depolarization of Electromagnetic Waves	100
5.1 The Rayleigh Criterion	101
5.2 Optical Analysis of the Reflective Backings	102
5.3 Depolarization by Scattering from Random Rough Surfaces	106
5.3.1 Depolarization of Isoclinic Fringes	113
5.3.2 Depolarization of Isochromatic Fringes	123
Chapter 6 Summary and Future Direction	128
Appendix A Fresnel's Equation	133
Appendix B Definition of Roughness	136
Appendix C Derivation of the Thermoelastic Equation	140
Bibliography	145
Vita	154

Acknowledgments

I would like to express my appreciation to Mark Hinders for his guidance, insight, and enthusiasm for this project. Our collaboration has allowed me to grow intellectually as well as professionally. I would also like to thank the members of my committee for their comments on this document. I am also indebted to Elliott Cramer, Mike Seale, Dan Perey, and Patty Howell of the NASA Langley Research Center in Hampton, Virginia. Your assistance to this project was invaluable.

I wish to express my thanks to the Physics Department at William and Mary. I have enjoyed, as well as benefited, from my interactions with the faculty and staff. I would have never been able maintain my student status without the assistance of Paula, Dianne, and Sylvia. Thank you for your guidance as well as the enjoyable conversations throughout the years. I would also like to acknowledge Ed, Mel, Kirk, and John. You all have been extremely helpful. You were never too busy to take a question or give me some help.

To my roommate of five years, Megan. Thank you for being such a wonderful friend for so many years. Your enthusiasm and cheerfulness have kept me going through some difficult times. My memories of graduate school are filled with our many adventures. To Julie, thank you for the many lunch time conversations where I was reminded of the many wonderful things that life has to offer. To all my other friends that I have met through the department -- Marco, Al, Justin, Doug, Peko, Scott, April, Chree, Ellen, Mike, and Renee, among them. Thanks so much for all of the great times that we have had together. I would also like to express my appreciation to my volleyball and softball teammates at the Williamsburg and James City County Recreational Centers. You allowed me to run off my frustrations and yet, still asked me to come back for the next game. I could have never remained sane without our interactions.

Finally, I would like to express my most sincere appreciation to my family. Thanks Mom, Dad, Jen, Aunt Donna, Uncle Barry, and Aunt Faye for believing in me. Mom and Dad, I have reached this point in my life because of your love, guidance, inspiration, and discipline. I love you! And finally to my husband, Joe. You have been the sunshine in my life and have given me the confidence and strength to finish this project. Words do not begin to express my love for you and the goodness that you bring out in me.

List of Tables

2.1 - Optical properties of some common polymers.	39
5.1 - Stress tensor components subjected to variations in angle.	122
5.2 - Stress tensor components subjected to variations in stresses.	125
5.3 - Stress tensor components with errors in the angle and stresses	127

List of Figures

1.1	Present day version of the Coker polariscope. Pictured above is the Measurements Group, Inc. Model 030 Polariscope in front of a hydraulic load frame	8
2.1	Isoclinic (a) and isochromatic (b) photoelastic images for a hole in a PMMA plate under vertical tension taken with the Model 030 Polariscope.. . . .	36
2.2	Theoretical plot of the amplitude response of a sample coated with black paint as a function of frequency. Notice the fall-off region as the frequency increases. At high frequencies the amplitude from the sample is completely damped-out in the coating. The remaining signal is the response of the coating reacting to the applied strain.	41
2.3	Thermoelastic (a) and photoelastic (b) responses from a polycarbonate sheet with a central hole under vertical tension.. . . .	45
2.4	Thermoelastic (a) and photoelastic (b) responses from a PMMA bar with a central hole under vertical tension.	46
2.5	Various surfaces subjected to polarized light and observed through an analyzer that is (a) parallel and (b) perpendicular to the incident light. Material list given in the text.	49
2.6	Ratio of the parallel to perpendicular polarization pixel values for reflection of surfaces 1 - 9. The industry standard is denoted by the dashed line for comparison.	50
3.1	Plane Polariscope [114].	56
3.2	Circular Polariscope [114].	57
3.3	Optical indicatrix ellipsoid intersected by a plane perpendicular to the propagation vector \mathbf{k} forming an ellipse. The principal semiaxes of the ellipse coincide with \mathbf{D}_1 and \mathbf{D}_2 and are proportional to the indices of refraction n_1 and n_2 [115].	60

3.4	The kDB system as related to the cartesian axes [116].	65
4.1	Set-up for the isoclinic model.. . . .	69
4.2	Propagating waves associated with the isoclinic and isochromatic theoretical models.	71
4.3	Set-up for the isochromatic model. The quarter-wave plates have a coordinate system that is rotated 45° from the lab system. The fast axis (F) denotes the component of the wave that will lead by a phase of 90°	77
4.4	Relation between the quarter-wave plate axes and the material coordinate system.. . . .	78
4.5	Flow chart for the theoretical calculation of the photoelastic fringes.	82
4.6	Comparison of (a) experimental versus (b) theoretical photoelastic fringe pattern for a hole in a plate under vertical tension. The experimental image was obtained with the model 030-polariscope and the theoretical image was calculated from the Kirsch problem.	83
4.7	A typical stress contour image for a FEA model of a hole in plate under uniaxial tension: (a) T_x , (b) T_y , and (c) T_{xy} . A color legend would accompany each image for the conversion of color to stress level.	84
4.8	Comparison of (a) experimental versus (b) theoretical photoelastic fringe pattern for a hole in a PMMA plate under vertical tension. The theoretical image was calculated using Finite Element Analysis	86
4.9	Comparison of (a) experimental versus (b) theoretical photoelastic fringe patterns for a hole with a notch in a PMMA plate under vertical tension. The theoretical image was calculated using Finite Element Analysis.	87
4.10	Comparison of (a) experimental versus (b) theoretical photoelastic fringe pattern for two identical holes in a PMMA plate under vertical tension. The theoretical image was calculated using Finite Element Analysis. The experimental image (a) shows the reflection of the light source in the upper right corner.	88
4.11	Comparison of (a) experimental versus (b) theoretical photoelastic fringe pattern for two different sized holes in a PMMA plate under vertical tension. The theoretical image was calculated using Finite Element Analysis. The experimental image (a) shows the reflection of the light source in the upper right corner	89

4.12	Comparison of (a) experimental versus (b) theoretical photoelastic fringe pattern a hole in a plate under vertical tension. The stresses for the theoretical image were calculated from the Kirsch problem.	90
4.13	(a) Experimental versus (b) theoretical isochromatic fringes for a hole in a plate under uniaxial tension at 400 pounds. The stresses for the theoretical images were calculated using FEA.	92
4.14	Thermoelastic phase images for a PMMA plate with (a) one hole and (b) two holes under vertical tension. The tops and bottoms of the holes exhibit a different phase from the rest of the sample due to cyclic loading.	95
4.15	Isoclinic lines for a hole in a plate under vertical tension. The angles correspond to the rotation of the polarizer/analyzer about the z axis in the laboratory system [123].	97
4.16	(a) General construction of isostatic lines from isoclinic lines used to visualize the (b) stress trajectories for a hole in a plate under vertical tension. Stress trajectories are at the top of (b) and isoclinic lines at the bottom [123].	97
4.17	Sixty pixels of thermoelastic data expanded to 120 pixels by linear interpolation between every two points.	99
5.1	Optical microscope image of the Rust-Oleum Metallic Paint at a magnification of 40x.	103
5.2	Optical microscope image of the Measurements Group reflective backing at a magnification of 20x.	105
5.3	Vector diagram for an element dS at an arbitrary orientation in space [124].	107
5.4	The local angle of incidence, δ , and its relation to the angle of incidence, θ . The angle of incidence is defined with respect to z_0 and constant for the whole surface whereas the local angle of incidence is defined from the normal at that location.	109
5.5	Cross-polarization ratio versus incidence angle, θ . As the rms slope increases, so does the depolarization. In this simulation, the relative permittivity was four and $\beta = 45^\circ$	112
5.6	There is a change in path length due to off normal incidence. The new path length is $-d(\sec\psi)$	114

5.7	Degradation of the fringes from the Kirsch problem for (a) zero depolarization and normal incidence, (b) zero depolarization and 5° from normal incidence, (c) 25% depolarization and normal incidence, (d) 25% depolarization and 5°, (e) 50% depolarization and normal incidence, and (f) 50% depolarization and 5°	117
5.8	Best fit isoclinic lines for various depolarizations and angles off normal incidence for the Kirsch problem.. . . .	118
5.9	Degradation of the FEA model for the notched hole at (a) zero depolarization and normal incidence and (b) 25% depolarization and normal incidence.	120
5.10	Best fit lines for various depolarizations and off normal incidence for the notch hole.. . . .	121
5.11	Best fit isoclinic lines for various depolarizations and angles off normal incidence for the two holes in a plate with different diameters.. . . .	121
5.12	Degradation of the isochromatic fringes with (a) zero, (b) 25% depolarization, and (c) 50% depolarization.. . . .	126
B.1	Schematic representation of a rough surface [129].	138

Abstract

Photoelasticity is an optical technique that measures the difference of the principal stresses plus the principal stress direction. A complementary technique is thermoelasticity which measures the sum of the principal stresses. Combining these two full-field, non-contact nondestructive evaluation techniques allows the individual stress components to be measured. One of the main difficulties in merging these two measurement systems is in identifying an appropriate surface coating. Thermoelasticity demands a highly emissive surface, while photoelasticity requires a thick, stress-birefringent, transparent coating with a retro-reflective backing. Two coatings have been identified that can be used for combined thermoelastic and photoelastic stress measurements: PMMA and polycarbonate.

An anisotropic electromagnetic boundary value model was developed to understand more fully the mechanisms through which photoelastic stress patterns are produced. This model produced intensity contour maps which matched the fringe patterns observed in the laboratory, and allowed the effect of measurement errors on the calculated stress tensor to be quantified. One significant source of error was the retro-reflective backing, which depolarized the light and degraded the resulting photoelastic fringes. A quantitative analysis of the degraded fringes, to be used as a rating scheme for reflective backing materials, showed that the isoclinic lines shift position as a result of the backing roughness and oblique incidence. This is a concern when calculating the stress components through the combination of photoelasticity and thermoelasticity because the data maps are integrated at the pixel level. Small shifts in the photoelastic fringes result in incorrect information being assigned to some pixels and hence lead to uncertainties in the stress tensor components. Progress in the understanding of the depolarization at the reflective backing allows the specification of new materials that will minimize this effect, as well as the development of robust computer algorithms to correct for any remaining depolarization.

**THERMOELASTIC AND PHOTOELASTIC FULL-FIELD
STRESS MEASUREMENT**

Chapter 1

Introduction

A structure is defined as any assemblage of material which is intended to sustain loads, and the study of structures is one of the traditional branches of physical science [1]. Nondestructive evaluation is a field devoted to the detection, repair, and prevention of flaws in objects. Its interests are with the detection of cracks, voids, disbonds, corrosion, and stress concentrations within an object and their effect on the overall structural integrity. Two techniques used for the characterization of stress distributions in a structure are thermoelasticity and photoelasticity. Photoelastic stress analysis is a well-established engineering tool, while thermoelastic stress analysis has been developed more recently. A combination of the two opens new possibilities for a better understanding the behavior of structures, as well as the development of practical flaw detection schemes for ensuring the safety of civil and aerospace structures and the quality of manufactured components.

1.1 History of Photoelasticity

In 1809 Étienne Malus, a military engineer and captain in the army of Napoleon, discovered the polarization of light by reflection. He found that light reflected at a particular angle from the surface of transparent bodies acquired the same property as light formed by double refraction. He measured the polarizing angles for water and

glass and concluded that the polarizing angle followed neither the order of refractive powers nor of the dispersive force. In 1811 David Brewster repeated the experiments of Malus and found the index of refraction to be the tangent of the polarization angle. He also discovered that complementary colors are produced by the action of crystalline bodies upon polarized light [2].

Brewster continued his optical experiments with annealed and unannealed glass drops. He observed dark lines in the unannealed bulbs that were not present in the annealed and then went on to discover that the burst bulbs cleaved in the direction of these lines. He also found that glass, when suddenly cooled, possessed all the optical properties of crystallized bodies, whereas slowly cooled glass did not have this special property. Brewster's investigation of the depolarization of light was not limited to glass. He found that calves' feet jelly, which had no particular action upon incident light, acquired, from simple pressure, a structure which enabled it to become double refracting [3]. He noticed the same result with a long plate of glass where he observed a deep black line when the glass was bent by the force of his hand. As this force increased, three or four orders of colors were present on each side of the black line. Brewster pointed out that these colors ascended according to Newton's scale of colors with the color at any particular point proportional to the compression or dilation to which that part is exposed. He noticed that some materials exhibited a greater number of colors than others when subjected to the same pressure.

Brewster took his observations and proposed the first (theoretical) application of photoelasticity. He surmised that if arch stones were made of glass or any other simply refracting substance, the intensity and direction of all the forces which are excited by a

superincumbent load in different parts of the arch will be rendered visible by exposing the model to polarized light [4].

In 1830 Brewster revisited birefringence in materials due to pressure and concluded that the force of double refraction is not resident in the molecules themselves but is the result of mechanical forces by which these molecules constitute solid bodies [5]. In 1853 he investigated the reaction of potash pressed between hard glass under heavy pressure. He observed that the resulting transparent film exhibited the phenomena of double reflection and polarization from its surface as if it was a large crystal [6].

At about the same time that Brewster was investigating potash, James Clerk Maxwell was conducting a mathematical study of the equilibrium of elastic solids. Maxwell began with the laws of elasticity expressing the relation between the changes in dimensions of a body and the forces which produce them. Using a triangle of unannealed plate-glass, Maxwell observed lines of equal intensity using circularly polarized light. He described these lines mathematically as

$$\phi_1(x, y) = \frac{I}{z} = \omega(p - q)\frac{1}{z}. \quad (1.1)$$

where I is the difference of retardation between the oppositely polarized rays, q and p are the pressures in the principal axes at any point, z is the thickness of the plate, and ω is the stress-optic coefficient. With plane polarized light he observed the direction of the principal axes as dark bands which shifted position as the triangle was turned in its own plane. These dark band were describe mathematically as

$$\phi_2(x, y) = \tan \theta \quad (1.2)$$

where θ is the angle of inclination of the principal axes. At the time, the best method of determining p and q was by graphical construction, although it was much better when ϕ_1 and ϕ_2 were known so as to resolve the pressures and directions of the axes. From Maxwell's mathematical study it was now possible to find the pressures from the curves of equal tint and equal inclination in any case where it may be required [7].

By this time it was well known that glass and other transparent, isotropic substances, when compressed unequally in different directions, behaved like doubly-refracting substances and exhibited colors, but few had considered how the effect varies with the nature of the light employed. It was assumed that the relative retardation in air was constant for all colors making the stress optic coefficient independent of the wavelength. The difference of the refractive indices was also considered independent of the wavelength whereby it exhibited no dispersion. Pockel showed that in certain glasses, the stress-optical coefficient does vary with the wavelength, being numerically greater in the green than in the red; in very heavy lead glasses, this variation was more rapid as the blue end of the spectrum was approached [8].

1.1.1 Design of the Polariscope

As the study of photoelasticity grew, various methods of fringe detection were created. When David Brewster studied strained glass he observed the colors with a pair of crossed Nicol prisms. In 1888 John Kerr used a Jamin's Interference-Refractor in his experiments on the birefringent action of strained glass. The apparatus was made from a Foucault prism, Iceland spar, a half wave plate, and a Nicol prism placed crossed to

that of the Foucault prism. It was reported that this system was capable of measuring a difference of retardation to the hundredth of an average wavelength [9].

The best means by the early 1900's for obtaining polarized light was through the use of prisms made from Iceland spar, first invented by Nicol and known by his name. Such prisms are unsurpassed for the purity and intensity of light transmitted through them. For scientific purposes, Nicol's prisms were more than ample, but the number of large prisms in existence was very limited. E. G. Coker and S. P. Thompson investigated other means of producing polarized light. They found the polarizing properties of glass plates were extremely useful in cases requiring a large doubly-refracting object. Because glass can be obtained at any convenient size and at a lower cost, it would make an easy, inexpensive means of obtaining polarized light. In practice, however, it was found that light which was incident upon a sheet of black glass at the polarizing angle transmitted polarized light with the intensity of one-seventh of the incident ray. This arrangement required a bank of lights to illuminate the plate to produce a sufficient intensity of polarized light for experimental use [10].

During this period, the usual optical equipment for photoelastic measurements had the following arrangement: a white or monochromatic light which passed through a condenser, a polarizing Nicol prism, a convex lens, the specimen and another lens, through another Nicol polarizer, and finally through an object which projected the image of the specimen on a screen or photographic plate. These lenses were large and isotropic with a large focal length to render small aberration. Of these elements and the required size of the Nicol prism made the photoelastic equipment very expensive. Alexander Goetz recommended the use of concave spherical mirrors in place of the

lenses, which reduced most of the experimental difficulties. This arrangement provided better accessibility and much more space for the test apparatus [11].

In the early 1900's, Coker set out to produce a "standard" photoelastic apparatus, later referred to as a polariscope, which could be used by engineers who had no great knowledge of physics. He designed an optical bench with a lens system which projected an enlarged image of a model upon a screen where Nicol prisms and mica quarter-wave plates were properly aligned and graduated. He developed a "tension-bar compensator" with which the stress-difference at any point in the model could be read directly in pounds per square inch on a spring balance. For the determination of the separate stresses, he used the method of deducing the sum of the stresses from measurements of the change in thickness of the model [12].

Efforts to reduce the amount of equipment and its cost were pursued by Raymond Mindlin and H. E. Wessman in the 1930's. Mindlin proposed a polariscope design where the light, after passing through the usual arrangement of optical devices, was reflected back through the same system [13]. Wessman's contribution was a simple, low-cost straining frame that could be designed and built in universities which established a photoelastic and model-analysis laboratory [14].

The Coker polariscope, seen in Figure 1.1, was the standard apparatus used in photoelastic stress analysis until 1974 when S. Redner developed a method of measuring photoelastic birefringence based on the phase-angle difference at two different wavelengths which allowed for automation of photoelastic data. He incorporated spinning crossed polarizers which rotated at a constant speed in the polariscope, modulating the light intensity emerging from the polariscope into



Figure 1.1 Present day version of the Coker polariscope. Pictured above is the Measurements Group, Inc. Model 030 Polariscope in front of a hydraulic load frame.

a sinusoidal wave. A photoelectric sensor which generated an electric current proportional to the light intensity was used as a detector. The direction of the principal stress was measured and compared to the measured voltage of a reference signal using a phase detector. This new automatic polariscope measured the direction and difference of principal stresses and strains simultaneously with the results appearing on a digital panel meter [15].

With image processing becoming more prevalent in the early 1980's, photoelasticians started incorporating it into their stress measurement systems. C. P. Burger and A. S. Voloshin developed the "half-fringe-photoelasticity" system which could resolve small differences in birefringence resulting either from low loads or low stress birefringence [16]. Early developments in photoelasticity concentrated on single point analysis, but advances in electronic equipment permitted full-field analysis. The major inadequacy in most of the automated systems was their inability to identify the isochromatic fringe orders without intervention with the operator [17].

Other polariscope designs were more focused on a particular application. Masayoshi Yamada developed a computer-controlled infrared polariscope to observe stresses in commercial silicon wafers [18-19]. H. Lee and S. Krishnaswamy combined a polariscope with a shearing interferometer to map stress fields in bimaterial systems. The main advantage of this set-up was that stress information could be obtained from optically isotropic as well as optically birefringent materials [20]. Yasushi Niitsu *et al.* used a He-Ne laser as the light source for a polariscope to measure small stresses in transparent materials [21]. E. Liasi *et al.* developed a retroreflection polariscope which differed from an ordinary polariscope in that the expensive field lenses were

eliminated by the addition of a retroreflector. The retroreflector was a single layer of high-index glass beads which enabled them to obtain images with double the fringe order [22]. D. E. P. Hoy used a color scanner as a digital recording polariscope. Scanners typically had, in the mid 1990's, a much higher resolution than a digital image camera and were widely available at a reasonable cost. With the addition of a polarizing element, the scanner could digitize fringes using white or monochromatic light with a fringe resolution of 0.2 fringes for white light or 0.5 for monochromatic [23].

In 1998 Jon Lesniak developed the Gray Field Polariscope (GFP1000). This polariscope was similar to S. Redner's 1974 system in that the polarizers rotate, but the GFP1000 system measured intensity and not voltage. Lesniak's system was digital and required no fringe analysis. The system had a resolution of 1/100 fringe and a spacial resolution of 80 x 60 or 480 x 360 pixels. The added feature of this system was its ability to determine the thickness of the photoelastic coating with an accuracy of $\pm 5\%$. This was significant because historically the photoelastic film was of known thickness before application because it is proportional to the difference in principal stresses. Uncertainties in thickness render unreliable photoelastic data. The GFP1000 could test components that have been painted with a photoelastic material and adjust for the coating thickness over the surface [24].

1.1.2 Advances in Photoelastic Analysis

The beginning of photoelasticity as it exists today started with the exploration of stress-distributions in engineering components of Xylonite by S. P. Thompson and E. G. Coker in 1909. This work attracted the attention of L. N. G. Filon whose chief interest

at the time was the mathematical theory of elasticity. It was his work which established the mathematical procedures to be followed in the determination of the stresses from the observations made on a stressed model. The work of Coker and Filon was responsible for the introduction of photoelastic measurements to many countries and provided the stimulus for work done by other investigators during this period [12].

With the Coker apparatus it was much easier to obtain the difference of the principal stresses from the isochromatic fringes and the angle of the principal stress axes from the isoclinics fringes, but deducing the stresses from these images was difficult. In 1921 A. Kimball and in 1923 L. N. G. Filon correlated the color of the observed fringes to stress values making it possible to obtain the stresses completely from observations of the photoelastic fringes [25]. Ikuzoo Arkawa continued this work with experimental observations of Bakelite to illustrate the extremely delicate behavior of photoelastic fringes. He found that the isoclinic lines of a circular disk with a center hole could not be satisfactorily traced in some parts of the plate, especially in the neighborhood of the internal boundary. He also found the isochromatics around the boundary were very delicately arranged in accordance with the mathematical theory of a multiply-connected plate [27].

With the growth of high-speed and large-size machinery, mechanics became an essential engineering tool. Because only the simplest problems in stress analysis can be solved theoretically, photoelasticity had become much more recognized [28-29], but its development was retarded due to the absence of a suitable material. Rather than color matching the fringes to correlate with stress level, Max Frocht used fringe orders to determine the difference of the principal stresses. With a monochromatic light

source, the fringes are much clearer than colored isochromatics and can be traced with accuracy and even photographed, securing permanent and convincing evidence of the stress distribution [30].

Photoelastic research was not limited to surface measurements. Three-dimensional photoelasticity was first observed by Maxwell in 1850 when he found that a hot jelly substance poured between two concentric cylinders under a torsional force maintained its effects on polarized light once the jelly cooled and the force was removed. In 1935 Solakian took a hot, circular rod of Marblette and held it in a twisted position as it cooled. Upon slicing the rod, the interior areas revealed concentric circles under polarized light. In 1936 Oppel theoretically discovered that cutting an annealed sample does not disturb its fringe pattern. M. Hetenyi continued the effort by conducting a large number of experiments for proof [31]. In applying the photoelastic method to states of stress which vary in three dimensions, the experimenter is confronted with the problem of interpreting the effects observed when light is passed through a medium whose properties vary from point to point in a general manner. Theoretical work on this topic was done in 1938 by Mindlin describing the optical aspects of three-dimensional photoelasticity [32] with an extension in 1940 by Drucker and Mindlin [33].

Many researcher in the 1920's were interested in determining the individual stresses over the surface of an object, and photoelastic analysis was a natural measurement tool to provide this information. The difficulty was that photoelasticity yielded the difference of the principal stresses, not the individual components. At the edge of an object, this was not an issue because only one of the two principal stresses were nonzero due to the edge creating a free surface. However, interior locations

were much more challenging to obtain individual stress components. Various methods had been employed to overcome this problem, such as graphical integration, but each had its own limitations and sources of error. In 1929 Henri Favre brought to the attention of the scientific community a method by which the individual stresses could be measured optically using a beam of light. He measured the absolute retardation of a beam passing through a transparent model when subjected to a change in stress. His measuring instrument was a precise interferometer which did not require the counting of fringes. This operation became much more rapid and accurate if the outside path was changed in length by an amount equal to the refractive change of the inside path. Although a precise measurement system, the photoelastic interferometer was not a full field measurement but rather a point detector on the order of $< 1mm$, the width of the beam [34].

As the physics of photoelasticity progressed, the discussion of measurement errors began. Stresses had been obtained previously by either color matching or compensation. In color matching known loads were applied to a tensile specimen of a similar material to that of the model creating a stress-color scale for comparison. Large errors were inevitable for a small change in stress, although fairly exact values were obtainable when the color changed from red to the blue. The stress compensation method used a polarized beam of light which passed through the model and focused on a specimen of the same material under tension. The line of pull of the tension specimen was adjusted to coincide with the direction of the minimum principal stress before altering the load until a dark spot appeared, corresponding to the part of the model under examination. As one can imagine, this method was very tedious in its

application [35]. In addition to errors associated with the identification of colors, Mindlin showed that if the retardation plates were not accurate quarter-wave plates, not only were the isoclinics not completely removed from the isoclinic fringe image but also the retardation of the fringes may be altered [36].

In attempts to reduce the number of errors, several new methods of photoelastic analysis were developed. D. C. Drucker proposed a method for obtaining σ_x and σ_y separately by the rotation of a two-dimensional model about an axis in its plane. He used the method of oblique incidence where the stresses are of significant magnitude [37]. Robert Gray developed the equations for the correction of the final fringe pattern from any initial stresses present in the coating or model [38]. Max Frocht and Roscoe Guernsey, Jr. combined the photoelastic data from frozen stress patterns with a numerical integration of the differential equations of equilibrium in Cartesian coordinates. This provided the actual principal stresses at each point of a homogeneous and isotropic body of arbitrary shape subjected to a general system of loads [39]. The development of plastics in 1953 provided the standard photoelastic material. They not only adhered to all kinds of structural materials, but their optical-strain constants were stable with time and large enough to permit commercial application in both elastic and plastic ranges of deformation [40]. J. W. Dally and F. J. Ahimaz produced a print with twice the number of sharper fringes by the superposition of light and dark isochromatic images [41]. Combining normal and oblique incident light, S. S. Redner showed high accuracy in the calculation of principal strains both at the boundary and in the interior regions of an object [42].

Douglas Bynum addressed other sources of error in a 1966 technical note discussing an experiment to determine the order of extremum error using the method of fringe multiplication. He found integrating effects due to strain averaging through the thick coating can be minimized by using an oblique angle of light incidence which corresponds to the minimum strain gradient. In addition, the light scatter due to the diffuse, mirrored birefringent coatings could be minimized if the structure surface is electroplated to obtain a specular finish for use of an unmirrored birefringent coating [43]. In 1962 J. W. Dally and F. J. Ahimaz investigated a photographic method for fringe multiplication in which a mixed-field pattern was obtained by superposition of ordinary light and dark field isochromatic fringe patterns. N. K. Das Talukder and P. Ghosh went on to show that although this technique gave the desired results, the equations derived for the fringe multiplication technique contained inaccuracies [44].

In 1979 R. K. Müller and L. R. Saackel combined photoelasticity with image processing methods. They took a photoelastic picture with a TV camera and stored it digitally. Using their own specially developed software, Müller and Saackel were able to do some basic manipulations on the digital photoelastic image [45]. Toyahiko Yatagai, *et al.* continued this work extracting fringes from the digital photoelastic images. Their method was based on the two-dimensional gray-level fringe peak detection technique [46]. A. S. Voloshin used the sensitivity of the image processing system to evaluate photoelastic materials showing a half-fringe order in the area of interest [47]. A. C. Gillies then developed a system which compared the digital results to mathematical models [48]. Techniques for finding fringe spacing and orientation in patterns laden with noise was developed by T. Y. Chen and C. E. Taylor. Their goal was

to automate the data-reduction processing so that a useful computerized, general fringe analysis algorithm could be used to analyze any fringe from any experimental method [49].

In addition to the image processing methods, Voloshin and Redner used spectral-contents-analysis to investigate the spectral content of a light beam passing through a stressed specimen. This beam contained all of the information necessary to automatically extract the value of the retardation [50]. A. J. Durelli and B. Ranganayakamma implemented numeric methods of Laplace's equation and finite element so as to verify experimental results [51]. P. Boulanger and M. Hayes studied the propagation of electromagnetic time-harmonic plane waves in deformed, non-absorbing, non-optically active materials and interpreted the results geometrically using an ellipsoid whose axes are proportional to the index of refraction in the principal coordinate system. The foundations of their method were based on Maxwell's equations and the electromagnetic constitutive equations [52].

Eliminating human interpretation of photoelastic fringes became popular in the early 1990's. E. A. Patterson and Z. F. Wang designed and built an automated full-field photoelastic analysis system with the objective of having minimum interaction with the operator [53]. One such procedure was the drawing of isoclinic lines from the photoelastic fringe resulting from linear polarized light. Often these fringes appeared as broad bands causing the researcher to approximate the isoclinic line through the center of the large band. K. Ramesh *et al.* developed a computerized method for the identification of the actual fringes from the bands. They developed an algorithm which utilized the minimum intensity criterion to thin the fringes to a width of one pixel [54].

With several stress separation techniques available, S. J. Haake and E. A. Patterson surveyed the methods to incorporate the most suitable technique into an automated full-field polariscope. They concluded that the shear difference method was susceptible to errors and that oblique incidence had the advantage of not using the inaccurate isoclinic parameters and having the neighboring points independent of each other [55]. In 1993, A. Asundi applied an interferometric technique, called phase shifting, to photoelasticity. This method had been used with other interferometric techniques, such as holography, Moiré, and even speckle interferometry, to determine fractional fringe order. This was accomplished by recording a few images corresponding to different optical arrangements in a given experimental situation. The optical elements invoked a specific phase shift between the recorded images, hence its experimental name of the phase-shifting technique [56]. S. J. Haake, Z. F. Wang, and E. A. Patterson used this new application to determine both the fractional isochromatic fringes and isoclinic parameters at all points in the field of view independent of their neighboring points showing the accuracy and reliability of this method [57]. J. Carazo-Alvarez, Haake, and Patterson then integrated phase stepping with spectral content analysis which identified the absolute value of the isochromatic parameter at a particular point and was used to calibrate maps of relative retardation produced by the phase stepping method [58]. Phase stepping and image processing of photoelastic data was restricted by the periodic nature of the data and the interaction between the principal angle and relative retardation. Z. F. Wang and E. A. Patterson used signal analysis and fuzzy set theory to overcome these difficulties [59].

By the mid 1990's, numerous researchers were working to obtain more exact fringe values using numerical methods. Y. Morimoto *et al.* separated the isochromatics and the isoclinics by calculating the Fourier transform of sequential images captured by rotating the polarizers and found this method insensitive to high frequency noise due to the Fourier filter [60]. Since isochromatic fringes are broad, uncertainties in the locations of the fringe centerlines limit the accuracy of the experimental data. B. Han and L. Wang subtracted the light field images from the dark field images to sharpen subfringes [61]. Jaime F. Cardenas-Garcia *et al.* rewrote the expressions for the principal stresses as a function of normalized variable distances from the center of the hole which enabled them to determine the stress tensor for any general loading situation [62]. C. Quan *et al.* evaluated the fractional fringe order by operating in the frequency domain and acquiring only one image. The fractional fringe order is obtained from the ratio of the real and imaginary parts of the Fourier transform which is then transformed to a total fringe order by phase unwrapping [63]. N. Plouzenec *et al.*, developed a new method to obtain isoclinic and isochromatic parameters by photoelasticity and numerical analysis. Four images are acquired from a plane polariscope which are numerically treated to separately calculate the isoclinic and isochromatic parameters. The parameters are functions of arctangents and arccosines which need to be unwrapped to restore continuity to the entire field. The results for a disk under diametrical compression produced a maximum difference of 1° for the isoclinic angle and 0.05 fringes for the isochromatic parameter [64].

In addition to numerical methods, the mid 1990's also provided photoelasticity with new methods of obtaining fringes. A. Ajovalasit *et al.* developed a new method

for automatic analysis of isochromatic fringes in white light, called red, green, and blue (RGB) photoelasticity. This process acquired the isochromatics with a color video camera and decomposed them into red, green, and blue before being compared to a calibration array [65]. K. Ramesh and S. Deshmukh used a similar method to determine fringes up to three orders. Their study found that using the difference in the RGB values between bright and dark field images reduced the noise in the data points [66]. S. J. Haake, E. A. Patterson, and Z. F. Wang used phase stepping to determine both the fractional isochromatic fringes and isoclinic parameters at all points in the field of view [67]. B. Han and A. L. Wang determined fractional fringe orders through the use of the Tardy Compensator with data from a robust algorithm producing highly sharpened isochromatic fringe contours in the immediate vicinity of an isoclinic line [68]. Sherri A. Sparling and Carolyn F. Small used hue, saturation, and light intensity values to identify photoelastic fringe values in the field of view of the camera. The digital images were obtained through a reflective white-light polariscope [69].

By 1997 numerous methods for the automation of photoelasticity had been developed. E. A. Patterson reviewed these methods and concluded that they all were derived from a common theoretical basis. He emphasized that all of the methods suffer from the same fundamental disadvantage, namely the periodic nature of the relative retardation and undefined regions in the isoclinic angles [70]. Most of the attempts to extract the difference of the principal stresses and the isoclinic angle have used phase-stepping which enabled the photoelastic parameters to be calculated through an arctangent function. A drawback to this approach is the need to unwrap the isoclinic angle and isochromatic parameter. Although several unwrapping procedures

are available, the isochromatic parameter and the isoclinic angle interact causing a high signal-to-noise ratio in some regions. Andrew Nurse developed a new approach to phase-stepping in which many of the problems involved with the extraction of data are either solved or circumnavigated. Using three narrow-band filters – red, green, and blue– in combination with a white light source and a plane polariscope, six images were collected and a least-squares algorithm used to obtain the fringe patterns. The least-square routine reduced the effects of the noise incurred in the data collection process; the three colors allowed the photoelastic parameters to be determined without the isoclinic-isochromatic interaction problem, and the isoclinic angle phase map could be unwrapped and assigned to one principal angle [71]. At the same time T. W. Ng used step-loading to overcome discontinuities in the phase measurement requiring unwrapping. This method required recording of successive images with phase increments or decrements of π radians or less and the loading restricted to either increase or decrease. Their technique required twice the number of intensities sampled compared to digital speckle-shearing interferometry [72]. M. J. Ekman and A. D. Nurse later extended load-stepping to determine the isochromatic parameter using three incremental loads instead of three wavelengths. This method was able to yield the absolute value of the isochromatic parameter without the need of auxiliary techniques for a base fringe value [73].

Other automation methods were done by Ramesh and Deshmukh who investigated phase shifting using color image processing – a superposition of image planes of red, green, and blue. They investigated whether one or all of the image planes can be thought of as behaving like an optical filter so that they can extend phase shifting to the

color domain [74]. T. Y. Chen demonstrated a new approach for digitally determining photoelastic birefringence using the relationship between the intensity values and fringe orders of two wavelengths. The methods allowed for the automatic determination of fringe orders without using the zero-order fringes with a 0.05 fringe accuracy [75]. G. Petrucci developed a technique based on phase-stepping with the use of true image color technology for evaluations. This system used four images from a dark field polariscope taken by rotating the optical elements in steps of 22.5° . Although this technique required more expensive hardware, its advantages were good resolution and high execution speed [76].

The theory behind phase-stepping is based on monochromatic light. W. Ji and E. A. Patterson investigated the effects of white light on phase-stepping through a mathematical model to analyze the errors generated by the use of various bandwidth spectra in the polariscope light sources. Errors due to the mismatch of quarter-wave plates and dispersion are thought to cause significant contributions to errors in the isoclinic angles and isochromatic fringe order. The form of the spectrum of white light directly influences the errors in the isoclinic angle and isochromatic fringe order. This error is larger for high isochromatic fringe order compared with low fringe order – typically 5 percent error for one fringe order. Using medium-band filters with a central wavelength matched to the quarter-wave plate greatly decreased the error generated by white light, allowing fringe orders up to 6 and 10 to be measured with an accuracy of ± 5 percent using 80 and 40 *nm* bandwidth filters, respectively [77].

The last two decades have seen significant advances in photoelasticity with the advent of PC-based digital image processing systems. The exploration of photoelastic

stress analysis does not stop here but will be continued into the next millennium with the development of new algorithms, analysis techniques, and hardware further advancing our understanding stress analysis through the use of birefringent materials.

1.2 History of Thermoelasticity

Whereas photoelasticity uses a birefringent coating to produce fringe patterns corresponding to the underlying stress field, thermoelasticity correlates temperature variations to stress. The phenomenon of a material changing temperature when stretched was first noted by John Gough in 1805. While stretching a piece of India Rubber, he felt a sensation of warmth when the rubber touched the edge of his lip. (It was known that the lips possess a high degree of sensitivity which enable them to detect small temperature changes with greater fidelity than other parts of the body.) He found that this temperature increase was destroyed by permitting the rubber to contract [78]. In 1830, Weber saw this effect in metals when he noted a sudden change in tension applied to a vibrating wire caused the fundamental frequency of the wire to change gradually rather than suddenly as he had expected. He reasoned that this transitory effect was due to the temporal change in temperature of the wire as higher stresses were applied [79].

Gough and Weber observed these temperature changes but offered no explanation into its cause. It was not until 1851 that William Thomson (Lord Kelvin) provided the theoretical basis for thermoelasticity: the coupling between mechanical deformation and generated heat. Thomson wrote that heat is not a substance, but a dynamical

form of mechanical effect. He concluded that there must be an equivalence between mechanical work and heat as between cause and effect. From this reasoning he derived

$$\theta = \frac{Ke}{\mu\kappa} \quad (1.3)$$

where θ is the change in temperature, e is the coefficient of expansion, K is the reciprocal of compressibility, μ is Carnot's Function, and κ is the specific heat under constant pressure. Equation (1.3) illustrates that the change in temperature of any solid is modified by an infinitely small alteration of its volume. For a rod or wire, the increase in temperature produced by stretching is written specifically as

$$\Delta\theta = \left(\frac{-a\theta}{\pi r^2 \rho s J} \right) \Delta F \quad (1.4)$$

where a is the thermal coefficient of expansion, r is the radius, ρ is the density, s is the specific heat, θ is the absolute temperature, ΔF is the increase in stretching force, and J is the mechanical equivalent of heat [80].

Joule was the first to attempt verification of equation (1.4) in 1859 using various liquids, metals, woods and rubber. He found general agreement between observations and theory but with an average 15% discrepancy. Edlund in 1865 used metal wires to show that the relative temperature change in different metals could be predicted by the Thomson formula but failed to show absolute accuracy – steel showed only 63% of the calculated temperature change. In 1882 Haga succeeded in verifying Thomson's formula to within 2.54% for steel wire and 0.25% for German silver. He used improved methods of measuring small changes in temperature and considered variations in the thermal coefficient of expansion at different temperatures. His method of temperature measurement utilized a thermocouple with one end soldered to the stretched part of the

wire and the other to an unstretched part. The difficulty in measuring small changes in temperature (<0.5 C) was where all the disagreement lay. The heat liberated or absorbed was very small and was rapidly lost by surface conduction and radiation from the wire making the galvanometer unable to register the total initial change in temperature. K. T. Compton and B. D. Webster discarded the thermocouple method and employed a resistance method requiring the use of a Wheatstone bridge. With the stretched wire forming one arm of the bridge, the resistance measurements were 35 times more sensitive than the galvanometer in Haga's experiment. To reduce the rate of heat loss, the steel piano wire was passed axially through a polished test-tube with ends plugged with cotton before being covered entirely with a thick layer of cotton. This reduced the rate of loss of heat to less than half of the rate when freely exposed producing measured values that were within 0.07% of the calculated values [81].

Tamman and Warrentuip continued this experiment in 1937 on copper, nickel and carbon steel. They showed the thermoelastic effect and the reversal of temperature change stopped at the yielding point of the material where they detected a sudden energy released by plastic strain. Their experimental goal was to determine the yield point in certain metals from this information [79]. In 1938 Clarence Zerner used thermoelasticity in his theory of internal friction of solids to show the importance of thermoelasticity in the damping of vibrations in polycrystalline materials [82]. Further advances in the understanding of thermodynamics and thermoelasticity resulted from M. A. Biot in 1956 who investigated the entropy changes in deformed materials. He derived thermoelasticity, not from thermodynamics, but by showing the inverse process of thermoelasticity leads to a variational formulation which coincides with a general

principle of irreversible thermodynamics using an entropy flow field. He found that an infrared signal yields the sum of the principal stresses and was insensitive to shear stresses [83].

With advances in infrared radiometric technology, Milo Belgen, at the NASA Langley Research Center in 1967, found it possible to measure dynamic structural stresses with infrared radiometers. With the applied strain within the elastic limit of the material and oscillations of strain rapid enough to be considered adiabatic, the average temperature of the object was found to increase slowly due to damping energy generation while the instantaneous temperature oscillated. Detection of this temperature oscillation correlated to areas of stress. With thermoelasticity yielding the sum of the principal stresses, strain gauges yielding the tension-compression strain in the direction of installation, photoelasticity yielding the difference of the principal strains, and brittle coatings yielding major principal tension strain, Belgen concluded that the use of infrared measurements in combination with existing methods would make biaxial stress data feasible.

Belgen's thermographic instrumentation consisted of a Cassegrainian type radiometer with a compensated thermistor bridge and a germanium lens detector. The optics yielded a field of view measuring 10.24 square millimeters for a target distance of 2.4 meters. During his analytical studies, Belgen discovered that a high-emittance surface on the object was quite desirable because he found painted beams yielded a higher radiometer signal than unpainted beams. To ensure this condition, he applied two coats of flat, black paint before data was acquired. Further analysis showed that the paint acted as a thermal insulator at high frequencies. To overcome this situation, the

high-emittance coating would be used at low frequencies to obtain improved signal-to-noise ratios [84-85].

The most common reason for measuring temperatures produced by deformation was to study the stored energy of cold work. Temperatures near running cracks had been measured as large as 1000 K - 2000 K. K. E. H. Jordan and B. I. Sandor wanted to establish a basis in 1978 for the quantitative stress of metal with stress analysis. Rather than using an infrared system, they chose thermocouples due to their cost compared to an infrared system [86].

It was not until 1974 that the first laboratory instrument was capable of measuring stress patterns down to a level of sensitivity to be of practical interest to a wide range of design engineers. The temperature changes of interest were in the range of 0.001 *K* to 0.3 *K*. This translated to 200 *Pa* in aluminium for a 1 *mK* temperature change. The first commercially available instrument to make practical use of the thermoelastic effect for experimental stress analysis was the SPATE 8000 (Stress Pattern Analysis by measurement of the Thermal Emission). This was a computer controlled, non-contact instrument which provided quantitative stress values at given points through a 16-color scale displayed on a monitor. A germanium lens in conjunction with motorized horizontal and vertical scanning mirrors focused the thermoelastic flux from a spot on the structure to a spot onto the detector [79].

Although the SPATE 8000 possessed the sensitivity necessary for thermoelastic stress analysis, it was only a point detector requiring approximately 45 minutes to scan a small area. D. Mountain and J. Webber built a thermoelastic system in 1978 that synchronously detected the infrared signal at the peak of oscillation. They produced an

image by building up many point measurements in a raster pattern [87]. D. Oliver *et al.*, increased the efficiency of this system in 1982 by using all of the signal, not just the peak, to produce a thermoelastic image. In 1982 L. R. Baker and J. M. B. Webber developed an infrared camera with a sensitivity of 0.001 K using a dichroic beam splitter focused by a germanium lens on an infrared detector. Rotation of the scanning mirror enabled an extended area on the object to be scanned, and hence the generation of a television-type raster on a colored cathode-ray tube. In this way, one of 16 possible colors can be related to the level of absolute or bipolar stress at a particular point on the object seen on a TV monitor for real-time stress display [88]. Two year later, J. Heyman reported producing a thermoelastic image by averaging multiple subtractions of image pairs taken before and after the application of stress to the sample using a commercial fast scan radiometer [89]. In response to the technical improvements, the SPATE 9000 was introduced in 1987 incorporating a more powerful computer with improved software developed by John Deere Incorporated and the University of Wisconsin. This system now provided full-field thermoelastic information and was capable of collecting both amplitude and phase whereas the SPATE 8000 was limited to amplitude measurements [79].

The SPATE 9000, as well as the Baker/Webber system, measured the surface temperature in response to applied stresses. Several mechanisms may affect the accurate measurement of the stress-induced temperature. Among them are internal conduction of heat between regions of different stress levels, heat lost from the surface to the environment, and the attenuating effects of surface coatings which may be otherwise beneficial to surface emissivity. The benefit of the use of cyclic loading as a

method of reducing the effects of internal and external heat transfer is balanced by the increased attenuation with frequency due to the coating. The coating is used to obtain a constant emissivity, to maximize the radiant energy, and to avoid reflected heat which attenuates the thermoelastic response from the object. A thermoelastic inert coating will attenuate the temperature change by simple resistance, capacitive thermal lag, and thermal “drag-down.” The attenuation increases with increasing frequency and coating thickness. McKelvie analyzed the amplitude of the surface temperature calculation induced by cyclic loading through solutions of the heat-conduction equation and found his analytical work in accord with experimental work of earlier investigators [90].

Although thermoelastic data is in the form of the sum of the principal stresses, the real interest is with the individual stress components. In 1988 T. G. Ryall and A. K. Wong presented a method for obtaining the stress components from thermoelastic data by taking into account the boundary conditions and the expected form of the stress distribution by means of a least-squares method. They found this technique to be relatively insensitive to random noise but due to ill-conditioning of the least squares matrix, the high frequency components of stresses were not able to be resolved. Also, the sample that they chose for this demonstration was rather simple, a known bulk stress applied at the boundary $x = 0$. For an arbitrary geometry, the problem becomes much more difficult [91].

In 1990, Huang *et al.*, also developed a method for determining the individual stresses from thermoelastic data using only a few locations of known stress or a traction-free segment of a boundary. Their method of separating stresses used an interferometrically recorded sum of the principal stresses in transparent models. For

problems where the signal is on a traction-free edge, the stress could be approximated by a polynomial of the third degree or by using finite difference approximations [92].

Thermoelastic stress analysis to this point had been purely qualitative because of noisy data and unreliable edge information. Y. M. Huang, R. E. Rowlands, and J. R. Lesniak developed a hybrid method of stress analysis to simultaneously smooth the thermoelastic data, enhance the boundary information, and separate the stresses at nonboundary locations using only the thermoelastic data. Their approach was to represent the loaded, isotropic, plane elastic object with stresses written in terms of complex stress potentials [93]. Huang and Rowlands continued this work by extending the model to areas adjacent to a curved boundary which only required limited information in the area of interest [94].

By 1990 the study of crack growth was of considerable interest to the NASA Langley Research Center. Although thermoelasticity was a natural method of observing crack propagation, the SPATE 9000 was too slow for analysis. K. Elliott Cramer and Christopher Welch at NASA combined a commercial infrared radiometer with real-time digital image processing to use for crack studies. The infrared camera was a video fast-scan system based on a single detector and fast-scanning mirror set which output information in video format at a rate of 30 images per second. At the same time J. R. Lesniak at StressPhotonics, Inc. was funded by NASA Langley to develop a new type of infrared camera that utilized a focal plane array in place of a vibrating mirror as in the Cramer/Welch system. This fast-scan detector-array camera was capable of obtaining 434 images per second using a 128 x 128 InSb array. Although this system was not as sensitive as the Cramer/Welch system, it overcame this difficulty by averaging more

data. Typical thermoelastic images with a temperature resolution of 1 mK would take 30 seconds [95].

In all of the thermoelastic systems, signal-to-noise ratios were a concern due to the very small temperatures being generated by the sample. The noise associated in thermoelastic data is related to the quantum statistics of photon emission and is dependent on the specimen's temperature. If a thermoelastic signal for a room temperature object was 1 mK , the same load but with the sample at an increased temperature would produce a signal exceeding 1 mK . Although ideal performance improves with elevated temperature, the practical performance is less because of electronic saturation problems. This problem occurs when the vastly increased flux due to the elevated temperature exceeds the design limitations of the electronics. J. Lesniak and B. Bartel designed a furnace to address this specific problem with elevated-temperature thermoelasticity. They were able to obtain a signal-to-noise ratio at elevated temperatures similar to ratios seen at room temperature [96].

Rather than using a cyclic load at a constant amplitude and frequency, S. T. Lin *et al.*, studied randomly loaded structures which are characteristic of field measurements on engineering structures. This method was useful for systems experiencing nonmodal behavior and was based on the ratio between total power of the thermoelastic signal and the total power of a reference signal with a specified time frame. An added benefit of this method was its ability to separate the measured thermoelastic data into individual stresses [97].

During the computational evaluations of measured thermoelastic data, inherent experimental noise can overwhelm the quality of information. B. J. Rauch and R. E.

Rowlands produced a numeric filter which incorporated the mechanics of the problem into a smoothing technique for noise removal. This filter was based on the isotropic compatibility equation and used a least squares fit to a general solution of Laplace's equation. It removed the noise without diminishing the information in the original measured data [98].

Under adiabatic conditions the heat transfer inside of the material under a cyclic load is neglected, whereas under nonadiabatic conditions, heat diffusion attenuates the spatial temperature gradients leading to an underestimation of stress concentrations. S. Offermann *et al.*, performed iterations of the direct heat diffusion model using the finite element method until the calculated temperature converged to the measured values. This method yielded a good restoration of the real stress map [99].

Since the mid 1980s researchers have been investigating the reproducibility of thermoelastic data between various SPATE systems. The first study found varied results, up to 20 percent difference, between five SPATE systems testing identical materials. These differences were attributed to inaccuracies in loading and variations in the test specimen material. The second study used eleven SPATE systems to calculate the ratio of temperature change to strain change. Comparison of the results showed a 16 percent variation which was blamed on the detector responsivity. J. M. Dulieu-Barton and P. Stanley conducted a third study which assessed the long-term reproducibility, reliability, and stability of various systems over a four year period. They found the detector responsiveness could change by 8 percent over a nine month period. To ensure high quality, reliable thermoelastic data, detector responsiveness should be redetermined periodically using a reliable standard test specimen (e.g., a Brazilian

disk), the test machine should be periodically recalibrated, and a controlled emissivity paint should be used [100].

With the price of a thermoelastic measurement system 30 times that of a photoelastic system, thermoelastic stress analysis has not become a standard measurement tool. Recent advances in detector arrays are promising to double the spacial resolution of the thermoelastic image at half the original cost. This step along with additional improvements in software is sure to make thermoelasticity a standard stress analysis system in every laboratory.

1.3 Motivation to Combine Thermo- and Photoelasticity

Accurate determination of stress distributions is essential in assessing the structural integrity of a component. Thermoelastic signals are proportional to the sum of the principal stresses

$$\Delta T = \left(\frac{-\alpha T}{\rho C_p} \right) (\sigma_x + \sigma_y) \quad (1.5)$$

where α is the thermal conductivity, ρ is the density, C_p is the specific heat capacity. Alternatively, photoelasticity measures the difference of the principal stresses plus the principal stress direction

$$(\sigma_x - \sigma_y) = \left(\frac{E}{1 + \nu} \right) \left(\frac{N_n \lambda}{2Kt} \right) \quad (1.6)$$

where E is the modulus of elasticity, ν is Poisson's Ratio, N_n is the normal incident fringe order, λ is the wavelength of light, t is the thickness of the photoelastic coating, and K is the strain-optic coefficient. With each system it is difficult, sometimes impossible, to determine the individual stress components without the

aid of a free surface. Several methods have been employed with photoelasticity to find a solution to this problem. One method involves the drilling of small circular holes over the surface of the test object, the diameter of which is on the order of the thickness of the photoelastic coating, creating numerous free boundaries [101]. Another method combines normal incidence photoelastic measurement with oblique incidence measurements. The problem with this procedure is that the oblique incident measurements are much more difficult and time consuming compared to normal incidence because not only must the oblique angle be accurately determined, geometric details in the testing object, such as small fillets, reentrant corners, physical obstructions, etc., will often prevent oblique incidence measurements. In addition, for certain strain states, significant errors can result from small inaccuracies in the measured fringe orders producing large errors in the calculated strains [102].

With the combination of the thermoelastic and photoelastic stress measurement systems, the full-field stress tensor can be determined with few geometric limitations. The key in linking the two systems is the identification of a coating that is both highly emissive (thermoelastic) and birefringent (photoelastic). A partial-integration of thermoelasticity with photoelasticity was done in 1996 by S. Barone and E. A. Patterson. The two stress measurements were applied to the *opposite faces* of a plate with a central circular hole. They claimed that the information could be obtained sequentially on the same face if the photoelastic coating could be bonded to the painted surface in the thermoelastic test or levered off with a scalpel before painting for thermoelastic analysis [103].

1.4 Dissertation Overview

The objective of this dissertation is to show that thermoelasticity and photoelasticity can be combined to produce the components of the stress tensor over the *entire* area of an object. Chapter 2 will address the coating issues between the thermoelastic and photoelastic stress measurement systems and provide a list of materials capable of being used for both experiments. Mathematically, the photoelastic effect is more difficult to describe than the thermoelastic effect. Chapter 3 will review the various theories of photoelasticity and Chapter 4 will describe the anisotropic electromagnetic boundary value problem. This is used to simulate the photoelastic fringes which will be used to explore conditions under which the fringes change shape and position. One such condition that has received very little attention in the literature is the depolarization of the light wave upon reflection. Changes to the incident light wave, in photoelasticity, are solely the result of the anisotropy induced by the applied tensile stress. Any changes added by the reflective backing are unwanted because it will alter the photoelastic data resulting in uncertainties in the calculated stress tensor components. It will be shown in Chapter 5 that a slight shift in the fringe pattern results in non-negligible errors in the calculation of the stress tensor components. Chapter 6 will conclude with a summary of the project and suggestions of future work for the determination of the stress tensor components through the combination of thermoelastic and photoelastic stress measurements.

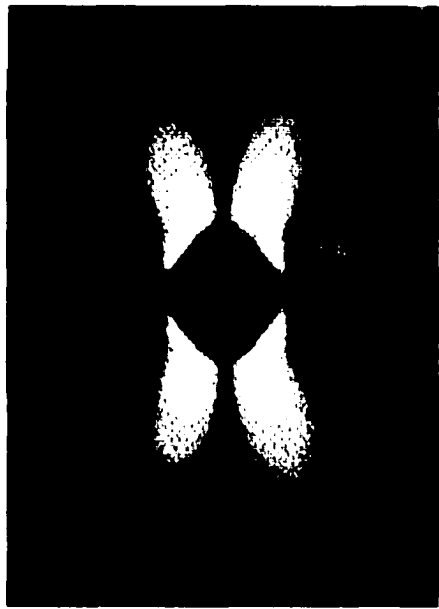
Chapter 2

Photo-Thermoelastic Coating

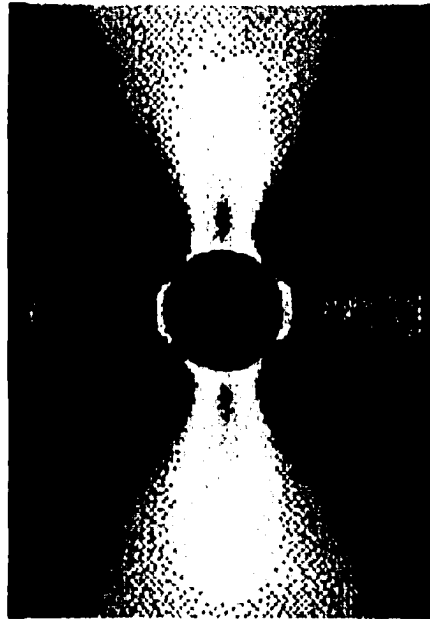
2.1 Measurement Systems Overview

Photoelasticity is a widely used, and well-established, full-field technique for the measurement of surface stresses in a part or structure during static or dynamic testing, as seen in Chapter 1. The stresses are seen as fringes in a clear, stress-sensitive coating, such as polycarbonate or epoxy, bonded to the test part. Upon application of an external load, the coating becomes optically anisotropic (birefringent). The induced anisotropy decomposes the incident light into two waves: an ordinary and an extraordinary wave which possess perpendicular polarizations relative to each other and different phase velocities. With the index of refraction related to the phase velocity by $n = c/v$, where c is the speed of light, the difference in n between the two waves multiplied by the thickness of the coating is defined as the relative retardation. As the coating becomes more optically anisotropic due to the applied stress, the relative retardation increases creating an interference which produces more fringes.

Photoelastic fringes are observed with polariscope composed of a polarizer, analyzer, two quarter-wave plates, and a light source. Two sets of fringe patterns, as seen in Figure 2.1, are produced in photoelastic stress analysis: isoclinics with linear polarized light and isochromatics with circular polarized light. Isoclinics appear as



(a)



(b)

Figure 2.1. Isoclinic (a) and isochromatic (b) photoelastic images for a hole in a PMMA plate under vertical tension taken with the Model 030 Polariscope.

dark lines which change position as the analyzer and polarizer are rotated. Along this line the angle of rotation of the analyzer/polarizer equals the angle by which the stress matrix is converted to a diagonal (principal) matrix. This angle is referred to as the “direction of the principal stresses.” Whereas linear polarized light reveals angle information, circular polarized light reveals isochromatic fringes which yield the difference in magnitude between the principal stresses. When using white polarized light, isochromatic fringes appear as varying bands of color corresponding to different levels of retardation between the two waves. With increasing relative retardation, each color in the spectrum is extinguished, starting with violet, leaving the complementary color for observation. Conversion of the color to the difference of the principal stresses is done with a color-to-stress chart which is unique for each photoelastic material. When polarized monochromatic light is used for illumination, the isochromatics appear as dark and bright fringes which are converted to the difference of the principal stresses through the identification of the fringe order.

A complementary stress measurement technique to photoelasticity is thermoelasticity. This is a relatively new method of stress detection which provides the sum of the principal stresses using thermographic techniques. As an object deforms under an applied stress, the surface exhibits small temperature fluctuations in areas of tensile and compressive stresses. These temperatures are very small and difficult to detect, requiring sensitive infrared detectors and cyclic loads ($1mK$ corresponds to stress measurements of $1.0 MPa$ in steel and $0.4 MPa$ in aluminum). Several factors affect the surface temperature – internal conduction of heat between regions of different stress levels and heat lost from the surface to the environment. A loading

frequency on the order of a few hertz is used to make the object repeat the temperature signals to ensure detection from the radiometer but to avoid the overall temperature of the sample to increase due to conduction. An added concern with the thermographic measurement is with the surface emissivity. A surface with a low emissivity, such as aluminum, reflects most incident infrared radiation (originating from the surrounding environment) concealing any temperature fluctuations which are a result of the induced mechanical deformation. Emissivity enhancing coatings, such as flat, black paint, are applied to such objects to obtain a thermoelastic stress map which is displayed as a two-dimensional color map. Each stress image is accompanied by a legend which is used to convert the colors to the sum of the principal stresses.

One of the main difficulties in merging thermoelasticity with photoelasticity is with the identification of an appropriate coating. The key to linking the two systems is the identification of a coating that is both highly emissive and birefringent.

2.2 Coating Characteristics

For a material to function effectively as a photoelastic coating, it must possess certain characteristics. Ideal photoelastic materials are transparent, have a low material fringe value (load required to produce one fringe-per-unit thickness) and possess linear strain-fringe and stress-strain relationship. Moreover, they must be isotropic, unaffected by small temperature variations as well as free from time-edge effects, residual stresses, and optical and mechanical creep. They must also be inexpensive and easily available. A large numbers of polymers exhibit birefringence and are

candidates for photoelastic coatings. Epoxy resins, introduced in the 1950s, are the most widely used and preferred materials suitable for not only birefringent coatings but also for three-dimensional photoelastic models. Some other commonly used photoelastic materials are polycarbonates, polymethylmethacrylate (PMMA), methanol of polycarbonate (PCBA), polyurethane, and elastomers [104-105].

If the clear, birefringent coating was opaque in the $3 - 5 \mu m$ band of the infrared, the coating could be used as a thermoelastic coating. Table 2-1 lists the transmission ranges for various birefringent polymers [106].

Table 2-1. Optical properties of some common polymers.

Polymer	Optical Transmission Range
PMMA	$< 330 \text{ nm}$, $340 \text{ nm} - 1660 \text{ nm}$
Low-Density poly(ethylene)	Visible - IR
High-Density poly(ethylene)	Visible - IR
Poly(vinyl Chloride)	UV - Visible - IR
Poly(styrene)	$< 250 \text{ nm}$, $300 - 3.2 \mu m$, $> 3.6 \mu m$
Nylon	Visible (if thickness $< 0.5 \text{ mm}$)
Celluloic compounds	Visible
Poly(carbonate)	UV - Visible - IR
Epoxide resins	Visible

Not only is material selection a concern but so is its thickness. Typically, thicker photoelastic coatings have better optical responses compared with thinner coatings of the same material because the response is proportional to coating thickness, as seen in equation (1.6). Thermoelastic coatings, on the other hand, need to be thin due to attenuation effects. Alexander MacKenzie investigated the effects of surface coatings on infrared measurements assessing coating responses to loading frequencies, angles of view, and elevated temperatures. He found the response greatest for objects with thin coatings experiencing low frequencies. As the frequency and coating thickness

increased, he observed diminishing thermoelastic signals due to the coating becoming more insulator-like, preventing the thermoelastic signal generated at the object/coating interface from propagating to the surface of the coating for detection. At high frequencies and coating thicknesses, he found the thermoelastic signal leveled out to about ten percent of the maximum. In addition, he concluded that the coating placed a thermal load on the surface of the substrate resulting in attenuation and phase lag in the substrate response at the substrate/coating interface. For a given substrate/coating material combination, this attenuation and a phase lag was a function of coating thickness and strain frequency. The thermoelastic coating could also contribute to the detected signal but this would be a small effect if the substrate had a high thermal diffusivity compared to the coating [107].

Typical photoelastic sheets range in thickness from 25 μm to 305 μm with an adhesive layer of approximately 40 μm whereas the thickness of the flat, black paint is about 10 μm . This makes the photoelastic layer six to thirty-five times that of the paint thickness. In photoelasticity a fraction of the applied load may be borne by the coating, which acts as a reinforcement on the test object. In this case stresses in the test object are smaller for a given load with the photoelastic coating than without it. Corrections are needed to calculate the actual stress on the test object without the added strength of the photoelastic coating [108].

If thermoelastic information is to be obtained from the photoelastic coatings six to thirty-five times the thickness of black paint, the response time of the coating will substantially lag that of the substrate being measured. This is due to the layers having a

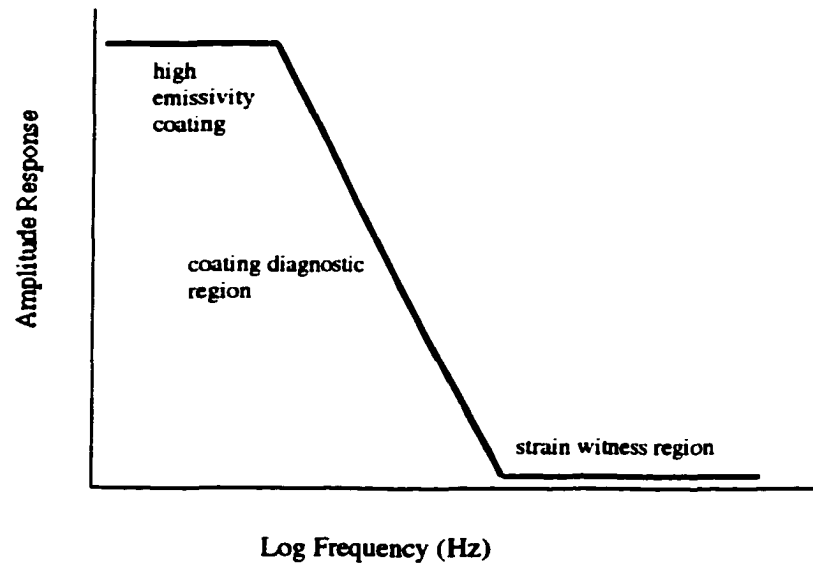


Figure 2.2. Theoretical plot of the amplitude response of a sample coated with black paint as a function of frequency. Notice the fall-off region as the frequency increases. At high frequencies the amplitude from the sample is completely damped-out in the coating. The remaining signal is the response generated by the coating reacting to the applied strain.

finite heat capacity and often being an thermal insulator. Reducing the thickness of the coating is the most direct way of reducing the thermal response time.

MacKenzie formulated the coating response as a thermal wave problem which depended on various parameters of the coating such as thickness and the frequency of oscillation. Analysis of this equation by Welch and Zickel showed that as the frequency and thickness increase, the thermal response drastically decreases in amplitude and develops a substantial phase shift. This reduction in amplitude does not continue indefinitely but is terminated in a region with zero phase and a single value, as seen in Figure 2.2. This high frequency-large thickness regime is the thermoelastic response to strain in the coating itself with the thermal waves from the substrate being completely absorbed by the coating. This was designated as the strain witness region [109].

The work of Welch and Zickel focused on black paint and not polymer coatings which are of interest to this project. S. Barone and E. A. Patterson investigated polycarbonate films, typically used in reflection photoelasticity, as a strain witness in thermoelasticity. These films were bonded to the test object for analysis. If the thickness of the coating was small in comparison with that of the substrate, the strains at the surface of the object were transmitted without significant variation. The thermoelastic temperature change of the coating was always in phase with the loading, whereas the phase from the substrate varied with thickness and frequency. When the signal was generated by the coating rather than the substrate, very thick coatings and high frequencies were preferred so that the interference of the thermoelastic effect of the coating with the thermoelastic effect coming from the substrate would be negligible. In addition, the coating must have an adequate infrared opacity to have a good emissivity and reduce errors due to reflection of radiation from the environment. Most materials commonly used in photoelasticity are opaque to wavelengths above $2.3 \mu m$. Barone and Patterson found the photoelastic material PS-1 worked well as a thermoelastic coating. The actual signal from the PS-1 coatings turned out to be much smaller than the signal obtainable with black paint. Increasing the sensitivity of the detector compensated for this lower signal but added noise to the data, thus making the measurement less accurate.

Barone and Patterson made several conclusions from thermoelastic data taken with a photoelastic coating. The 1 mm thick photoelastic coating on an aluminum plate showed a slight enhanced thermoelastic response compared to the response for the 2 mm and 3 mm coating for all frequencies. This was due to the reinforcing effect of

the coating on the substrate, a result typically found in reflection photoelasticity and was expected here as well. Moreover, to avoid out-of-plane bending moments, two coatings were applied to opposite sides of the specimens for the 1, 2, and 3 mm thick coatings to double the reinforcing effects. Observations of the phase difference between the loading and temperature response did not show significant variation over the region observed. This indicated that the effects from thermal diffusion were small and constant with thickness of the coating and loading frequency [110].

2.3 Dual-Use Coating

Candidates for the thermoelastic and photoelastic coating must be opaque in the $3 - 5 \mu m$ band of the infrared and be birefringent in the visible. Two materials fitting these requirements are polymethylmethacrylate (PMMA) and polycarbonate materials. PMMA was obtained from a local glass supply store and cut to 30 cm x 5 cm x 3 mm with a 13mm diameter hole. It was sprayed with two layers of Rust-Oleum metallic paint on the back side enabling the acquisition of photoelastic data. The second sample was a 33 cm x 5 cm x 1.6 mm piece of aluminum with a 0.5 mm polycarbonate sheet (PS-1D), purchased from the Measurements Group, Inc. in Raleigh, North Carolina, epoxied to the front surface before a 13mm hole was drilled. The samples were placed in a hydraulic load frame, MTS 800, in order to subject them to vertical tension.

With a cyclic load of 5 Hz, thermoelastic data was obtained with the DeltaTherm 1000. This contains a 128 x 128 InSb array detector operating in the $3 - 5 \mu m$ wavelength region, with a spacial resolution of 0.1 mm and is capable of capturing

434 images per second (Stress Photonics, Madison, WI). Thirty seconds of data was collected and averaged to produce a stress map. The replacement of the DeltaTherm 1000 with the Model 030-Series Reflection Polariscope manufactured by the Measurements Group, Inc., Raleigh, NC, permitted the acquisition of photoelastic data under a static load. The thermoelastic and photoelastic results for a hole in plate under vertical tension for a polycarbonate sheet attached to aluminum is shown in Figure 2.3 and for a PMMA plate in Figure 2.4.

Photoelastic coatings must be securely cemented to the structure to ensure proper strain transmission. In most applications, an aluminum powder filled epoxy cement is used due to its excellent adhesion functions and added reflectivity [111]. After the strain measurements are complete, the coating needs to be removed to restore the object to its original state. There are three methods for removing the photoelastic coating – chemical, thermal, and mechanical. The chemical method involves submerging the test object in a solvent, such as methylene chloride, for a period of about 12 hours. For this method to work properly, bond failure between the coating and test part must be initiated at several points along the edge of the coating to allow the solvent to attack the adhesive. The second method of coating removal is by thermal methods. Heat alone will not remove the photoelastic coating, but it can be pried, scraped, or pulled off more easily when heated to about 100– 150°C. This method will require final finish cleaning of the surface by mechanical or chemical means to remove any remaining cement. The third technique involves various mechanical methods: when all else fails, the coating can always be removed by chipping, sand blasting, or grinding [112].

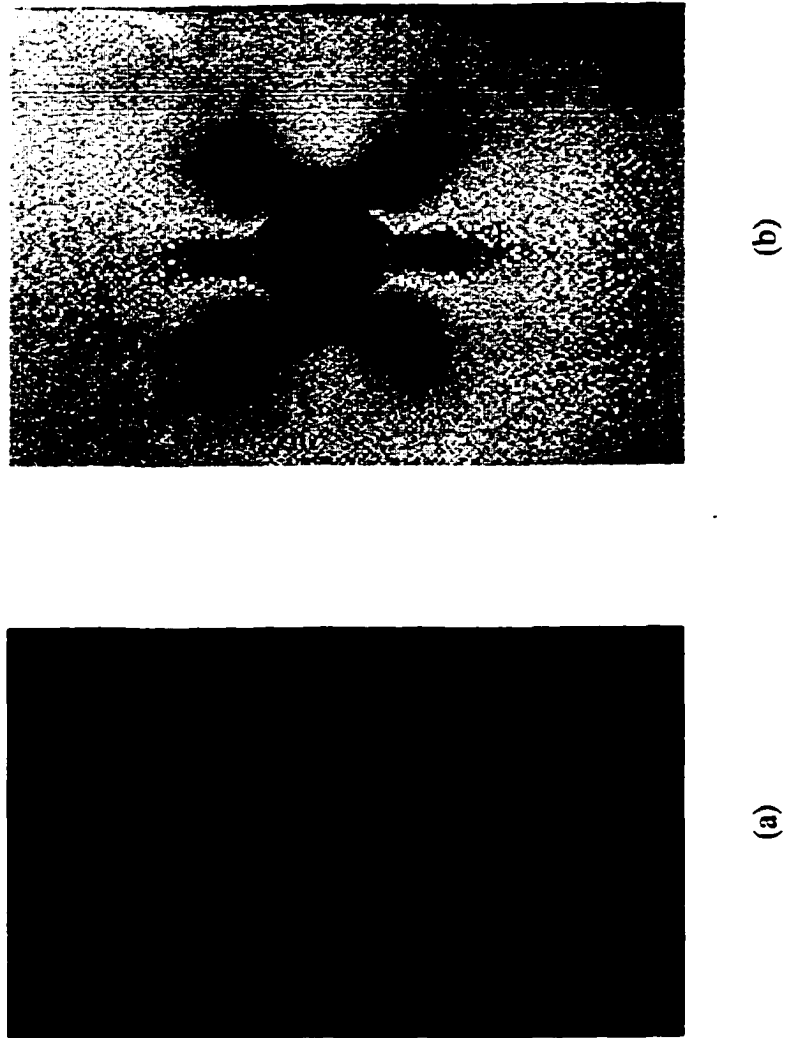


Figure 2.3. Thermoelectric (a) and photoelastic (b) responses from a polycarbonate sheet with a central hole under vertical tension.

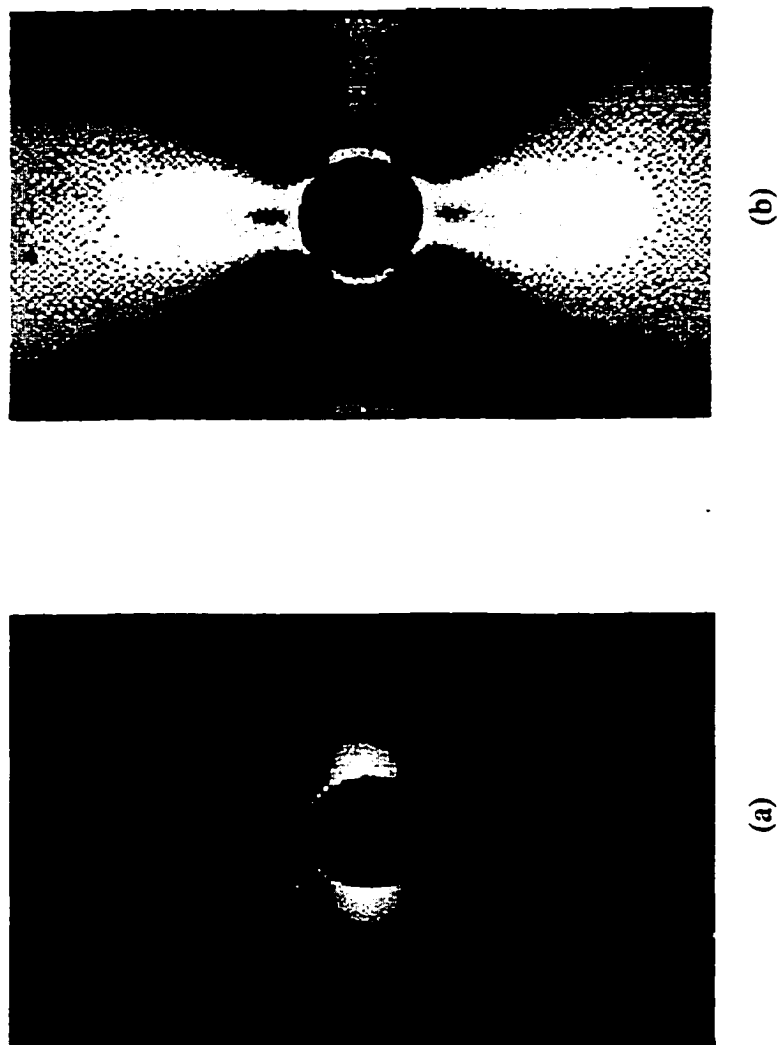


Figure 2.4. Thermoelastic (a) and photoelastic (b) responses from a PMMA bar with a central hole under vertical tension.

These methods of coating removal can be very harmful to the test object because it can be damaged by the solvents, heat, or mechanical efforts to chip the coating away using a hammer and a chisel. If the dual-use coating was tinted and sufficiently durable then it could be used as a “paint” for corrosion protection, aesthetics, etc., as well as for stress measurements on any structure or part in its natural environment.

Because of its durability and its photoelastic characteristics, epoxies are a top selection for the dual-use paint coating. The Measurements Group, Inc. sold a Bisphenol-A based Epoxy Resin (PSO-3) which was sprayed onto the surface of the object following the application of a reflective layer of diglycidyl ether of Bisphenol-A (RSO-3). This coating provided a rapid technique for covering parts, but it was difficult to control the coating uniformity and thickness and has since been taken off of the market. In spite of the problems, PSO-3 was tested as a dual-use coating.

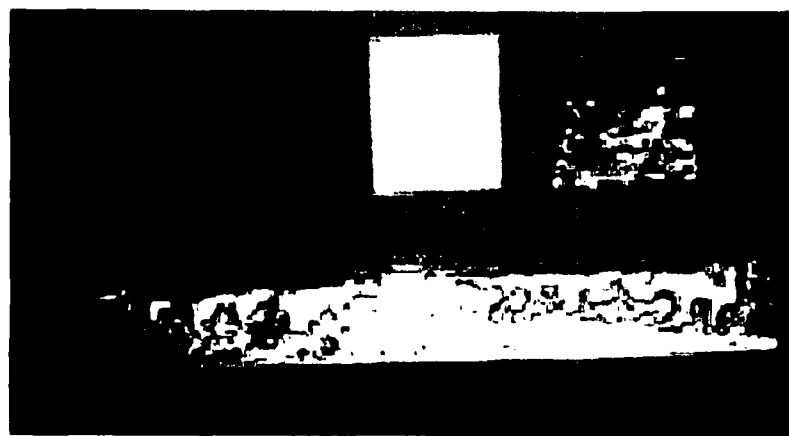
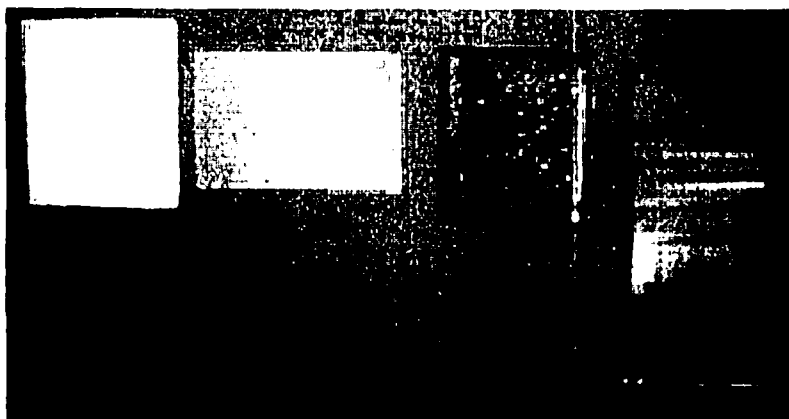
Coating candidates were not limited to ones in Table 2-1. Several birefringent polymer films were obtained from Dr. Catharine Fay of the Composites and Polymer Branch at the NASA Langley Research Center in Hampton, Virginia. The list included LaRC-1A Extruded film #5A, Kapton[®] HA, UPILEX[®] R, LaRC 8515, TOR, Kapton[®] HY, Teflon, Mylar, UPILEX[®] S, and LaRC - 1AX. These films varied in color from clear to a brownish-orange, in optical transmission from transparent to opaque in the visible, and in thickness from 25 μm to 75 μm . Although these materials were expected to be opaque in the infrared due to their chemical structure, testing of these films in the 3-5 μm IR showed differently. One possible reason was that the film was too thin to show total opaqueness. Increasing the thickness or the addition of other chemicals may have allowed the film to become totally opaque in the 3 – 5 μm IR

band. The investigation of these materials stopped at this point because PMMA and polycarbonate had already been identified as dual-use coating candidates and further chemical study on the birefringent polymers was out of the scope of this thesis.

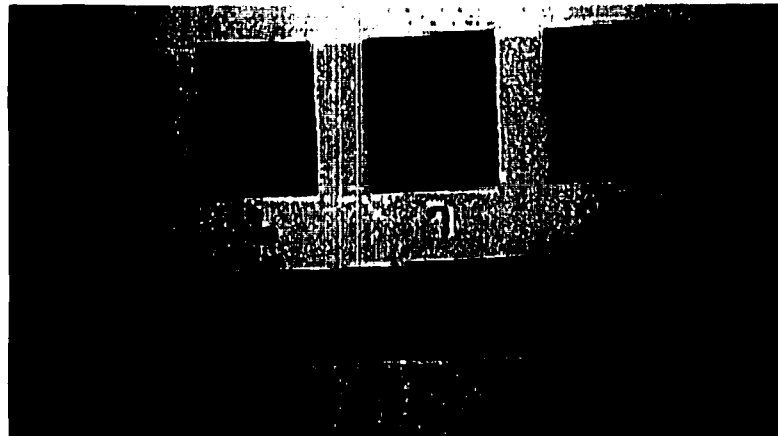
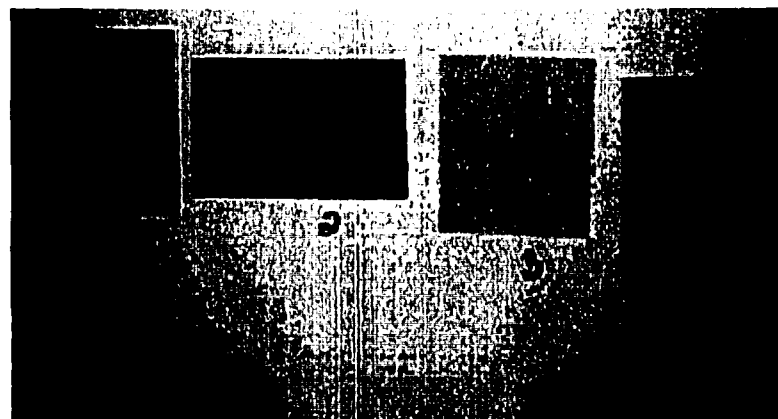
2.4 Reflective Backing

The backing layer in reflection photoelasticity consists of metal particles suspended in an epoxy or other adhesive. Because of the added width that this layer contributes to the overall thickness of the photoelastic coating, other products were compared in reflectance and in thickness to see if spray paints or other types of materials exhibited similar characteristics. Nine samples were selected, among them were Rust-Oleum Metallic Spray Paint (1), Rust-Oleum High Heat Gray Paint (2), MIL-P-53022B Gray Primer (3), Hydropox 4:1 Gray Epoxy (4), 20 μm Aluminum spheres suspended in (The Measurements Group) PSO-3 Photoelastic Coating (5), 20 μm aluminum spheres suspended in Elmer's Glue (6), (The Measurements Group) PS-1E photoelastic sheet with reflective backing (7), aluminum repair tape (8), and RSO-3 spray reflective backing (9). The function of this surface is to reflect the incident light without affecting its polarization. To test these nine samples as to their ability to preserve polarization upon reflection, they were placed in front of a reflection polariscope which illuminated each surface with vertically polarized light. The samples were then viewed through an analyzer with its polarization axis first parallel and then perpendicular to the incident light as shown in Figure 2.5.

Initial inspection of Figure 2.5 showed Rust-Oleum Metallic Spray Paint (1), Rust-



(a)



(b)

Figure 2.5. Various surfaces subjected to polarized light and observed through an analyzer that is (a) parallel and (b) perpendicular to the incident light. Material list given in the text.

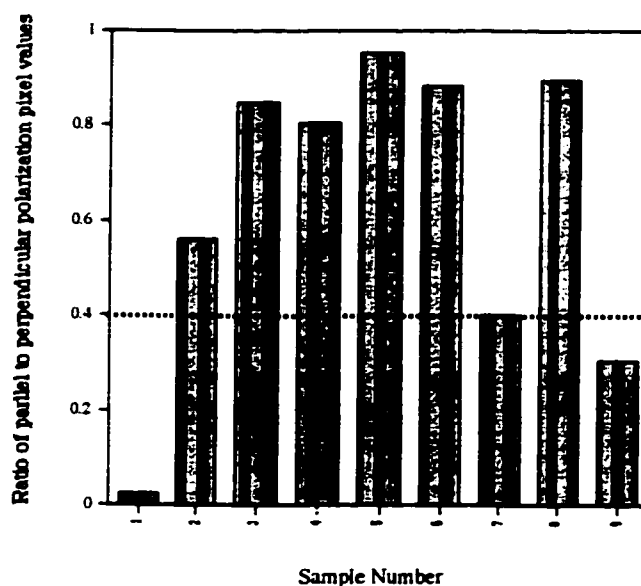


Figure 2.6. Ratio of the parallel to perpendicular polarization pixel values for reflection of surfaces 1 - 9. The industry standard is denoted by the dashed line for comparison.

Oleum High Heat Gray Paint (2), PS-1E photoelastic sheet with reflective backing (7), aluminum repair tape (8), and RSO-3 (9) had similar characteristics: they were bright with the analyzer parallel and dark with the analyzer perpendicular to the incident polarized light. The remaining materials all exhibited a gray appearance due to much of the light either being scattered away from the analyzer or the surface changed the polarization of the wave. Further analysis was done by calculating the ratio between pixel values in the parallel and perpendicular analyzer images and comparing it to the industry standard, sample 7, as seen in Figure 2.6. Ratios at or below the industry standard are materials that would work as well as the current available reflective backing. The metallic Rust-Oleum paint (1) possessed the lowest ratio followed by the RSO-3 (9). The Rust-Oleum High Heat Gray Paint (2) also preformed well as a reflective backing although its ratio was slightly larger. A small amount of saturation was observed in the parallel polarization image for the metallic Rust-Oleum paint (1)

which could have lowered the calculated ratio. Estimates indicate a corrected ratio value of approximately 0.05.

It was clear from this analysis that the Metallic Rust-Oleum paint performed as well as the industry standard at a substantially smaller thickness, 10 μm for the paint and 250 μm for the backing plus adhesive. This material, in combination with other identified birefringent coatings, was a candidate for the dual-use coating “paint” described earlier.

2.5 Deposition

Various combinations of birefringent coatings and reflective backings were prepared for testing. PSO-3 was applied using a Paasche Airbrush to a thoroughly cleaned 33 cm x 5 cm x 1.6 mm piece of aluminum which was heated to 35°C. Several problems were encountered with the application of this material to the aluminum, the main one being the spraying of the epoxy because of clogging in the airbrush.

The airbrush was equipped with two different types of containers to hold paint – a small jar with a plastic straw in the cap and a small metal cup. Very little of the epoxy was sprayed onto the sample when the small jar was used even with increased air pressure. When the jar was replaced with the small metal cup, flow of the epoxy through the airbrush onto the sample was easier. The differences between the containers were with the jar set-up pulling the material up through a plastic straw compared to the metal cup having a small tube at the bottom. It was suspected that the epoxy stuck to the plastic straw causing a decrease in flow during application. W. E. Witzell also

encountered difficulty when spraying photoelastic coatings. His primary problem was with the epoxy setting up in the spray gun during the application. When he was able to have the material pass through the spray gun uninterrupted by either controlling the temperature of the exothermic reaction or varying the amount of the catalyst, he found longer curing times and runs in the coating on the surface [113].

Once the coating was applied to the object, the epoxy was allowed to cure for 24 hours at room temperature or for about 20 minutes at 93°C. When left to cure at room temperature, humidity kept the material tacky for days while the use of an oven and hot-plate yielded samples that sometimes contained bubbles. The formation of the bubbles was not suspected to be related to the spraying technique because there was no evidence of them once the spraying was complete. The use of a dry box assisted in the removal of humidity during room temperature drying but was not always successful and available for use. Replacement of the airbrush with an ordinary paint brush resulted in a few better samples but the main difficulty with curing remained. Difficulty with this product was not unique to this research. PSO-3 and RSO-3 have since been taken off of the market because of their difficulty in application.

Other combinations of materials were tested. Among them was TOR on Rust-Oleum gray high heat paint. It was found that the N-Methyl-2-Pyrrolidone solvent for the TOR rewet the dried paint giving it the appearance of paint stripper on an old piece of furniture. Next was PMMA dissolved in xylenes applied on Rust-Oleum metallic paint. Once the solvent evaporated in a dry box, there was significant evidence that the xylenes interacted with the paint because the surface showed signs of bubbling and streaking. Inspection of the contents of the metallic paint showed it to contain toluene

and xylenes. With the solvent of the PMMA identical to chemicals used in the spray paint, it would rewet the paint causing some mixing between the two layers. However, when the paint was replaced by a metallic suspended epoxy, the PMMA deposited on the surface nicely. Work with other materials such as poly-Bisphenol-A Carbonate produced films that curled up on themselves once the solvent evaporated. Conversations with Dr. Floyd Klavetter, from the Department of Applied Science at the College of William and Mary, attributed this effect to the lack of a polar surface for the adherence of the polymer. The coating found itself more polar than the substrate, resulting in the curling of the film upon drying.

Although the surface requirements for thermoelastic and photoelastic stress analysis seem to be in opposition to each other, polycarbonate and PMMA have shown promise. Not only are they birefringent in the visible but they are also opaque in the infrared preventing the thermographic imager from seeing the low emissive reflective backing. These coatings were used to collect both thermoelastic and photoelastic data which were then combined to determine the full-field stress tensor components. Before any data analysis, the theory behind fringe generation and heat production must be understood to ensure confidence in the calculated stress values. These theories were united in a computer code to simulate the thermoelastic stress maps and photoelastic fringes. Of the two theories, it was birefringence that was the most challenging to model.

Chapter 3

Photoelastic Theories

James Maxwell developed the one-dimensional theory of photoelasticity because of David Brewster's observations. More recently, increased understanding in the fields of optics, elasticity, and electromagnetics have provided additional explanations of birefringence. The following is a description of the one-dimensional theory followed by a modern optical and electromagnetic analysis. The objective is to combine all three theories into a model that will be able to generate photoelastic fringes. Errors, such as non-retroreflection, will be systematically introduced into the model and the effects observed in the resulting fringe patterns. How the modified photoelastic data influences the calculation of the full-field stress tensor is of significant interest to this thesis.

3.1 One-Dimensional Theory

As a material is subjected to an applied stress, the density of the object changes resulting in a modified index of refraction. Some optically isotropic materials become anisotropic when subjected to an applied load resulting in the propagating light wave being decomposed into an ordinary and extraordinary wave each having different velocities and polarizations orthogonal to one another. The relative retardation, δ , between these waves is the difference in their optical path lengths,

$$\delta = d(n_e - n_o), \quad (3.1)$$

where n_e and n_o are the indices of refraction for the extraordinary and ordinary waves, respectively, and d is the thickness of the medium. Brewster's Law connects the difference in the indices of refraction with the difference in the principal strains by

$$(n_x - n_y) = K (\epsilon_x - \epsilon_y) \quad (3.2)$$

where K is defined as the strain-optic coefficient and is a property of the material, and ϵ_x and ϵ_y are the principal strains. The combination of equations (3.1) and (3.2) yields the photoelastic equation for reflection

$$(\epsilon_x - \epsilon_y) = \frac{\delta}{2dK} = \frac{N\lambda}{2dK}, \quad (3.3)$$

where N is the fringe order number.

Photoelastic fringes are observed through a polariscope which reveals two sets of fringes. A plane polariscope produces linear polarized light which is incident upon a strained sample coated with a birefringent material, and the reflected light is analyzed by a second linear polarizer set perpendicular to the first, as depicted in Figure 3.1. The intensity of the light passing through the second polarizer has the form

$$I = a^2 \sin^2 2(\beta - \alpha) \sin^2 \frac{\pi\delta}{\lambda}, \quad (3.4)$$

where α is the angle between the polarization axis of the first polarizer and the y-axis and β is the angle between the principal x-axis and the y-axis. The intensity becomes zero when the crossed polarizers become parallel to the direction of the principal strains in the coating. Thus, a plane polariscope is set-up to measure principal strain direction. The images used to determine this quantity are called isoclinic fringes

Placing quarter-wave plates after the polarizer and before the analyzer converts the linear polariscope into a circular polariscope, as seen in Figure 3.2, which produces a

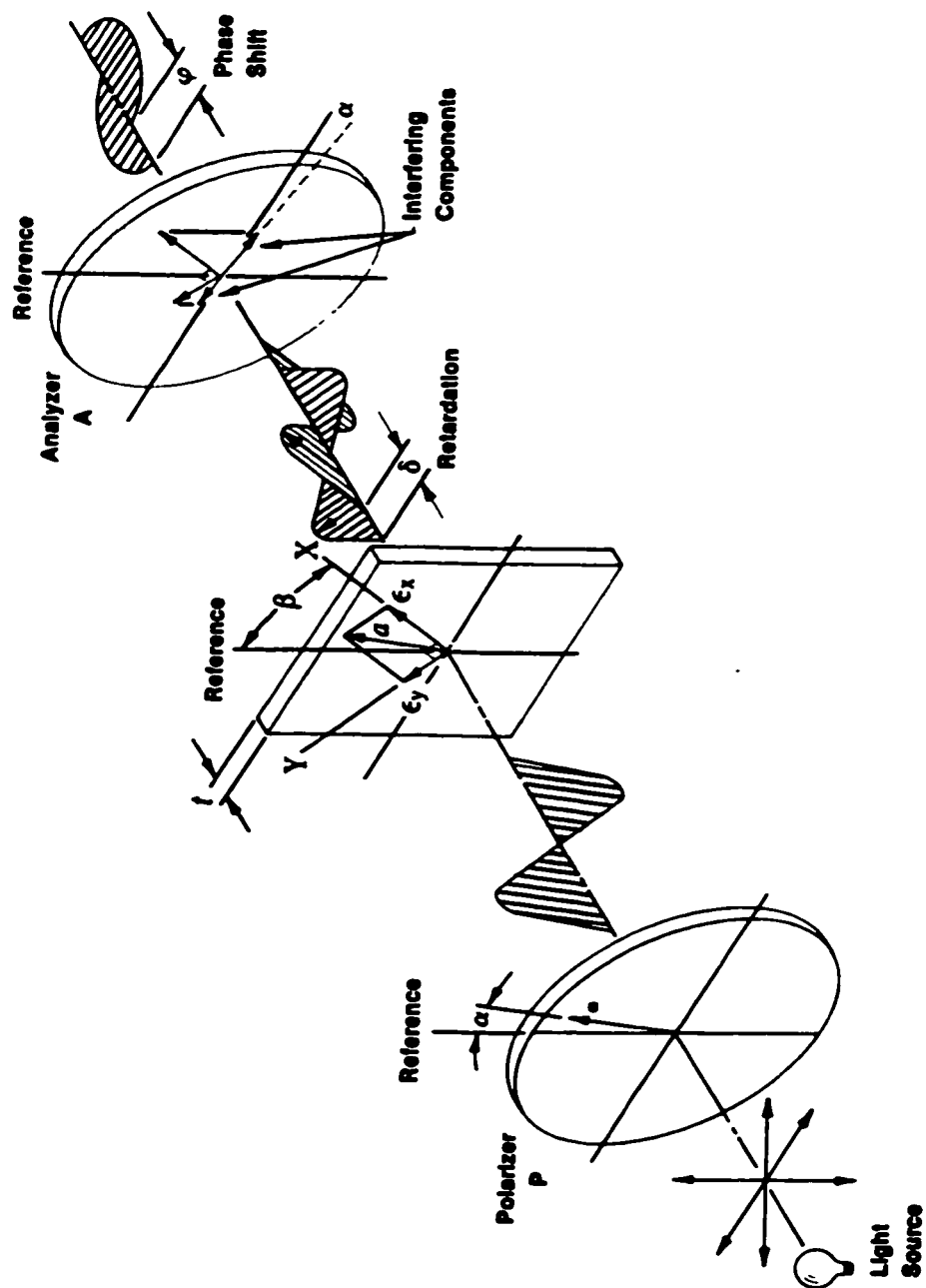


Figure 3.1. Plane Polariscroscope [114].

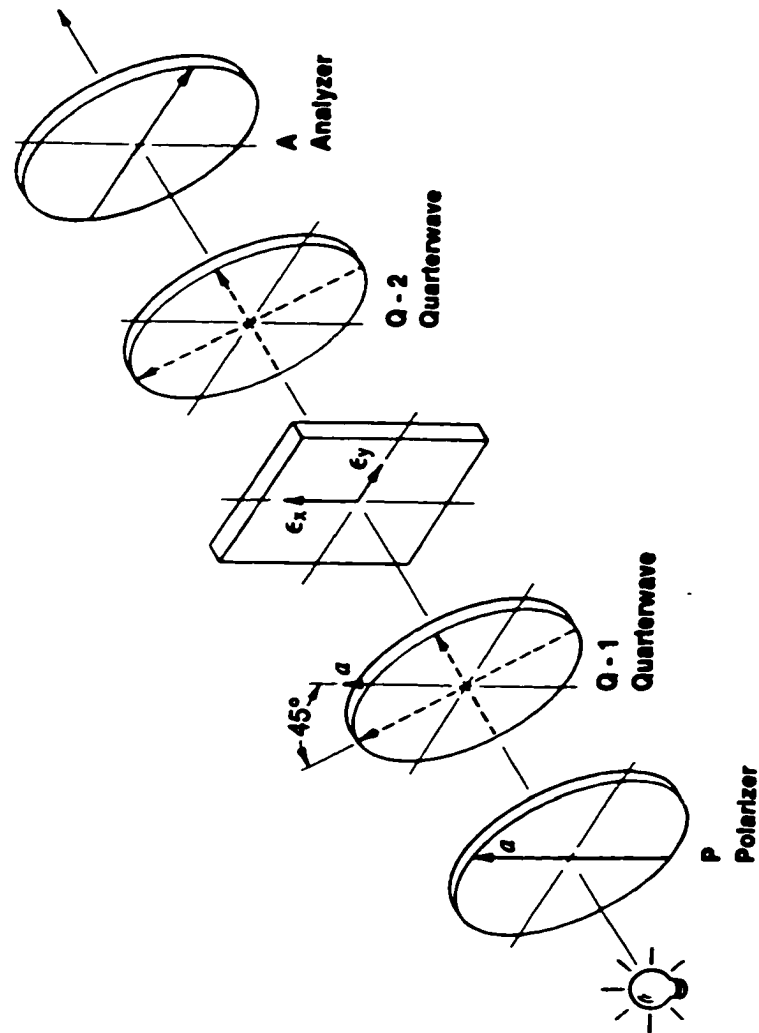


Figure 3.2. Circular Polariscopes [114].

different set of fringes. The intensity of light emerging from a circular polariscope is

$$I = a^2 \sin^2 \frac{\pi \delta}{\lambda}, \quad (3.5)$$

and becomes zero when $\delta = N\lambda$. Thus a circular polariscope is setup to measure the difference of the principal strains, referred to as isochromatic fringes [114].

This level of theory is adequate for experimental determination of fringe order, N , and strain direction, but offers little insight into the anisotropic characteristics of the material. A more defined picture is formed with the investigation of light waves propagating through a stressed material.

3.2 Modern Optics

Anisotropic materials have physical properties that vary with direction. Assuming the material is isotropic with regards to magnetic permeability, μ , anisotropic for the permittivity, ϵ , and is a lossless medium, the impermeability tensor, \mathfrak{a}_j , can be defined from the relationship between the electric field vector, \mathbf{E} , and the electric displacement, \mathbf{D} ,

$$E_i = \sum_{j=1}^3 \mathfrak{a}_j D_j. \quad (3.6)$$

In general there are nine elements associated with the impermeability tensor but energy consideration, such as the energy of the electromagnetic field and the energy flux (Poynting vector) which are valid for isotropic materials are also valid for anisotropic materials. In addition the assumption of no energy loss in the medium results in the permeability tensor being Hermitian, will reduce the tensor to six or less independent elements.

Properties of the impermeability tensor can be understood through the use of a geometric surface, called the optical indicatrix, generated from the electric energy density equation,

$$2U_E = \mathbf{D} \cdot \mathbf{E}. \quad (3.7)$$

This can be rewritten as

$$\frac{D_x^2}{2U_E \epsilon_x} + \frac{D_y^2}{2U_E \epsilon_y} + \frac{D_z^2}{2U_E \epsilon_z} = 1 \quad (3.8)$$

by substituting the principal values of the electric displacement for the electric field vector. This equation expresses an ellipsoid whose semiaxes equal the square root of the principal dielectric constants and is known as the optical indicatrix. It should be noted that other studies of anisotropy label this ellipsoid as the index ellipsoid, reciprocal ellipsoid, poinsot ellipsoid, and the ellipsoid of wave normals.

The optical indicatrix is used to determine the electric field, \mathbf{E} , the propagation vector \mathbf{k} , and the Poynting vector, \mathbf{S} , given the displacement vector, \mathbf{D} . Alternatively it can determine \mathbf{D} and \mathbf{E} given \mathbf{k} . Drawing the propagation vector from the center of ellipsoid in the appropriate direction, a plane normal to propagation vector slices the ellipsoid forming an ellipse. The principal semiaxes of this ellipse are proportional to the indices of refraction, n_1 and n_2 , and coincide with \mathbf{D}_1 and \mathbf{D}_2 , two orthogonal polarizations for the wave with wave vector \mathbf{k} , as illustrated in Figure 3.3. For certain directions of \mathbf{k} , the plane normal to \mathbf{k} will cut the ellipsoid forming a circle. These special directions are referred to as the *optic axes* of the material. If there is only one such direction, the material is referred to as uniaxial, and a material with two special directions, is called a biaxial material.

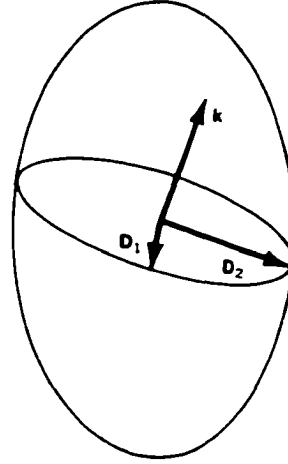


Figure 3.3. Optical indicatrix ellipsoid intersected by a plane perpendicular to the propagation vector \mathbf{k} forming an ellipse. The principal semi-axes of the ellipse coincide with \mathbf{D}_1 and \mathbf{D}_2 and are proportional to the indices of refraction n_1 and n_2 [115].

As stated above, the principal axes for the ellipse are proportional to the indices of refraction. Through the use of Fresnel's equation written as (see Appendix A for details)

$$\sum_{j=1}^3 \frac{k_j^2}{k^2 (n^2 - n_j^2)} = \frac{1}{n^2}, \quad (3.9)$$

the relationship between the propagation direction and the index of refraction can be determined. This equation is quadratic with respect to n and has two positive roots, n_1^2 and n_2^2 , which are squares of the principal indices of refraction. They are related to the impermeability tensor by

$$\mathfrak{A} = \frac{1}{n_i^2} = \frac{\epsilon_0}{\epsilon_i}, \quad (3.10)$$

where ϵ_i is the principal permittivity in the material and ϵ_0 is the permittivity of free space. Because applying a force to an isotropic material produces a small change in the index of refraction, the impermeability tensor can be expanded in a power series of the total applied field,

$$\mathfrak{A}_k = \mathfrak{A}_{ik}^{(0)} + q_{ijkm} T_{jm} \quad \text{for stress and} \quad (3.11a)$$

$$\mathfrak{A}_k = \mathfrak{A}_{ik}^{(0)} + p_{ijkm} S_{jm} \quad \text{for strain.}$$

The tensors q and p contain the stress-optic values and the strain-optic values, respectively, of the coating and are related through the elastic stiffness constants by

$$p_{ijkl} = q_{ijmn} C_{mnkl}. \quad (3.12)$$

The waves associated with n_1 and n_2 from Fresnel's equation are referred to as the ordinary and extraordinary waves respectively which have a phase difference of

$$\delta = k_0 L (n_1 - n_2) \quad (3.13)$$

where L is the thickness of the material. The physical interpretation of this equation is seen when the relative retardation, δ , is incorporated into an equation which converts the phase difference into an intensity of light transmitted through crossed polarizers,

$$I_{\max} = A^2 \sin^2 \left(\frac{\delta}{2} \right). \quad (3.14)$$

With monochromatic light, the contours of equal intensity determined by equation (3.14) represent contours of equal stress [115].

This analysis connects the impermeability tensor to the induced stress in a material and permits the calculation of the fringes. Modern optics predicts the two waves propagating in the anisotropic medium but does not provide a mathematical expression for them. Equations for the ordinary and extraordinary waves are found when exploring electromagnetic wave theory.

3.3 Electromagnetic Wave Theory

The fundamental equations for electromagnetic wave theory were established in 1873 by James Clerk Maxwell and experimentally verified by Heinrich Hertz in

1888. This elegant theory embodies many principles and concepts which served as fundamental rules of nature and forms a vital link to other scientific disciplines.

Maxwell's equations can be written as

$$\nabla \times \mathbf{E}(\mathbf{r}, t) + \frac{\partial}{\partial t} \mathbf{B}(\mathbf{r}, t) = 0 \quad (3.15a)$$

$$\nabla \times \mathbf{H}(\mathbf{r}, t) - \frac{\partial}{\partial t} \mathbf{D}(\mathbf{r}, t) = \mathbf{J}(\mathbf{r}, t) \quad (3.15b)$$

$$\nabla \cdot \mathbf{B}(\mathbf{r}, t) = 0 \quad (3.15c)$$

$$\nabla \cdot \mathbf{D}(\mathbf{r}, t) = \rho(\mathbf{r}, t) \quad (3.15d)$$

where \mathbf{E} is the electric field strength, \mathbf{B} is the magnetic flux density, \mathbf{H} is the magnetic field strength, \mathbf{D} is the electric displacement, \mathbf{J} is the electric current density, and ρ is the electric charge density. These relations are the fundamental laws governing the behavior of electromagnetic fields in free space and in media. No reference has been made here to specific material properties which would provide connections to other disciplines of physics, such as plasma physics, continuum mechanics, solid-state physics, thermodynamics, etc. The behavior of the electromagnetic waves in the presence of a medium, whether it is diffracted, refracted, or scattered, is of primary interest over deformation or movement of the medium. Thus the constitutive relations characterize a material medium according to its various properties. For an isotropic material

$$\mathbf{D} = \epsilon \mathbf{E} \quad (3.16a)$$

$$\mathbf{B} = \mu \mathbf{H}. \quad (3.16b)$$

An isotropic material is defined as one in which the field vector \mathbf{E} is parallel to \mathbf{D} and the field vector \mathbf{H} is parallel to \mathbf{B} . Inside the material the permittivity, ϵ , is determined

by the electrical properties of the medium and the permeability, μ , by the magnetic properties of the medium.

More generally, a material is described by its permittivity tensor,

$$\epsilon = \begin{pmatrix} \epsilon_{xx} & \epsilon_{xy} & \epsilon_{xz} \\ \epsilon_{yx} & \epsilon_{yy} & \epsilon_{yz} \\ \epsilon_{zx} & \epsilon_{zy} & \epsilon_{zz} \end{pmatrix}. \quad (3.17)$$

When rotated to the principal optical axes, the this matrix has the form

$$\epsilon = \begin{bmatrix} \epsilon_x & 0 & 0 \\ 0 & \epsilon_y & 0 \\ 0 & 0 & \epsilon_z \end{bmatrix}, \quad (3.18)$$

with ϵ_x , ϵ_y , and ϵ_z referring to the principal axes of the crystal. For cubic crystals, the diagonal elements are equal and the material is considered optically *isotropic*. In tetragonal, hexagonal, and rhombohedral crystals, two of the three parameters are equal. Such crystals are optically *uniaxial* exhibiting a two-dimensional degeneracy; the principal axis that exhibits this anisotropy is called the *optic axis*. For a crystal with the z-axis as the optic axis, it is regarded as *positive uniaxial* if $\epsilon_z > \epsilon$ and *negative uniaxial* if $\epsilon_z < \epsilon$. In orthorhombic, monoclinic, and triclinic crystals, all three crystallographic axes are unequal making the medium optically *biaxial*.

In this study, time-harmonic (monochromatic or continuous) waves will be considered. The benefit of using such waves are (1) the continuous wave assumption can be used to eliminate the time dependence in Maxwell's equations and thus considerably simplifying the mathematics; (2) once the continuous wave case is solved

and a sound understanding is developed for the frequency-domain phenomena, Fourier theory can be applied to study the time-domain phenomena; and (3) continuous wave representation covers the whole spectrum of electromagnetic waves. For a continuous wave, Maxwell equations (3.15a-d) are rewritten as

$$\nabla \times \mathbf{E} = i\omega\mathbf{B} \quad (3.19a)$$

$$\nabla \times \mathbf{H} = -i\omega\mathbf{D} + \mathbf{J} \quad (3.19b)$$

$$\nabla \cdot \mathbf{B} = 0 \quad (3.19c)$$

$$\nabla \cdot \mathbf{D} = 0. \quad (3.19d)$$

In a source-free region, $\mathbf{J} = \rho = 0$, plane waves of the form $e^{i\mathbf{k}\cdot\mathbf{r}}$ convert these equations to

$$\mathbf{k} \times \mathbf{E} = \omega\mathbf{B} \quad (3.20a)$$

$$\mathbf{k} \times \mathbf{H} = -\omega\mathbf{D} \quad (3.20b)$$

$$\mathbf{k} \cdot \mathbf{B} = 0 \quad (3.20c)$$

$$\mathbf{k} \cdot \mathbf{D} = 0. \quad (3.20d)$$

From these equations it is obvious that the electric displacement and magnetic flux density are always perpendicular to the wave vector, \mathbf{k} . The plane containing both \mathbf{D} and \mathbf{B} is referred to as the DB plane. For a medium with $\mathbf{B} = \mu\mathbf{H}$, the vector \mathbf{H} also lies in the DB plane. If the medium is anisotropic with respect to permittivity, the electric field vector may not lie in the DB plane. For this reason the polarization of the plane wave will be denoted by the vector electric displacement instead of the electric field.

To facilitate discussions of wave behavior and solutions for the field vectors inside a homogeneous medium, a new coordinate system is needed. This new coordinate

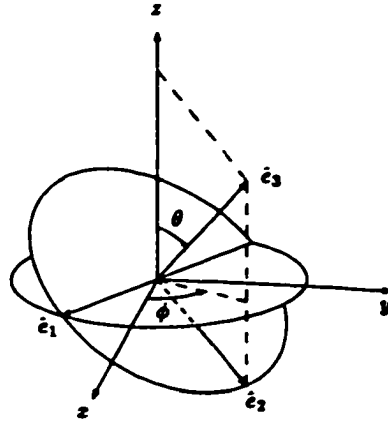


Figure 3.4. The kDB coordinate system as related to the cartesian axes [116].

system will consist of the propagation vector and the DB plane and be referred to as the kDB system. This system has three unit vectors \hat{e}_1 , \hat{e}_2 , and \hat{e}_3 where \hat{e}_3 is defined as the direction of propagation vector as shown in Figure 3.4. The transformation between the kDB system and the Cartesian system is given by

$$\mathbf{T}_{trans} = \begin{pmatrix} \sin \phi & -\cos \theta & 0 \\ \cos \theta \cos \phi & \sin \theta \cos \phi & -\sin \theta \\ \sin \theta \cos \phi & \sin \theta \sin \phi & \cos \theta \end{pmatrix}. \quad (3.21)$$

Within the frame of the kDB system, equations (3.20a-d) take the form

$$\mathbf{k} \times \mathbf{E}_{kDB} = \omega \mathbf{B}_{kDB} \quad (3.22a)$$

$$\mathbf{k} \times \mathbf{H}_{kDB} = -\omega \mathbf{D}_{kDB} \quad (3.22b)$$

$$\mathbf{k} \cdot \mathbf{B}_{kDB} = 0 \quad (3.22c)$$

$$\mathbf{k} \cdot \mathbf{D}_{kDB} = 0. \quad (3.22d)$$

When $\mathbf{k} = \hat{e}_3 k$, $B_3 = D_3 = 0$ and the constitutive relations written as

$$\mathbf{E}_{kDB} = \boldsymbol{\kappa}_{kDB} \cdot \mathbf{D}_{kDB} \quad (3.23a)$$

$$\mathbf{H}_{kDB} = \mu \mathbf{B}_{kDB}, \quad (3.23b)$$

equations (3.22a) and (3.22b) can be written in matrix form as

$$\begin{pmatrix} \kappa_{11} & \kappa_{12} \\ \kappa_{21} & \kappa_{22} \end{pmatrix} \begin{pmatrix} D_1 \\ D_2 \end{pmatrix} = \begin{pmatrix} 0 & \mu \\ -\mu & 0 \end{pmatrix} \begin{pmatrix} B_1 \\ B_2 \end{pmatrix} \quad (3.24)$$

and

$$\nu \begin{pmatrix} B_1 \\ B_2 \end{pmatrix} = \begin{pmatrix} 0 & -\mu \\ \mu & 0 \end{pmatrix} \begin{pmatrix} D_1 \\ D_2 \end{pmatrix} \quad (3.25)$$

where $u = \omega/k$, $\kappa = 1/\epsilon$, and $\nu = 1/\mu$.

The tensor κ is called the impermeittivity tensor. In a uniaxial medium with the optic axis in the \hat{z} direction, the impermeittivity tensor has the form

$$\kappa = \begin{pmatrix} \kappa & 0 & 0 \\ 0 & \kappa & 0 \\ 0 & 0 & \kappa_z \end{pmatrix}. \quad (3.26)$$

Transformation to the kDB system by $\kappa_{kDB} = \mathbf{T}_{trans} \cdot \kappa \cdot \mathbf{T}_{trans}^{-1}$ yields

$$\kappa_{kDB} = \begin{pmatrix} \kappa & 0 & 0 \\ 0 & \kappa \cos^2 \theta + \kappa_z \sin^2 \theta & (\kappa - \kappa_z) \sin \theta \cos \theta \\ 0 & (\kappa - \kappa_z) \sin \theta \cos \theta & \kappa \sin^2 \theta + \kappa_z \cos^2 \theta \end{pmatrix} \quad (3.27)$$

.Using this result in equations (3.24-25) produces

$$\begin{pmatrix} \kappa_{11} & 0 \\ 0 & \kappa_{22} \end{pmatrix} \begin{pmatrix} D_1 \\ D_2 \end{pmatrix} = \begin{pmatrix} 0 & \mu \\ -\mu & 0 \end{pmatrix} \begin{pmatrix} B_1 \\ B_2 \end{pmatrix} \quad (3.28)$$

and

$$\nu \begin{pmatrix} B_1 \\ B_2 \end{pmatrix} = \begin{pmatrix} 0 & -\mu \\ \mu & 0 \end{pmatrix} \begin{pmatrix} D_1 \\ D_2 \end{pmatrix}. \quad (3.29)$$

Eliminating \mathbf{B} from these results in the relationship

$$\begin{pmatrix} u^2 - \nu\kappa_{11} & 0 \\ 0 & u^2 - \nu\kappa_{22} \end{pmatrix} \begin{pmatrix} D_1 \\ D_2 \end{pmatrix} = 0. \quad (3.30)$$

Four cases satisfy (3.30). The first is $D_1 = D_2 = 0$ implying no field. The second case is $D_1 \neq 0$ and $D_2 = 0$ which corresponds to a linearly polarized wave in the \hat{e}_1 direction with a phase velocity of

$$u = \pm \sqrt{\nu\kappa_{11}} = \pm \sqrt{\nu\kappa}. \quad (3.31)$$

Case three is $D_1 = 0$ and $D_2 \neq 0$ corresponding to a linearly polarized wave in the \hat{e}_2 direction with a phase velocity of

$$u = \pm \sqrt{\nu\kappa_{22}} = \pm \sqrt{\nu(\kappa \cos^2 \theta + \kappa_z \sin^2 \theta)}. \quad (3.32)$$

Case four has $D_1 \neq 0$ and $D_2 \neq 0$ which only occurs if $\kappa_{11} = \kappa_{22}$ and is only true for an isotropic medium or the propagation direction along the optic axis.

The result of these two waves propagating with different phase velocities in a medium is called birefringence. When an electromagnetic wave enters an optically uniaxial medium, it decomposes into two linearly polarized waves. With the y-axis perpendicular to the front surface and the z-axis as the optic axis, the spacial dependence of the \mathbf{D} vector becomes [116]

$$D = \hat{x} D_o \exp \left[\frac{i\omega y}{\sqrt{\nu\kappa}} \right] + \hat{z} D_e \exp \left[\frac{i\omega y}{\sqrt{\nu\kappa_z}} \right]. \quad (3.33)$$

Conversion of this equation to an electric field vector provides the necessary equation for the material propagating wave. Used in combination with equations for an incident and reflected wave, an anisotropic electromagnetic boundary value problem can be established which will enable the calculation of photoelastic fringes. This method is preferred over the other theories in that errors can be systematically incorporated into the model and their effects observed in the resulting fringe patterns. In the next chapter this model will be tested on a hole in a plate, a hole with a notch, and two holes in a plate under vertical tension for comparison to experimental results.

Chapter 4

Anisotropic Electromagnetic Boundary Value Problem

The motivation to develop an alternate description of the photoelastic effect evolved from the inability of the existing theories to relate parameters, such as angle of incidence and surface roughness, to observe the effects on the resulting photoelastic fringes. The anisotropic electromagnetic boundary value model will combine electromagnetic wave theory and modern optics with appropriate electromagnetic boundary conditions to produce photoelastic fringe patterns for comparison with laboratory observations. This method is non-graphical and capable of producing the phase and amplitude of all incident, reflected, and material propagating waves.

4.1 Isoclinic Model

Consider a plane electromagnetic wave traveling in the negative z -direction normally incident upon a birefringent coating of thickness d with the x and y axes in the plane of the material. The plane wave will pass through a polarizer aligned along the y axis, interact with the stressed medium, and then pass through an analyzer aligned along the x axis as seen in Figure 4.1. Two coordinate systems will be utilized in this model – the kDB system for the material frame and Cartesian for the analyzer and polarizers in the lab frame.

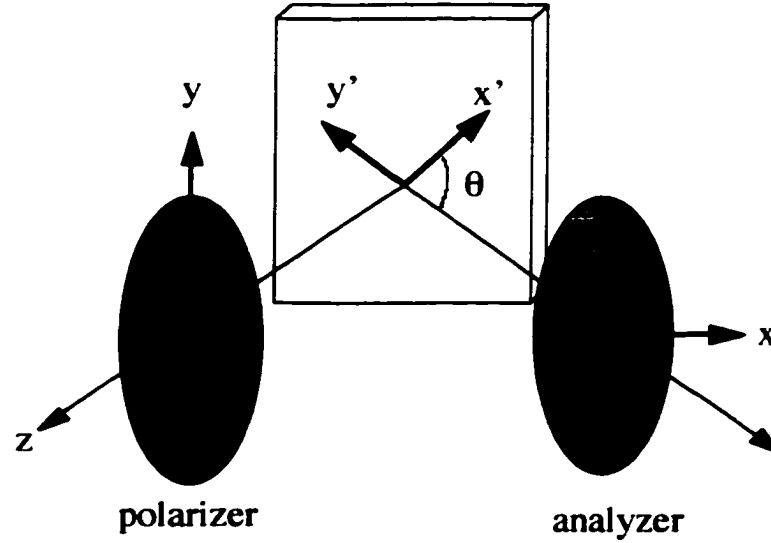


Figure 4.1. Set-up for the isoclinic model.

The unloaded material is optically isotropic requiring the material frame (kDB) to be aligned to that of the lab system (Cartesian). From Figure 3.4, it is clear that $\theta_{kDB} = 0^\circ$ and $\phi_{kDB} = 90^\circ$. Substitution of these values into the transformation equation (3.21) yields

$$\mathbf{T}_{trans} = \begin{pmatrix} 1 & 0 & 0 \\ 0 & 1 & 0 \\ 0 & 0 & 1 \end{pmatrix}. \quad (4.1)$$

The kDB coordinates, \mathbf{r}_{kDB} , are related to the Cartesian coordinates, \mathbf{r} , by $\mathbf{r}_{kDB} = \mathbf{T}_{trans} \cdot \mathbf{r} \cdot \mathbf{T}_{trans}^{-1}$ which, when written explicitly, yields

$$\hat{e}_1 = \hat{x}, \hat{e}_2 = \hat{y}, \text{ and } \hat{e}_3 = \hat{z}. \quad (4.2)$$

When an external load is applied to the material, it becomes optically anisotropic. For a material under in-plane uniaxial tension, the relation between the impermeability

tensor and the applied load, as given in equation (3.11a), can be written as

$$\begin{pmatrix} \varepsilon_{xx} \\ \varepsilon_{yy} \\ \varepsilon_{zz} \\ \varepsilon_{yz} \\ \varepsilon_{zx} \\ \varepsilon_{xy} \end{pmatrix} = \begin{pmatrix} \varepsilon^{(0)} \\ \varepsilon^{(0)} \\ \varepsilon^{(0)} \\ 0 \\ 0 \\ 0 \end{pmatrix} + \begin{pmatrix} p_{xx} & p_{xy} & p_{xy} & 0 & 0 & 0 \\ p_{xy} & p_{xx} & p_{xy} & 0 & 0 & 0 \\ p_{xy} & p_{xy} & p_{xx} & 0 & 0 & 0 \\ 0 & 0 & 0 & p_{zz} & 0 & 0 \\ 0 & 0 & 0 & 0 & p_{zz} & 0 \\ 0 & 0 & 0 & 0 & 0 & p_{zz} \end{pmatrix} \begin{pmatrix} T_{xx} \\ 0 \\ 0 \\ 0 \\ 0 \\ 0 \end{pmatrix} \quad (4.3)$$

where $p_{zz} = p_{xx} - p_{xy}$ and the stress-optic coefficients, p , are for an isotropic material.

Writing the new impermeability tensor in a normal matrix form results in

$$\varepsilon = \begin{pmatrix} \varepsilon^{(0)} + p_{xx}T_{xx} & 0 & 0 \\ 0 & \varepsilon^{(0)} + p_{xy}T_{xx} & 0 \\ 0 & 0 & \varepsilon^{(0)} + p_{xy}T_{xx} \end{pmatrix}. \quad (4.4)$$

When compared to equation (3.26), (note the relation between impermeability and permittivity is $\varepsilon = \varepsilon_0 \kappa$), this equation signifies an optically uniaxial medium with the optic axis along the x axis in the material. For convenience the material coordinates will not be labeled \hat{e}_1 or \hat{e}_2 but rather x' and y' and be referred to as the principal stress axes. From the one-dimensional theory of photoelasticity, the angle of polarizer/analyzer unit and the angle of the principal axes will vary. The polarizer will be aligned along y and the analyzer along x . The angle ϕ will measure the rotation of the crossed analyzer/polarizer unit from the y axis and the angle θ will measure the rotation of the principal axes from the x axis.

The general expression for a CW, linearly polarized, normal incidence light wave is

$$\vec{E}_I = (\hat{x} \cos \phi + \hat{y} \sin \phi) A e^{-ik_0 z}. \quad (4.5)$$

This is incident upon the stressed medium and must be rotated to the kDB system for further analysis,

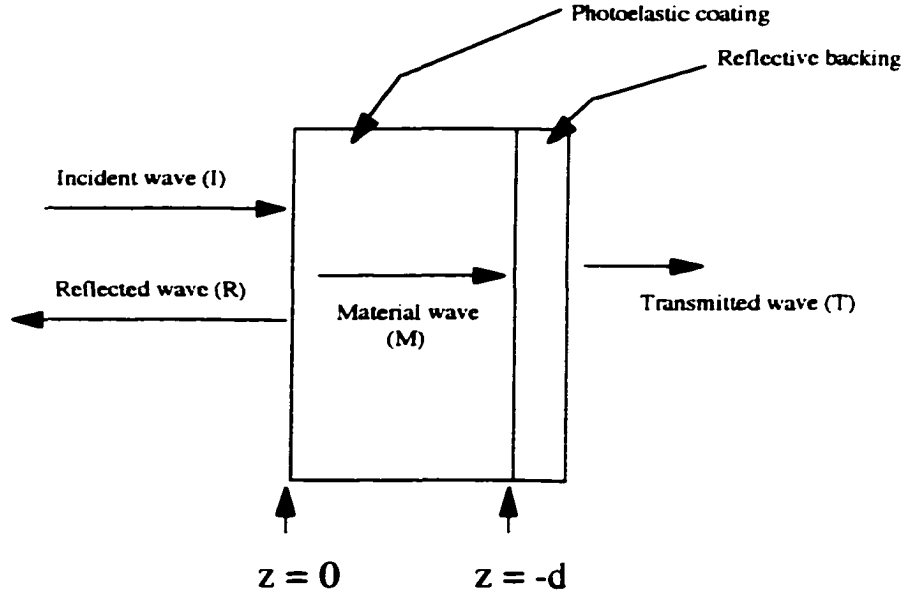


Figure 4.2. Propagating waves associated with the isoclinic and isochromatic theoretical models.

$$\begin{pmatrix} E_I^x \\ E_I^y \\ E_I^z \end{pmatrix} = \begin{pmatrix} \cos \theta & \sin \theta & 0 \\ -\sin \theta & \cos \theta & 0 \\ 0 & 0 & 1 \end{pmatrix} \begin{pmatrix} A \cos \phi \\ A \sin \phi \\ 0 \end{pmatrix} e^{-ik_0 z}. \quad (4.6)$$

In the vicinity of the material, there will be an incident (*I*), reflected (*R*), material propagating (*M*), and transmitted (*T*) waves as shown in Figure 4.2.

These have the form, in the material system,

$$\vec{E}_I' = [\hat{x}' \cos(\theta - \phi) + \hat{y}' \sin(\theta - \phi)] A e^{-ik_0 z} \quad (4.7a)$$

$$\vec{E}_R' = [\hat{x}' B_{x'} + \hat{y}' B_{y'}] e^{ik_0 z} \quad (4.7b)$$

$$\begin{aligned} \vec{E}_M' = & \hat{x}' \kappa_{xx} D_o e^{-\frac{i\omega z}{\sqrt{\nu\kappa_{xx}}}} + \hat{y}' \kappa_{yy} D_e e^{-\frac{i\omega z}{\sqrt{\nu\kappa_{yy}}}} + \\ & \hat{x}' \kappa_{xx} D_o' e^{\frac{i\omega z}{\sqrt{\nu\kappa_{xx}}}} + \hat{y}' \kappa_{yy} D_e' e^{\frac{i\omega z}{\sqrt{\nu\kappa_{yy}}}} \end{aligned} \quad (4.7c)$$

$$\vec{E}_T' = [\hat{x}' F_{x'} + \hat{y}' F_{y'}] e^{-ik_t z} \quad (4.7d)$$

By requiring the normal and tangential components of **B**, **D**, **E**, and **H** to be continuous across the boundaries,

$$\vec{n} \cdot (\vec{B}_2 - \vec{B}_1) = 0 \quad \vec{n} \times (\vec{E}_2 - \vec{E}_1) = 0 \quad (4.8)$$

$$\vec{n} \cdot (\vec{D}_2 - \vec{D}_1) = 0 \quad \vec{n} \times (\vec{H}_2 - \vec{H}_1) = 0,$$

four equations are generated at the air/photoelastic coating intersection,

$$E_I^x(z=0) + E_R^x(z=0) = E_M^x(z=0) \quad (4.9a)$$

$$E_I^y(z=0) + E_R^y(z=0) = E_M^y(z=0) \quad (4.9b)$$

$$H_I^x(z=0) + H_R^x(z=0) = H_M^x(z=0) \quad (4.9c)$$

$$H_I^y(z=0) + H_R^y(z=0) = H_M^y(z=0), \quad (4.9d)$$

and four at the photoelastic coating/reflective backing boundary

$$E_M^x(z=-d) = E_T^x(z=-d) \quad (4.10a)$$

$$E_M^y(z=-d) = E_T^y(z=-d) \quad (4.10b)$$

$$H_M^x(z=-d) = H_T^x(z=-d) \quad (4.10c)$$

$$H_M^y(z=-d) = H_T^y(z=-d). \quad (4.10d)$$

If the reflective backing was a perfect conductor, $\vec{E}_T' = 0$. The material wave would then be reflected upon interaction with the back surface ($z = -d$) reducing the number of equations in (4.10) to two (a-b). The remaining six equations are solved for the six unknown amplitudes, B_x , B_y , D_o , D_e , D_o' , and D_e' . For the case where the reflective backing has a finite conductivity whereby $\vec{E}_T' \neq 0$, it will be assumed that the energy transfer from the material wave to the transmitted wave is small so that the perfect conductor calculation is a close approximation. With this in mind, the amplitude and

phase of each wave can be calculated from the six equations (4.9a-d) and (4.10a-b). The polariscope records the backscatter from the sample therefore requiring the calculation of $B_{x'}$ and $B_{y'}$,

$$B_{x'} = \frac{A \cos(\theta - \phi) \left[\cos\left(\frac{\omega d}{\sqrt{\nu\kappa_{xx}}}\right) + \left(\frac{\omega}{k_o \sqrt{\nu\kappa_{xx}}}\right) \left(i \sin\left(\frac{\omega d}{\sqrt{\nu\kappa_{xx}}}\right)\right) \right]}{\cos\left(\frac{\omega d}{\sqrt{\nu\kappa_{xx}}}\right) - \left(\frac{\omega}{k_o \sqrt{\nu\kappa_{xx}}}\right) \left(i \sin\left(\frac{\omega d}{\sqrt{\nu\kappa_{xx}}}\right)\right)} \quad (4.11a)$$

$$B_{y'} = \frac{-A \sin(\theta - \phi) \left[\cos\left(\frac{\omega d}{\sqrt{\nu\kappa_{yy}}}\right) + \left(\frac{\omega}{k_o \sqrt{\nu\kappa_{yy}}}\right) \left(i \sin\left(\frac{\omega d}{\sqrt{\nu\kappa_{yy}}}\right)\right) \right]}{\cos\left(\frac{\omega d}{\sqrt{\nu\kappa_{yy}}}\right) - \left(\frac{\omega}{k_o \sqrt{\nu\kappa_{yy}}}\right) \left(i \sin\left(\frac{\omega d}{\sqrt{\nu\kappa_{yy}}}\right)\right)} \quad (4.11b)$$

Rewriting these equations in terms of a phase and amplitude results in the expression for the reflected wave

$$\vec{E}'_R = [\hat{x}' \cos(\theta - \phi) e^{i\Gamma_e} + \hat{y}' \sin(\theta - \phi) e^{i\Gamma_o}] A e^{ik_0 z} \quad (4.12)$$

where

$$\Gamma_e = \arctan \left[\frac{n_e \sin 2K_1 d}{\cos^2 K_1 d - n_e^2 \sin^2 K_1 d} \right] \quad (4.13a)$$

$$\Gamma_o = \arctan \left[\frac{n_o \sin 2K_2 d}{\cos^2 dK_2 - n_o^2 \sin^2 dK_2} \right] \quad (4.13b)$$

and

$$K_1 = \frac{\omega}{\sqrt{\nu\kappa_{xx}}} \quad (4.14a)$$

$$K_2 = \frac{\omega}{\sqrt{\nu\kappa_{yy}}} \quad (4.14b)$$

$$n_e = \frac{K_1}{k_0} \quad (4.14c)$$

$$n_o = \frac{K_2}{k_0} \quad (4.14d)$$

Inspection of equation (4.12) shows an ordinary wave traveling along the y' axis and an extraordinary wave along the x' axis, which is consistent with the behavior of an

anisotropic material. The reflected wave in (4.12) is rotated back to the lab system

$$\begin{pmatrix} E_I^x \\ E_I^y \\ E_I^z \end{pmatrix} = \begin{pmatrix} \cos \theta & -\sin \theta & 0 \\ \sin \theta & \cos \theta & 0 \\ 0 & 0 & 1 \end{pmatrix} \begin{pmatrix} \cos(\theta - \phi) e^{i\Gamma_e} \\ \sin(\theta - \phi) e^{i\Gamma_o} \\ 0 \end{pmatrix} A e^{-ik_0 z} \quad (4.15)$$

resulting in the expression

$$\begin{aligned} \vec{E}_R = & \hat{x} A e^{ik_0 z} [\cos \theta \cos(\phi - \theta) e^{i\Gamma_e} - \sin \theta \sin(\phi - \theta) e^{i\Gamma_o}] + \\ & \hat{y} A e^{ik_0 z} [\sin \theta \cos(\phi - \theta) e^{i\Gamma_e} - \cos \theta \sin(\phi - \theta) e^{i\Gamma_o}]. \end{aligned} \quad (4.16)$$

The reflected wave now passes through the analyzer which only transmits that portion of \vec{E}_R that is parallel to its polarization axis. This is written as

$$\vec{E}_{analyzer} = \hat{x} E_R^x \cos(\phi - 90^\circ) + \hat{y} E_R^y \sin(\phi - 90^\circ) \quad (4.17)$$

where the 90° signifies crossed polarizer and analyzer.

Comparison between theoretical and experimental results can only be done by converting this equation to an intensity value. This is accomplished by using

$$I = \langle E_x^2 \rangle + \langle E_y^2 \rangle + 2 \langle E_x \cdot E_y \rangle \cos(\delta) \quad (4.18)$$

where δ is the phase difference between the two waves. Combining equation (4.17) and (4.18) results in the linear polarization intensity equation

$$\begin{aligned} I_{linear} = & A_e^2 (\cos^2 \theta \sin^2 \phi + \sin^2 \theta \cos^2 \phi) + \\ & A_o^2 (\sin^2 \theta \sin^2 \phi + \cos^2 \theta \cos^2 \phi) + \\ & A_e A_o \sin 2\theta \cos 2\phi \cos(\Gamma_e - \Gamma_o) \end{aligned} \quad (4.19)$$

where

$$A_e = A \cos(\phi - \theta) \quad (4.20)$$

$$A_o = A \sin (\phi - \theta) .$$

Using the trigonometric identity $\cos 2\delta = 1 - 2 \sin^2 \delta$, equation (4.19) can be written as

$$\begin{aligned} I_{linear} = & A_e^2 (\cos^2 \theta \sin^2 \phi + \sin^2 \theta \cos^2 \phi) + \\ & A_o^2 (\sin^2 \theta \sin^2 \phi + \cos^2 \theta \cos^2 \phi) + \\ & A_e A_o \sin 2\theta \cos 2\phi - 2A_e A_o \sin 2\theta \cos 2\phi \sin^2 \left(\frac{\Gamma_e - \Gamma_o}{2} \right) . \end{aligned} \quad (4.21)$$

Numerical evaluation of this equation shows that the fourth term dominates the expression. This occurs because the observed fringes are a product of the phase difference between the extraordinary and ordinary waves. The contribution from the amplitude terms alone is extremely small. This simplification creates a modified linear intensity equation

$$I_{linear} = A^2 \sin [2 (\theta - \phi)] \sin 2\theta \cos 2\phi \sin^2 \left(\frac{\Gamma_e - \Gamma_o}{2} \right) . \quad (4.22)$$

With the amplitude squared defined as

$$a^2 = A^2 \sin 2\theta \cos 2\phi, \quad (4.23)$$

equation (4.22) can be rewritten as

$$I_{linear} = a^2 \sin [2 (\theta - \phi)] \sin^2 \left(\frac{\Gamma_e - \Gamma_o}{2} \right) . \quad (4.24)$$

Comparison of this equation with the linear intensity equation (3.4) from the one-dimensional theory,

$$I = a^2 \sin^2 [2 (\beta - \alpha)] \sin^2 \left(\frac{\pi \delta}{\lambda} \right) ,$$

shows remarkable similarities. The advantage of (4.24) over (3.4) is the detailed information contained in the anisotropic electromagnetic boundary intensity equation that is not explicitly involved in the one-dimensional theory. For any case where the stresses are known because the impermeability tensor links the stresses with the phase of

the waves, equation (4.24) can be used to simulate the photoelastic fringes. An added feature of equation (4.24) is its ability to include problems with optical components and reflective backings, such as imperfect polarizers and rough surfaces, and observe their influence on the resulting fringe patterns. Incorporating errors into the model in a systematic method and observing any changes in the photoelastic fringes will enhance our understanding of fringe generation by an applied stress and enable us to take the necessary steps to correct these problems.

4.2 Isochromatic Model

Isoclinic fringes are one of two fringe patterns produced using photoelasticity. The isoclinic fringes are used to extract the direction of the principal stresses whereas the isochromatic fringes provide the difference between the principal stresses. Isochromatic fringes are observed when linear polarized light is replaced with circular light. The mathematical development is similar to that of the isoclinics except with the addition of two quarter-wave plates, one following the polarizer and the other proceeding the analyzer as shown in Figure 4.3.

Isochromatic fringes are not dependent on the orientation of the polarizer/analyzer unit making the mathematical equations independent of ϕ . The incident polarized light will have the form

$$\vec{E}_I = \hat{y} A_y e^{-ik_0 z}. \quad (4.25)$$

This wave is incident on the first quarter-wave plate with its fast axis $\frac{\pi}{4}$ radians from the x axis. Transmission of this wave through the quarter-wave plate results in a $\frac{\pi}{4}$ rotation

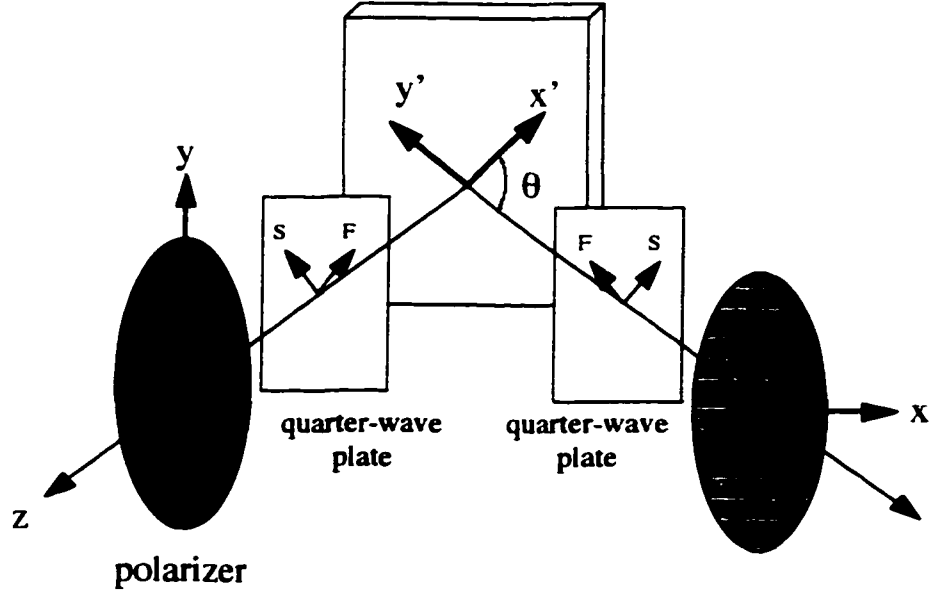


Figure 4.3. Set-up for the isochromatic model. The quarter-wave plates have a coordinate system that is rotated 45° from the lab system. The fast axis (F) denotes the component of the wave that will lead by a phase of 90° .

given by

$$\begin{pmatrix} E_{Q1}^x \\ E_{Q1}^y \end{pmatrix} = \begin{pmatrix} \cos \frac{\pi}{4} & \sin \frac{\pi}{4} \\ -\sin \frac{\pi}{4} & \cos \frac{\pi}{4} \end{pmatrix} \begin{pmatrix} 0 \\ A_y e^{-ik_0 z} \end{pmatrix} \quad (4.26)$$

yielding

$$\vec{E}_{Q1} = \hat{x}'_Q \left(\frac{\sqrt{2}}{2} \right) A_y e^{-(ik_0 z - \pi/2)} + \hat{y}'_Q \left(\frac{\sqrt{2}}{2} \right) A_y e^{-(ik_0 z)} \quad (4.27)$$

which is the equation for circularly polarized light. The unit axes \hat{x}'_Q and \hat{y}'_Q refer to the quarter-wave plate so as not to be confused with the primed material coordinate systems (kDB).

The light wave defined by (4.27) is incident upon the birefringent material requiring a coordinate transformation to the material system,

$$\begin{pmatrix} E_{Q1}^{x'} \\ E_{Q1}^{y'} \end{pmatrix} = \begin{pmatrix} \cos \left(\theta - \frac{\pi}{4} \right) & \sin \left(\theta - \frac{\pi}{4} \right) \\ -\sin \left(\theta - \frac{\pi}{4} \right) & \cos \left(\theta - \frac{\pi}{4} \right) \end{pmatrix} \begin{pmatrix} E_{Q1}^x \\ E_{Q1}^y \end{pmatrix} \quad (4.28)$$

where $(\theta - \frac{\pi}{4})$ is the angle between the fast axis of the quarter-wave plate and the x' axis as seen in Figure 4.4.

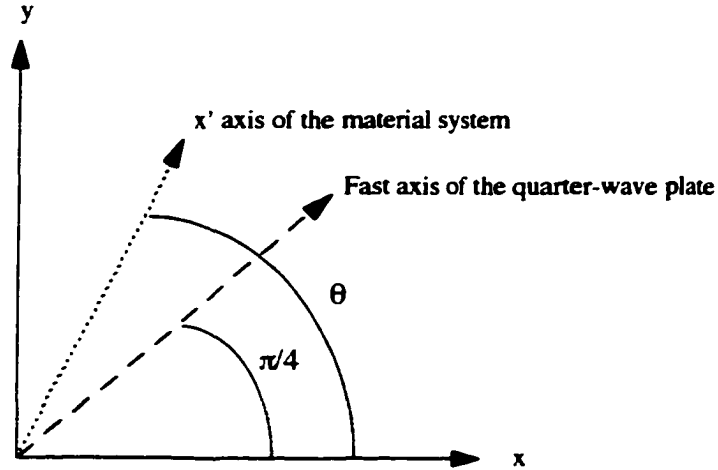


Figure 4.4. Relation between the quarter-wave plate axes and the material coordinate system.

This wave is used in place of \vec{E}_I' in equation (4.7a) to calculate the coefficients $B_{x'}$ and $B_{y'}$ resulting in

$$B_{x'} = \frac{\left(\frac{-A_y}{\sqrt{2}}\right) e^{i(\frac{\pi}{4}-\theta)} \left[(-1 + e^{i2\alpha_x}) k_o \kappa_{xx} + (1 + e^{i2\alpha_x}) \sqrt{\frac{\kappa_{xx}}{\nu}} \omega\right]}{(-1 + e^{i2\alpha_x}) k_o \kappa_{xx} - (1 + e^{i2\alpha_x}) \sqrt{\frac{\kappa_{xx}}{\nu}} \omega} \quad (4.29a)$$

$$\alpha_x = \frac{\omega d}{\sqrt{\nu \kappa_{xx}}} \quad (4.29b)$$

$$B_{y'} = \frac{\left(\frac{A_y}{\sqrt{2}}\right) e^{i(\frac{\pi}{4}-\theta)} \left[(-1 + e^{i2\alpha_y}) k_o \kappa_{yy} + (1 + e^{i2\alpha_y}) \sqrt{\frac{\kappa_{yy}}{\nu}} \omega\right]}{(-1 + e^{i2\alpha_y}) k_o \kappa_{yy} - (1 + e^{i2\alpha_y}) \sqrt{\frac{\kappa_{yy}}{\nu}} \omega} \quad (4.29c)$$

$$\alpha_y = \frac{\omega d}{\sqrt{\nu \kappa_{yy}}} \quad (4.29d)$$

Rewriting these equations in terms of phase and amplitude yields the reflected wave equation

$$\vec{E}_R' = \left(\hat{x}' A_{Bx} e^{i\Lambda_x} e^{-i\pi/2} + \hat{y}' A_{By} e^{i\Lambda_o}\right) e^{ik_o z} \quad (4.30)$$

where

$$A_{Bx} = \frac{\left(\frac{A_y}{\sqrt{2}}\right) [(1 + n_e^2) + (-1 + n_e^2) \cos(2K_1d)]}{\sin^2(K_1d) + n_e^2 \cos^2(K_1d)} \quad (4.31a)$$

$$\Lambda_e = \tan^{-1} \left[\frac{\varrho_e \sin\left(\frac{\pi}{4} - \theta\right) + n_e \sin(2K_1d) \cos\left(\frac{\pi}{4} - \theta\right)}{\varrho_e \cos\left(\frac{\pi}{4} - \theta\right) - n_e \sin(2K_1d) \sin\left(\frac{\pi}{4} - \theta\right)} \right] \quad (4.31b)$$

$$\varrho_e = n_e^2 \cos^2(K_1d) - \sin^2(K_1d) \quad (4.31c)$$

$$A_{By} = \frac{\left(\frac{A_y}{\sqrt{2}}\right) [(1 + n_o^2) + (-1 + n_o^2) \cos(2K_2d)]}{\sin^2(K_2d) + n_o^2 \cos^2(K_2d)} \quad (4.31d)$$

$$\Lambda_o = \tan^{-1} \left[\frac{\varrho_o \sin\left(\frac{\pi}{4} - \theta\right) + n_o \sin(2K_2d) \cos\left(\frac{\pi}{4} - \theta\right)}{\varrho_o \cos\left(\frac{\pi}{4} - \theta\right) - n_o \sin(2K_2d) \sin\left(\frac{\pi}{4} - \theta\right)} \right] \quad (4.31e)$$

$$\varrho_o = n_o^2 \cos^2(K_2d) - \sin^2(K_2d). \quad (4.31f)$$

This wave now passes through the second quarter-wave plate with its fast and slow axes reversed from that of the first. This optical element rotates \vec{E}'_R about z from the material coordinate (kDB) system to the primed quarter-wave plate system by

$$\begin{pmatrix} E'_{Q2}{}^{x-slow} \\ E'_{Q2}{}^{y-fast} \end{pmatrix} = \begin{pmatrix} \cos\left(\theta - \frac{\pi}{4}\right) & -\sin\left(\theta - \frac{\pi}{4}\right) \\ \sin\left(\theta - \frac{\pi}{4}\right) & \cos\left(\theta - \frac{\pi}{4}\right) \end{pmatrix} \begin{pmatrix} E'_R{}^x \\ E'_R{}^y \end{pmatrix} \quad (4.32)$$

which results in the equation

$$\begin{aligned} \vec{E}'_{Q2} &= \hat{x}'_Q \left[A_{Bx} \cos\left(\theta - \frac{\pi}{4}\right) e^{i\Lambda_e} e^{i(k_oz - \pi/2)} - A_{By} \sin\left(\theta - \frac{\pi}{4}\right) e^{i\Lambda_o} e^{ik_oz} \right] \\ &+ \hat{y}'_Q \left[A_{Bx} \sin\left(\theta - \frac{\pi}{4}\right) e^{i\Lambda_e} e^{i(k_oz - \pi)} + A_{By} \cos\left(\theta - \frac{\pi}{4}\right) e^{i\Lambda_o} e^{i(k_oz - \pi/2)} \right]. \end{aligned} \quad (4.33)$$

This wave is rotated $\frac{\pi}{4}$ radians about z and is finally incident upon the analyzer with its polarization axis along x . Taking the x components of \vec{E}'_{Q2} yields

$$\vec{E}_{analyzer} = \hat{x} \left(\frac{\sqrt{2}}{2} \right) (E_{Q2}^{x'} - E_{Q2}^{y'}) . \quad (4.34)$$

Using the relation $I = EE^*$ results in the intensity equation for circular polarization

$$I_{circular} = \frac{1}{2} (A_{Bx} - A_{By})^2 + 2A_{Bx}A_{By} \sin^2 \left(\frac{\Lambda_e - \Lambda_o}{2} \right) . \quad (4.35)$$

Numerical analysis of this equation shows

$$\frac{1}{2} (A_{Bx} - A_{By})^2 \ll 2A_{Bx}A_{By} \sin^2 \left(\frac{\Lambda_e - \Lambda_o}{2} \right) \quad (4.36)$$

which, for the same reasons as the isoclinic case, simplifies the circular polarization intensity to

$$I_{circular} = 2A_{Bx}A_{By} \sin^2 \left(\frac{\Lambda_e - \Lambda_o}{2} \right) . \quad (4.37)$$

With $a^2 = 2A_{Bx}A_{By}$ in the above equation, $I_{circular}$ resembles the circular polarization intensity of one-dimensional theory, equation (3.5),

$$I = a^2 \sin^2 \left(\frac{\pi \delta}{\lambda} \right) .$$

As with the isoclinic model, the advantage of equation (4.37) over equation (3.5) is the detailed information regarding the propagating waves which form the observed fringe patterns.

4.3 Experimental Versus Theoretical Comparison

Theoretical photoelastic fringes are produced by incorporating equations (4.24) and (4.37) into a computer program to create intensity contour plots. The code was written in Mathematica and used the stresses over the surface of the object calculated from known equations or finite element. A common benchmark object for stress

analysis is a plate with a central, circular hole under uniaxial tension. Equations describing the stress field for an infinite plate with a central, circular hole can be obtained from various continuum mechanics books and used to generate files of T_x , T_y , and T_{xy} calculated at each coordinate location. These files are read into the Mathematica model and the stress matrix associated with each coordinate is converted to a diagonal matrix (principal stress matrix) through

$$\begin{aligned} T_{x'} &= \frac{1}{2}(T_x + T_y) + \frac{1}{2}(T_x - T_y)\cos 2\theta + T_{xy}\sin 2\theta \\ T_{y'} &= \frac{1}{2}(T_x + T_y) - \frac{1}{2}(T_x - T_y)\cos 2\theta - T_{xy}\sin 2\theta \\ \tan 2\theta &= \frac{2T_{xy}}{T_x - T_y} \end{aligned} \quad (4.38a)$$

where θ is the principal angle [118]. The stress dependent variables in the theoretical model are κ_{xx} and κ_{yy} which are used in the calculation of the phase velocities for the ordinary and extraordinary waves. With the impermeability tensor, \mathfrak{p} , related to the impermeability tensor, κ , by $\mathfrak{p} = \epsilon_o \kappa$, the first two components in equation (4.3) can be written as

$$\kappa_{xx} = \frac{1}{\epsilon_o n^2} + \frac{1}{\epsilon_o} (q_{xx} T_{x'} + q_{xy} T_{y'}) \quad (4.39a)$$

$$\kappa_{yy} = \frac{1}{\epsilon_o n^2} + \frac{1}{\epsilon_o} (q_{xy} T_{x'} + q_{yy} T_{y'}) \quad (4.39b)$$

where q 's are the stress optic coefficients and $1/n^2 = 1/\epsilon^{(0)}$. The strain optic coefficients are tabulated for selected materials and are converted to stress optic coefficients through equation (3.12). The impermeability components are calculated at each coordinate location and used to calculate the intensity in equations (4.24) and (4.37) after the selection of the material thickness and wavelength of light used in the

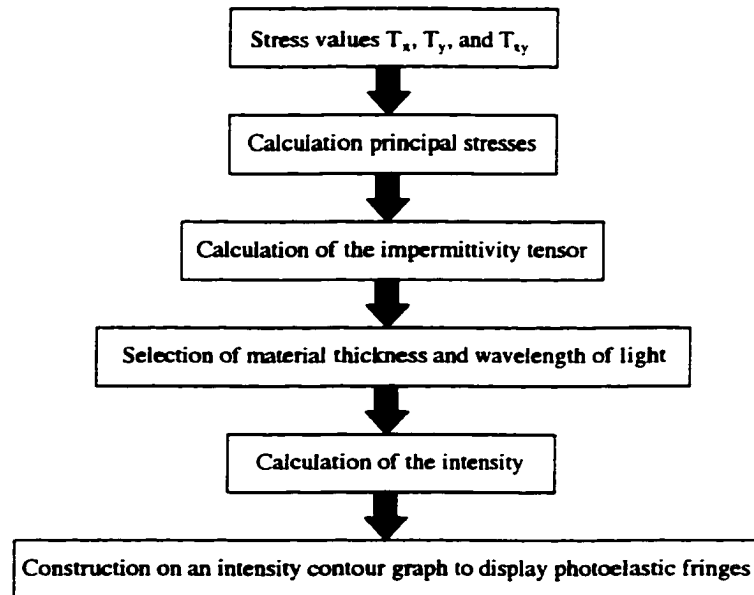
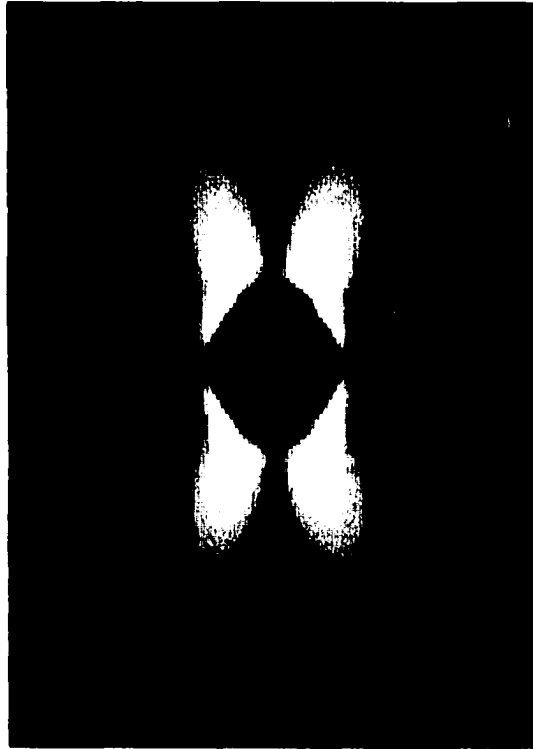


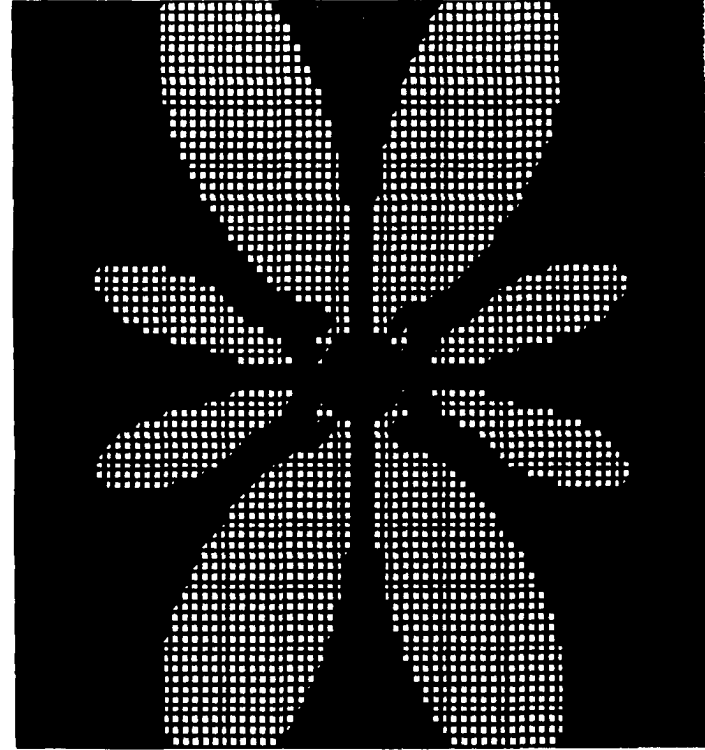
Figure 4.5. Flow chart for the theoretical calculation of the photoelastic fringes.

initial illumination. See Figure 4.5 for a flow diagram of the code. The resulting graph is a surface plot which is then converted to a contour image. Mathematica does not easily permit the manipulation of these images, so the intensity information was written to a file and analyzed by Microsoft Excel. This spread sheet permitted the adjustment of the plotted intensity scale so that various slices of the surface plot could be examined and compared with experimental results. The result of the classical Kirsch problem solution for a hole in an infinite plate under uniaxial tension is shown in Figure 4.6a and is consistent with expected laboratory results.

To obtain the stresses for any object under a myriad of loading conditions, a finite element analysis package was used. COSMOS/M, a commercial finite element package, was used to build a model of finite dimension and select material makeup. The model was subjected to uniaxial tension resulting in contour image plots for T_x , T_y , and T_{xy} as shown in Figure 4.7. Because COSMOS/M only provided stress information



(a)



(b)

Figure 4.6. Comparison of (a) experimental versus (b) theoretical photoelastic fringe pattern for a hole in plate under vertical tension. The experimental image was obtained with the model 030-polariscope and the theoretical image was calculated from the Kirsch problem.

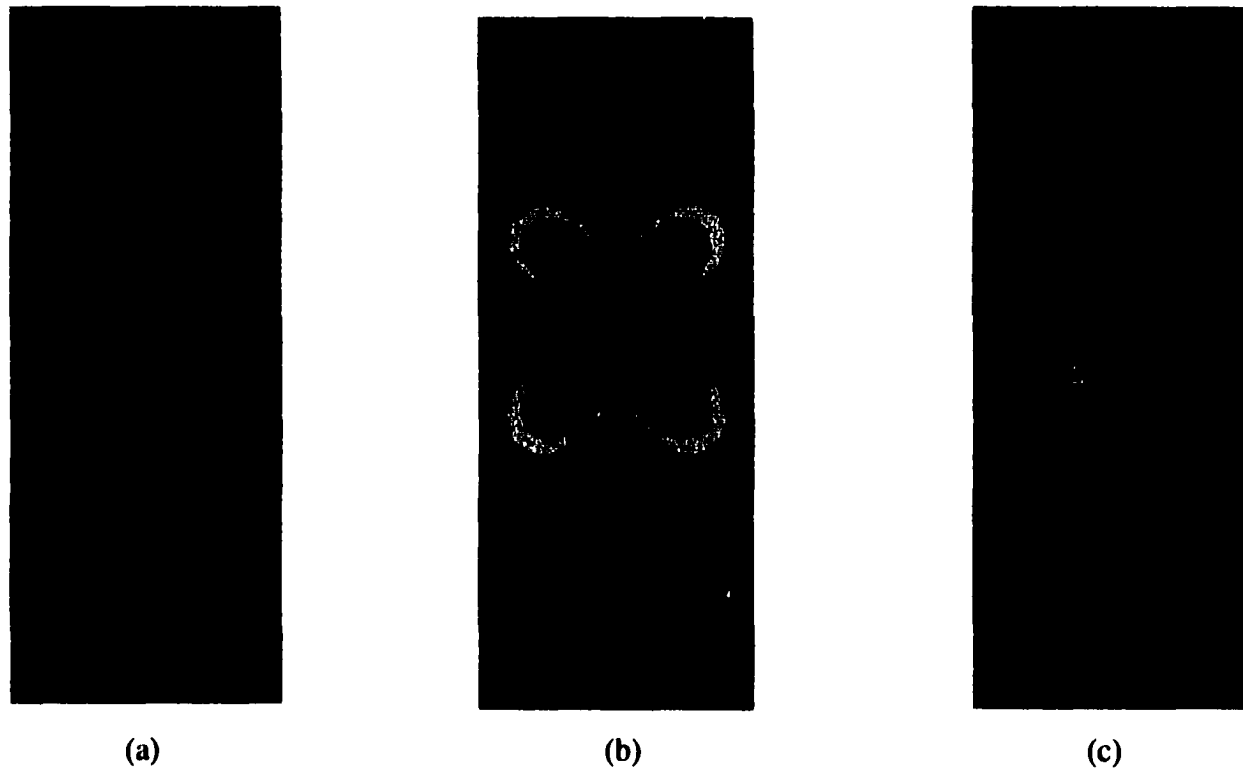
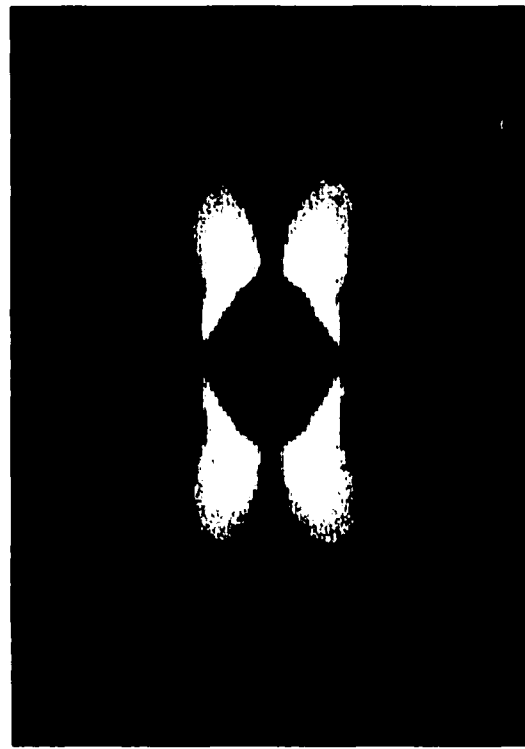


Figure 4.7. A typical stress contour images for a FEA model of a hole in plate under uniaxial tension: (a) T_x , (b) T_y , (c) T_{xy} . A color legend would accompany each image for the conversion of color to stress level.

at nodal points, the contour plots (an interpolation graphic from the calculated nodal stresses) were downloaded into NIH-Image 1.57. This program permitted regions of the stress contour image to be saved as text with the pixel locations possessing a value ranging from 1 to 255 corresponding to the color at that point. The color was converted to stress through the color scale provided by COSMOS/M with each contour stress image. Adjusting the existing code to accommodate the new stress information provided a method to check the model against objects. The results for a hole in a finite plate under uniaxial tension is shown in Figure 4.8. A slightly more complicated geometry is a notched hole is illustrated Figure 4.9. Notice that both contain a dark fringe line extending from the notch towards the top and bottom of the hole. A plate with two identical offset holes, seen in Figure 4.10, and two different, offset holes in Figure 4.11. Both theoretical images are qualitatively similar to the laboratory results. These geometries suggest that the electromagnetic boundary value problem will produce isoclinic photoelastic fringes for many geometries if given the stress field.

The other set of photoelastic fringes, the isochromatics, proved to be more difficult to match with experimental images. This occurred because the fringe patterns are dependent upon the applied stress. As the stress changes, so do the isochromatics. This problem was not encountered in the isoclinic model because these images are load independent. Isoclinic fringes measure the direction of the principal stresses which do not change with increasing loads whereas the isochromatics measure the difference in magnitude between the principal stresses. As the applied load increases, so does the magnitude. The comparison between an experimental image and the Kirsch problem is shown in Figure 4.12. Although the images are consistent, they are at different applied

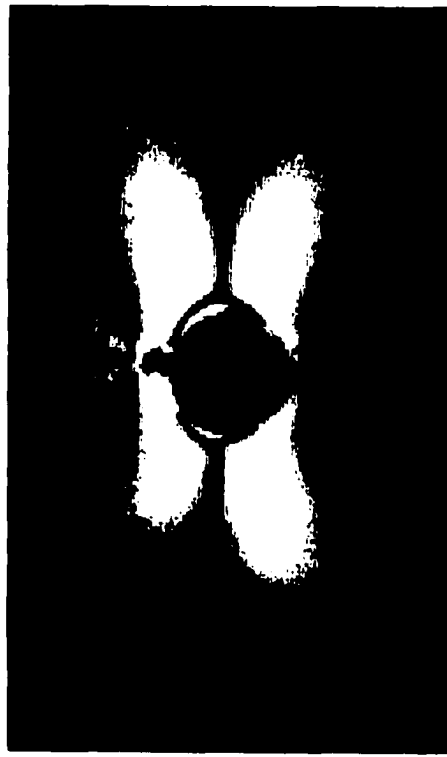


(a)

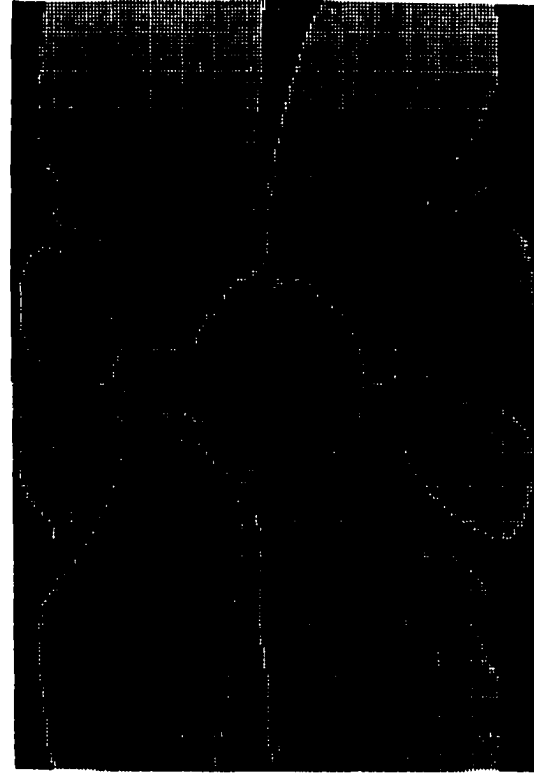


(b)

Figure 4.8. Comparison of (a) experimental versus (b) theoretical photoelastic fringe patterns for a hole in a PMMA plate under vertical tension. The theoretical image was calculated using Finite Element Analysis.

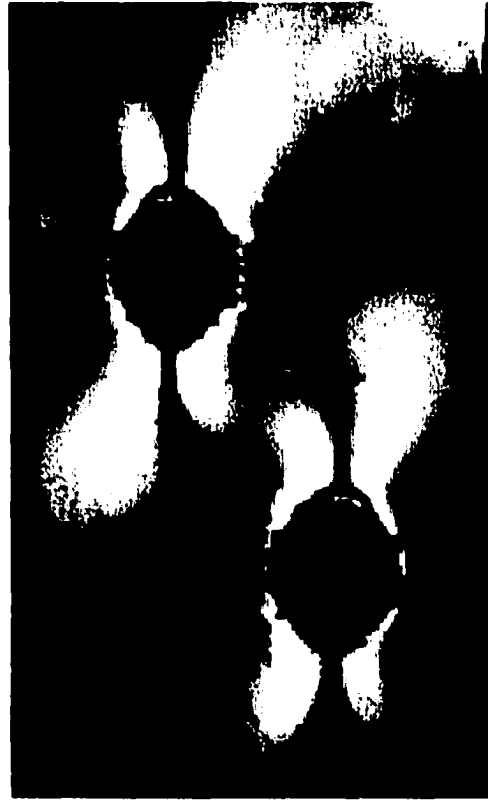


(a)



(b)

Figure 4.9. Comparison of (a) experimental versus (b) theoretical photoelastic fringe patterns for a hole with a notch in a PMMA plate under vertical tension. The theoretical image was calculated using Finite Element Analysis.



(a)



(b)

Figure 4.10. Comparison of (a) experimental versus (b) theoretical photoelastic fringe pattern two identical holes in a PMMA plate under vertical tension. The theoretical image was calculated using Finite Element Analysis. The experimental image (a) shows the reflection of the light source in the upper right corner.

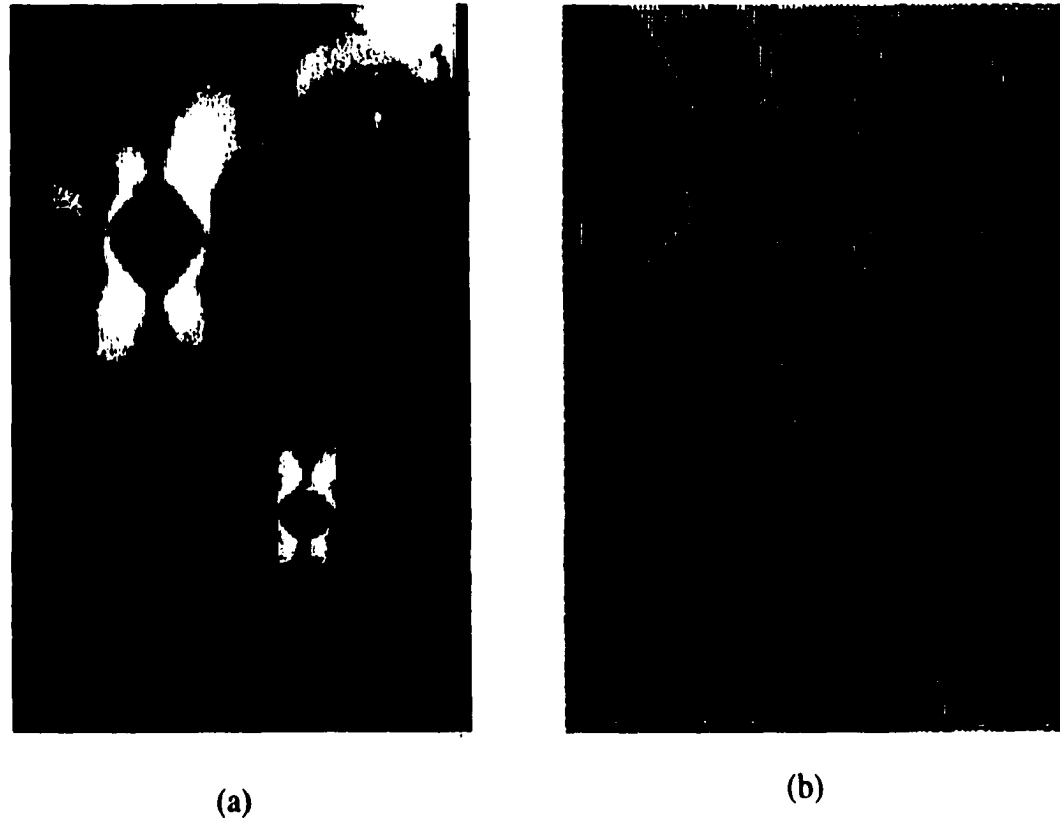
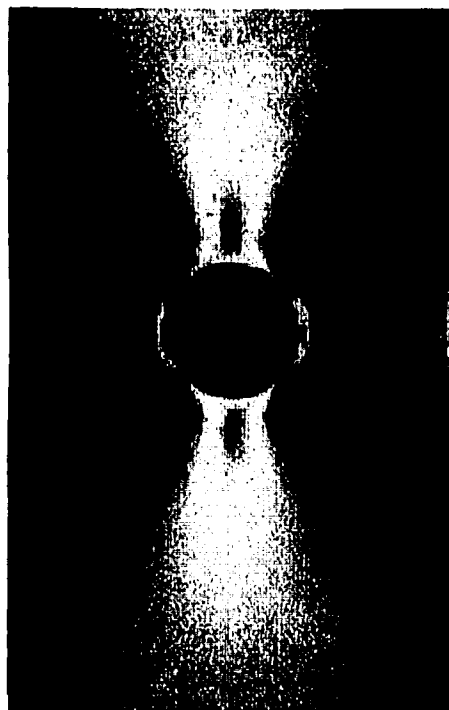
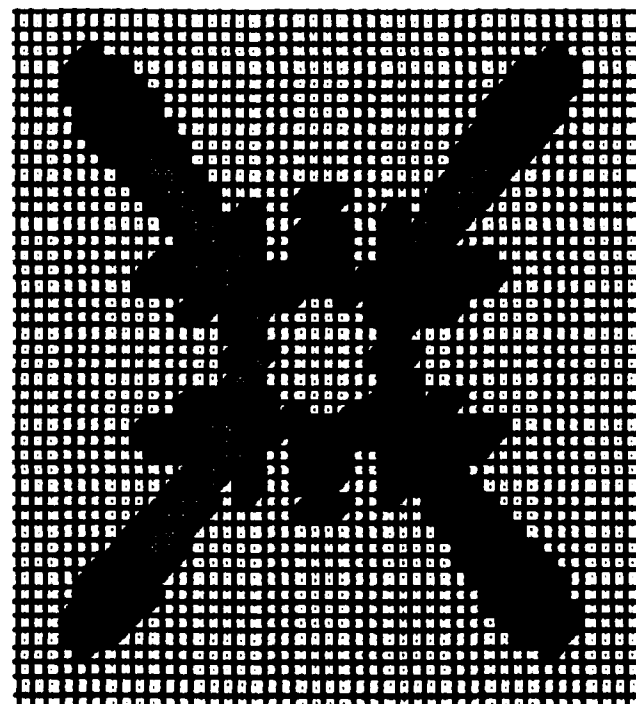


Figure 4.11. Comparison of (a) experimental versus (b) theoretical photoelastic fringe pattern two different sized holes in a PMMA plate under vertical tension. The theoretical image was calculated using Finite Element Analysis. The experimental image (a) shows the reflection of the light source in the upper right corner.



(a)



(b)

Figure 4.12. (a) Experimental versus (b) theoretical isochromatic fringes for a hole in a plate under uniaxial tension. The stresses for the theoretical images were calculated from the Kirsch problem.

loads. Figure 4.13 shows the comparison between a FEA image at an applied load of 400 pounds and an experimental image at the same loading. The FEA model is beginning to exhibit the characteristic pattern for that material at 400 pounds, but it is not a complete match. This was not entirely unexpected. Finite element analysis does not completely match the actual loading conditions and material properties because it is impossible to know precisely all of the conditions to which this object was exposed. The boundary conditions which the computer uses to calculate the stresses are only an approximation of the actual laboratory. The results of the model are as good as the input parameters, some of which have to be estimated. FEA is, at most, a good approximation but not an exact match to the laboratory conditions.

4.4 Combining Thermoelasticity and Photoelasticity

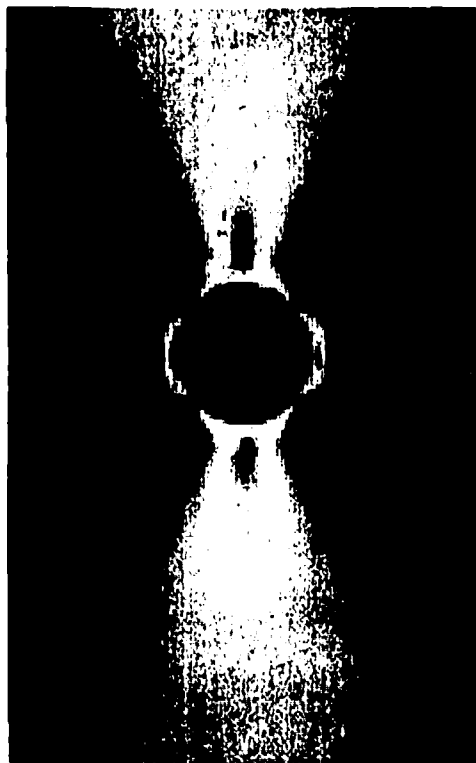
Thermoelasticity provides the sum of the principal stresses and photoelasticity provides the difference of the principal stresses plus the principal stress direction. Combining thermoelastic and photoelastic data to extract the full stress tensor is not computationally difficult. To determine the relation between the principal stresses and the full stress components, begin with a stress tensor of the form

$$\begin{pmatrix} T_x & T_{xy} \\ T_{xy} & T_y \end{pmatrix}. \quad (4.40)$$

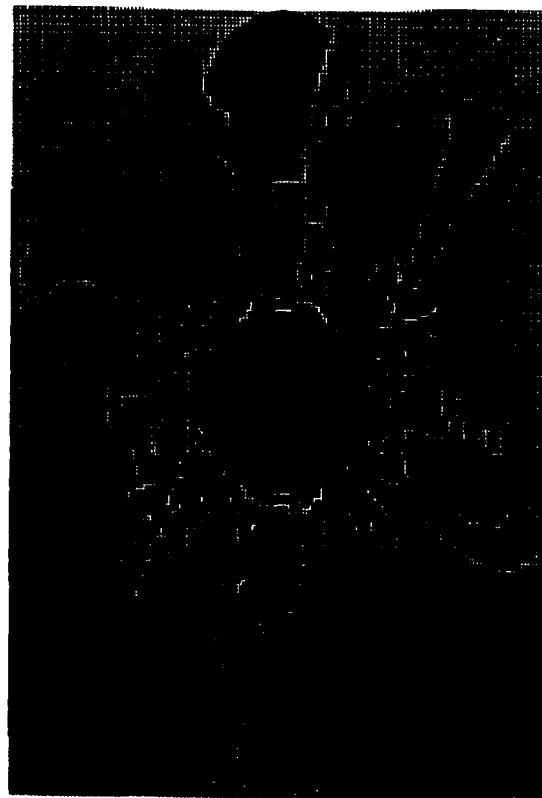
A rotation of this matrix about an angle θ yields a tensor with its components defined in terms of the original matrix elements [118]

$$T_{x'} = \frac{1}{2}(T_x + T_y) + \frac{1}{2}(T_x - T_y)\cos 2\theta + T_{xy}\sin 2\theta \quad (4.41a)$$

$$T_{y'} = \frac{1}{2}(T_x + T_y) - \frac{1}{2}(T_x - T_y)\cos 2\theta - T_{xy}\sin 2\theta \quad (4.41b)$$



(a)



(b)

Figure 4.13. (a) Experimental versus (b) theoretical isochromatic fringes for a hole in a plate under uniaxial tension at 400 pounds. The stresses for the theoretical images were calculated using FEA.

$$T_{x'y'} = -\frac{1}{2} (T_x - T_y) \sin 2\theta + T_{xy} \cos 2\theta. \quad (4.41c)$$

This rotated matrix becomes the principal matrix by requiring $T_{x'y'}$ to be zero. Solving for θ in (4.41c) and defining it as the principal angle results in

$$\tan 2\theta = \frac{2T_{xy}}{T_x - T_y}. \quad (4.42)$$

Solving (4.41a) and (4.41b) for T_x and T_y produces the relations between the general stress and the principal stress components

$$T_x = \frac{1}{2} [(T_{x'} + T_{y'}) + (T_{x'} - T_{y'}) \cos 2\theta] \quad (4.43a)$$

$$T_y = \frac{1}{2} [(T_{x'} + T_{y'}) - (T_{x'} - T_{y'}) \cos 2\theta] \quad (4.43b)$$

$$T_{xy} = \frac{1}{2} (T_{x'} - T_{y'}) \sin 2\theta \quad (4.43c)$$

where $(T_{x'} + T_{y'})$ is provided by the thermoelastic system and $(T_{x'} - T_{y'})$ and θ came from the photoelastic system. Using these equations, it is possible to determine the components of the stress tensor over the surface of the object if the sum and difference of the principal stresses are known along with the principal angle at each point on the surface. The difficulty with determining the tensor elements at each pixel lies not with material compatibility between the thermoelastic and photoelastic systems but with experimental and processing issues such as load setting, calibration errors, and pixel matching.

4.5 Data Integration Issues

Since thermoelastic measurements are steady-state and photoelastic measurements are static, a common loading between the two systems is needed for the integration of the two data sets. K. E. Cramer *et. al* compared thermoelastic data with data

generated from finite element code using a static load. They studied the tensile and compressive stresses across a hole in a plate under vertical tension and concluded that the thermoelastic data matched the finite element results when the mean load from the thermoelastic measurement was used in the theoretical static model [119].

The steady-state loading for thermoelastic analysis produces errors in the calculated sum of the principal stresses at certain edges on a sample. The phase images for a hole in a plate and two holes in a plate under vertical tension are shown in Figure 4.14. The tops and bottoms of the holes reveal a different phase from that of the sample. This occurs because the vertical motion (deformation) of the sample due to cyclic loading makes the imager average data between free space and the sample. The imager locks into the phase exhibited by the majority of the sample and generates a two-dimension stress map. Variations in phase result in inaccuracies in the thermoelastic data. This effect can be minimized but not eliminated.

The stress maps produced by thermoelasticity and photoelasticity require calibration to ensure accurate stress values. Interpretation of these images in terms of sums and differences of principal stresses is done through a color legend or fringe-order-to-stress conversion. For thermoelastic analysis, a color legend bar accompanies every image and is calibrated with a perpendicular strain gauge rosette mounted to the object in an area with a low strain gradient. The strain gauge readings are used to determine the calibration factor, k ,

$$k = \frac{E(\epsilon_x + \epsilon_y)}{S_{ave}(1 - \nu)} \quad (4.44)$$

where E is Young's Modulus, ν is Poisson's ratio, ϵ_x and ϵ_y are the measurements from the strain gauge, and S_{ave} is the average thermoelastic signal obtained in the location

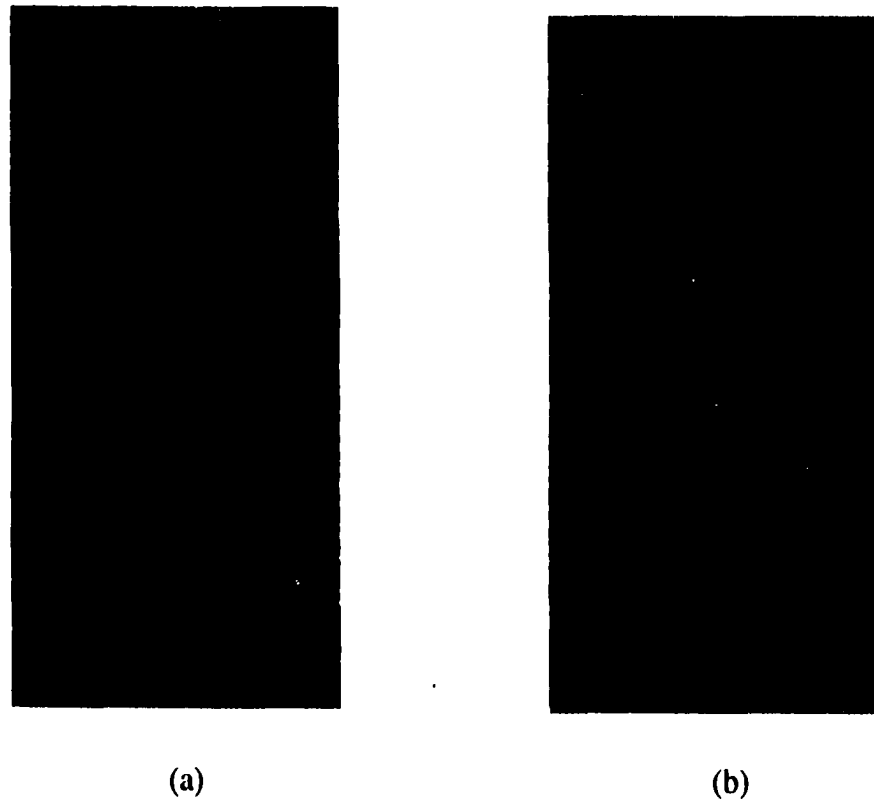


Figure 4.14. Thermoelastic phase images for a PMMA plate with (a) one hole and (b) two holes under vertical tension. The tops and bottoms of the holes exhibit a different phase from the rest of the sample due to cyclic loading.

of the strain gauge [120]. For circular polarized white light photoelasticity, colors are associated with stresses according to an unvarying sequence of color in the birefringent material. The relative retardation in the material extinguishes one color of the incident white light as the load is increased. Once a full wavelength of relative retardation is achieved, the colors repeat, appearing fainter than the first series signifying an increase by a whole fringe order. Each material will have its own unique color-to-stress conversion chart which can be determined using the deflection of a cantilever beam. With a beam coated with the photoelastic material and one end mounted in a rigid frame, a precision micrometer deflects the beam imposing a known state of strain on the coating which is then correlated with the resultant birefringence [121]. For circularly polarized monochromatic light, only dark and bright fringes are present. The difference of the principal stresses (or strains) is calculated by determining the fringe order, N . Refer to section 3.1, equation (3.3).

A second set of fringes is obtained when linear polarized light is used for illumination and the sample viewed with an analyzer having its polarization axes set perpendicular to the incident light. Black fringes appear in the material corresponding to the polarizer/analyzer axes becoming parallel to the direction of the principal stresses. As the polarizer/analyzer is rotated through 90° , the full set of isoclinic fringes are observed. These fringes are typically traced or photographed to produce an image with of all of the isoclinic angles as shown in Figure 4.15. From this composite image, isostatic lines are drawn, as shown in Figure 4.16, revealing stress trajectories which provide more insight into the stress field of the object under study. The isostatic lines are constructed in a similar manner to equipotential lines in electrostatics. The

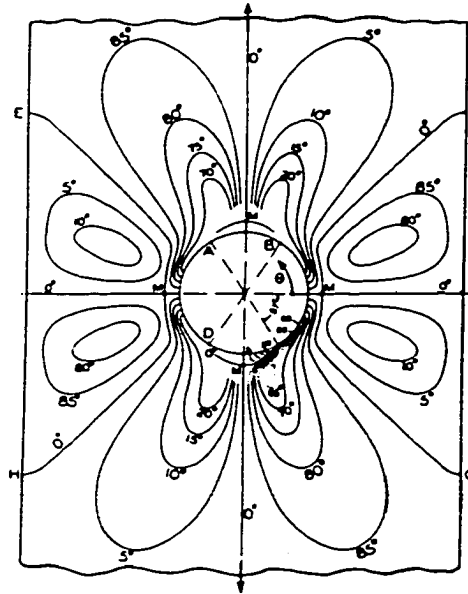


Figure 4.15. Isoclinic lines for a hole in a plate under vertical tension. The angles correspond to the rotation of the polarizer/analyzer about the z axis in the laboratory system [123].

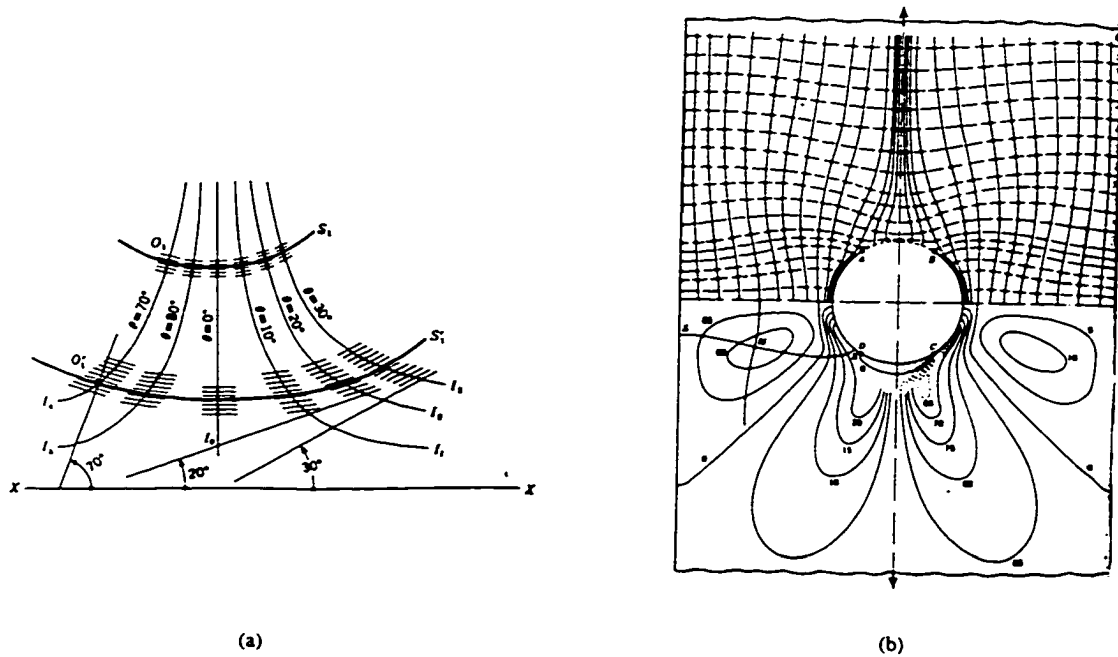


Figure 4.16. (a) General construction of isostatic lines from isoclinic lines used to visualize the (b) stress trajectories for a hole in plate under vertical tension. Stress trajectories are at the top if (b) and isoclinic lines at the bottom [123].

equipotential lines bisect the electric field lines whereas the isostatic lines are rotated an angle θ from the bisector in accordance with the isoclinic line it passes. At times, isoclinic fringes appear as broad bands rather than thin lines. Tracing methods position the isoclinic line through the center of the thick band. More recently, computer algorithms have been developed which digitize the isoclinic image and convert it to a fringe skeleton with a width of one pixel. These codes are hampered by long processing times and are prone to failure in areas of high stresses [122].

An increasingly popular technique for determining the isoclinic angle and phase difference between the ordinary and extraordinary waves (isochromatic parameter) is through the use of four fringe images obtained at different polarizer/analyzer settings. Each image is associated with an intensity equation, and algebraic manipulation of these equations results in the isoclinic angle being a function of the arctangent and the isochromatic parameter a function of the arccosine of the four intensities. Because of the inverse trigonometric functions, discontinuities in the returned values occur requiring an unwrapping process to restore continuity throughout the entire field. This is not a trivial process. For the isoclinic unwrapping, only points with at least one of its eight adjacent points unwrapped can be treated. This is done by adding or subtracting $\pi/2$ where the phase difference between points is more than $\pi/3$. Isochromatic unwrapping is different from the isoclinic procedure. The isochromatic parameter is unwrapped once the zero order fringe, the maximal and minimal values of the isochromatic parameter, and the total number of fringes are known [122].

For thermoelastic and photoelastic data to be combined, the stress images from the two systems must possess a one-to-one pixel mapping. The DeltaTherm 1000 has

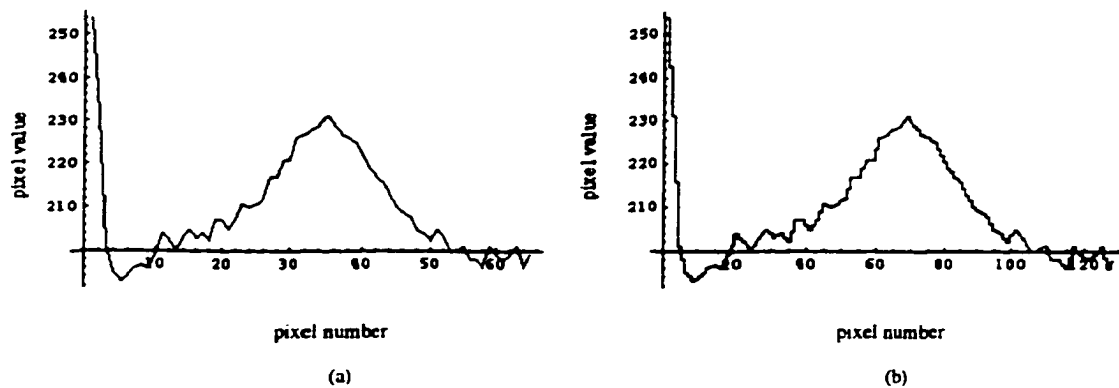


Figure 4.17. Sixty pixels of thermoelastic data expanded to 120 pixels by linear interpolation between every two points.

a picture resolution of 128 x 128 square pixels whereas the photoelastic images are acquired with a digital camera producing 800 x 600 or 1600 x 1200 square pixel images. Alignment of these images is critical in obtaining the components of the stress tensor. Barone and Patterson reduced the larger array of points to that of the smaller array through computer processing [103]. An alternative method is to expand the smaller data matrix to that of the larger. Since thermal data is typically smooth, the number of pixels can be increased through linear interpolation as shown in Figure 4.17. Algorithms for this process can be found in many image analysis software packages.

Another issue that has received less attention in the literature is the effect of a non-retroreflecting surface. It is assumed that the reflective backing is a perfect retroreflector which preserves the state of the wave upon reflection. Any change to the light wave, physically observed as fringes, is attributed solely to induced anisotropy of the photoelastic coating by the applied stress. If the reflective backing also contributed a change on the light wave upon reflection, what influence would it have to the observed fringe pattern? Additionally, what effect would it have on the determination of the full-field stress tensor?

Chapter 5

Depolarization of Electromagnetic Waves

Polarization refers to the orientation of the field vectors of an electromagnetic wave at a given point during one period of oscillation. A change in polarization as a consequence of propagation, reflection, scattering, diffraction, or any other interaction with matter is called depolarization. The case under consideration for this thesis is the depolarization effect of a light wave upon reflection from an imperfect retroreflector, such as a rough surface. A retroreflector is an optical element that reflects an incident beam of light back to its origin for all angles of incidence. This is an important feature because not only is the intensity of light at the analyzer greater but also the light ray returns along the same path it entered the coating thereby eliminating any stress gradient averaging. Any averaging is a result of the reflected light passing through a slightly larger area of the coating due to a change in angle of reflection from the angle of incidence. Because the stresses differ from point to point, the information extracted from the light at the analyzer is related to the average of the stress gradient in that area of inspection. Since photoelastic fringes are produced by the depolarization of the incident light wave by the induced anisotropy of the photoelastic medium, any additional depolarization by the reflective surface is unwanted and can change the fringe pattern. The mathematical model used to simulate the photoelastic fringes assumed a smooth, reflective surface exhibiting retroreflection. A smooth plane will reflect the

incident light spectrally in a single direction while a rough surface will scatter it into various directions. The same surface may be rough for some wavelengths and smooth for others; or for the same wavelength it may be either rough or smooth for different angles of incidence. The scattered waves are not only described by their amplitudes and phases, but also by their polarization. One of the difficult questions connected with rough-surface theory is what happens to the original polarization of the incident wave after it has been scattered.

5.1 The Rayleigh Criterion

The Rayleigh criterion, based on ray theory, is the most widely used approach to scattering by rough surfaces. Consider two rays incident on a surface with irregularities in height h at a grazing angle of γ . The path difference between these two rays is

$$\Delta r = 2h \sin \gamma \quad (5.1)$$

with a phase difference of

$$\Delta \phi = \frac{2\pi}{\lambda} \Delta r. \quad (5.2)$$

If the phase difference is small, the two rays will be almost in phase as in the case of a perfectly smooth surface. As the phase difference increases, the two rays will interfere until $\Delta \phi = \pi$ and will cancel. If there is no energy flow in this direction, it must have been redistributed in other directions. Thus for $\Delta \phi = \pi$ the surface scatters and is considered rough and for $\Delta \phi = 0$ the surface reflects spectrally and is smooth. The dividing line between a rough surface and a smooth surface is determined by choosing the phase difference between the extremes, $\Delta \phi = \frac{\pi}{2}$. Upon substitution into equation

(5.1), the equation for the Rayleigh Criterion is written as

$$h < \frac{\lambda}{8 \sin \gamma} \quad (5.3)$$

which determines whether a surface is considered smooth. An alternate method of expressing the Rayleigh Criterion is to use only the right side of this equation as a measure of the effective surface roughness. Therefore a surface will tend to be effectively smooth only under two conditions:

$$\frac{h}{\lambda} \rightarrow 0 \quad \text{or} \quad \gamma \rightarrow 0. \quad (5.4)$$

The Rayleigh criterion is useful for the distinction between smooth and rough surfaces because it is based on three easily measured parameters (h , λ , γ) but does not provide any details on the effect that rough surfaces have on scattered waves. The next section will discuss a more quantitative expression for the backscattered wave in terms of the same three parameters [124].

5.2 Optical Analysis of the Reflective Backings

The two reflective surfaces used in the laboratory were Rust-Oleum metallic paint and the Measurements Group polycarbonate sheet with reflective backing. Upon visual inspection, both looked relatively smooth. The surface of the metallic paint at a magnification of 40x is shown in Figure 5.1. The silver particles suspended in the paint are quite prominent and vary in size. Notice that some of the image is out of focus. This indicates the height differential that was present on the surface. A slight turn of the fine adjustment knob on the microscope brought these areas into focus. The surface

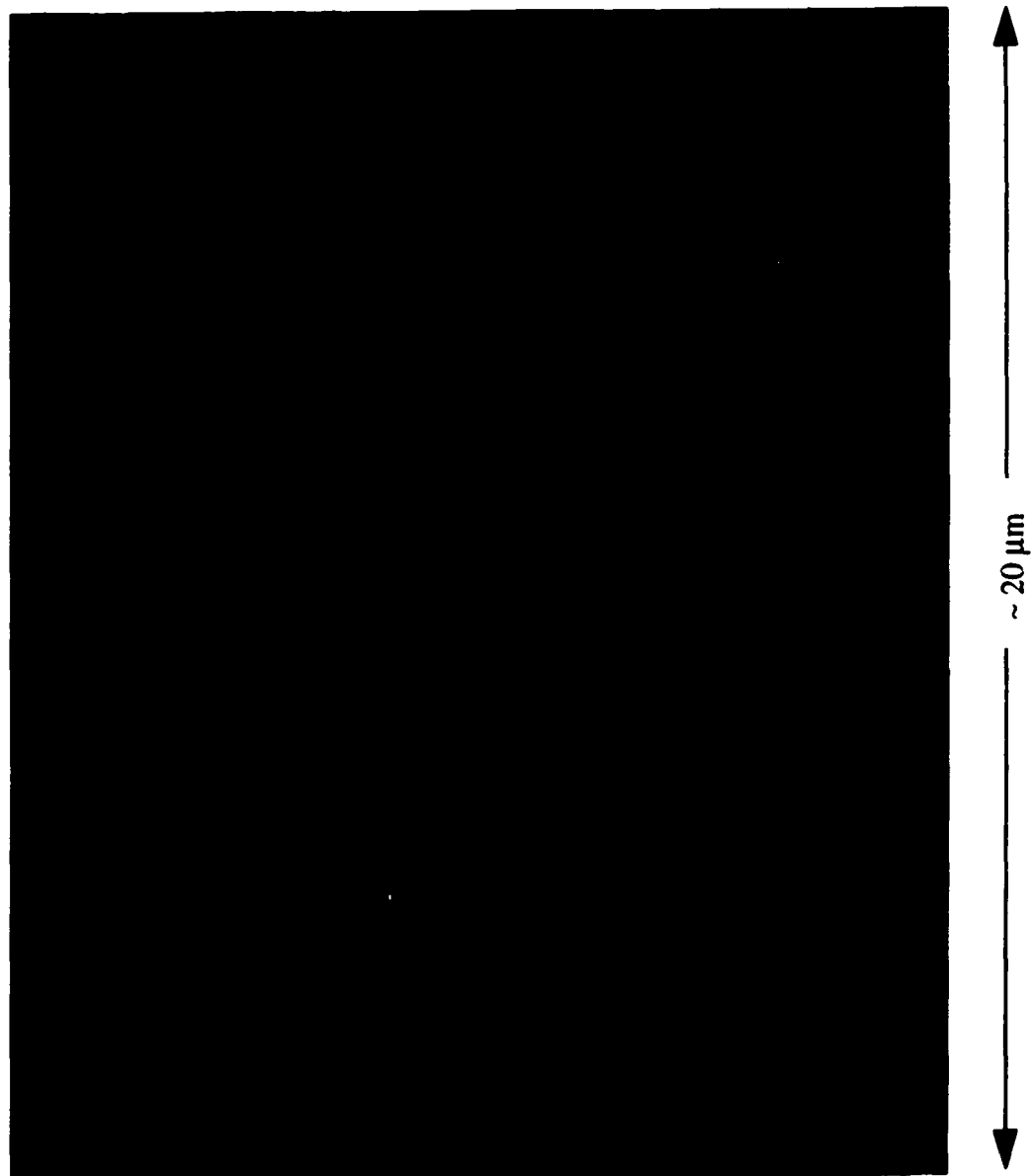


Figure 5.1. Optical microscope image of the Rust-Oleum Metallic Paint at a magnification of 40x.

of the Measurements Group reflective backing, shown in Figure 5.2, has some bubbles seen at a magnification of 20x.

In monochromatic photoelasticity with yellow light ($\lambda = 450 \text{ nm}$) the surface is considered effectively smooth if $(\frac{h}{\lambda}) \rightarrow 0$. This ratio equals 0.1 if $h = 45 \text{ nm}$ and will go to zero as h get smaller. A μm scale is used to observe the surface features in Figures 5.1 and 5.2. The metallic paint image showed areas out of focus that came into focus after a small turn of the fine adjustment knob. Estimation of the height difference between the focused and out-of-focused region was 0.5 to $1 \mu\text{m}$, which does not satisfy the ratio in the Rayleigh Criterion for a smooth surface. The Measurements Group reflective backing did not show as many out of focus areas as did the metallic paint, but the surface did reveal larger features, such as the bubbles seen in Figure 5.2. The second part of the Rayleigh Criterion is that the local angle of incidence goes to zero, $\gamma \rightarrow 0$. The spherical object on the right of Figure 5.2 measures approximately $7 \mu\text{m}$ in length. If this feature is thought of as a half buried ellipsoid with its semi-major axis measuring $3.5 \mu\text{m}$ and its semi-minor axis $0.5 \mu\text{m}$ (the lower approximation of the height difference from the metallic paint image), a right triangle can be constructed with the semi-major and semi-minor axes. An approximate slope can be calculated by taking the arctangent of the semi-minor to the semi-major axis yielding an inclination angle of 8° .

It is clear that both surfaces depolarize, to some degree, the incidence light because the Rayleigh Criterion for a smooth was not satisfied. Depolarization will cause the photoelastic fringe patterns to change resulting in uncertainties in the stress tensor components when combined with thermoelastic data. Due to this depolarization, the selection of reflective surfaces is a serious issue for photoelasticity when the results

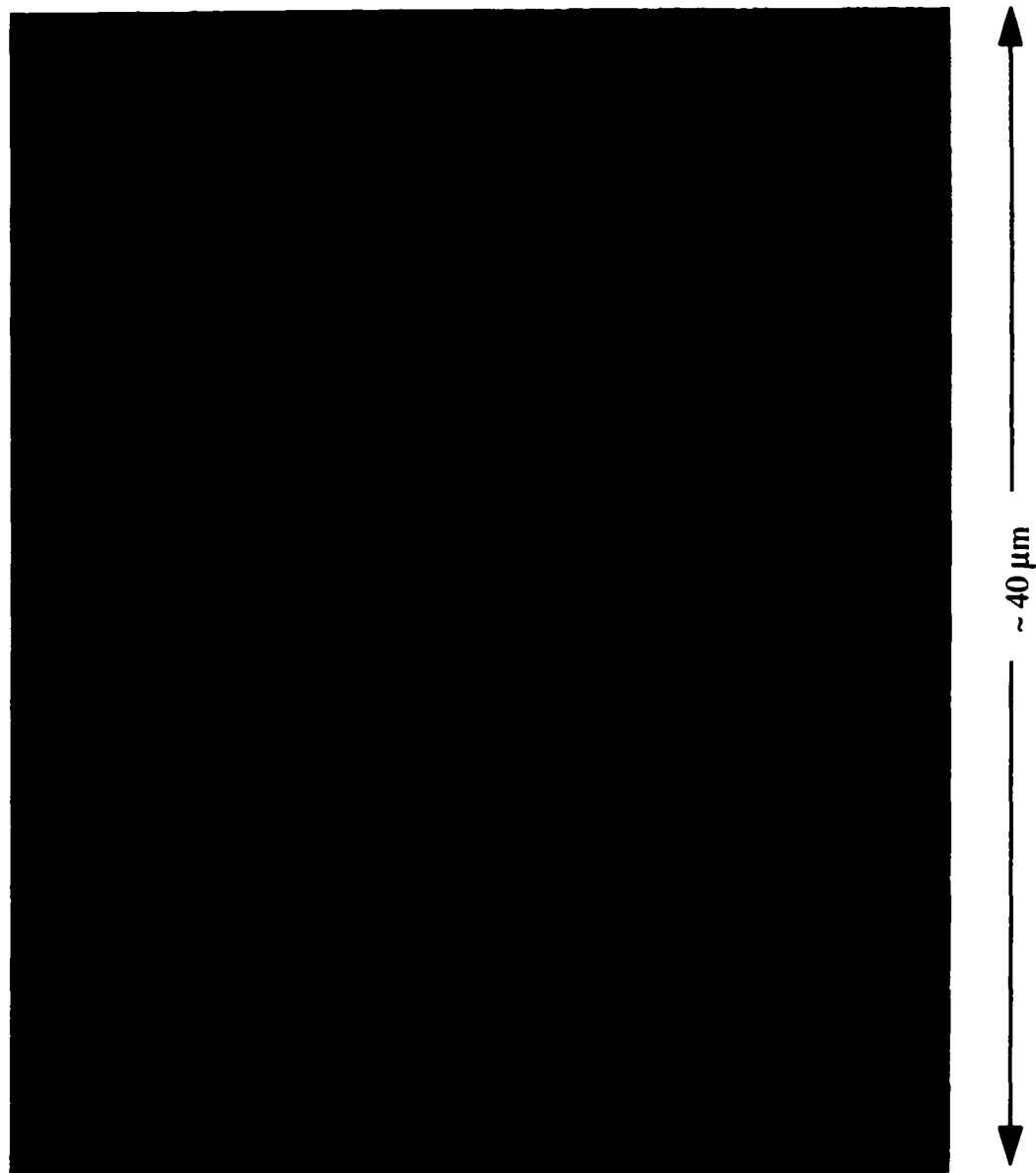


Figure 5.2. Optical microscope image of the Measurements Group reflective backing at a magnification of 20x.

are combined with other stress measurements. Depolarization effects have been largely ignored in the photoelastic community because the focus has been with the optical response of the clear, birefringent coatings which are desired to produce a large number of fringes for a relatively low applied stress. In addition, the isoclinic and isochromatic fringe patterns are interpreted on a full-field scale versus a pixel scale. Small changes in the fringe pattern due to depolarization will largely go unnoticed unless the fringe maps are examined on the pixel level. Also, photoelasticity has been used, to a large extent, as a qualitative rather than a quantitative stress measurement. More fringes indicate a higher stress. A quick measurement of fringe order by its color yields an approximate stress value for that region. If instead, thermoelastic and photoelastic measurement are to be combined to produce the full-field stress tensor, the photoelastic fringes must be analyzed at the pixel level. Any changes to the fringes as a result of depolarization will cause the stress tensor to be incorrect.

5.3 Depolarization by Scattering from Random Rough Surfaces

The calculation of the depolarization of electromagnetic waves scattered from objects or surfaces of given shape is easily described using geometric or ray optics. In many cases the result is nearly identical to that obtained from more sophisticated methods. In other cases, such as backscattering, the simplicity of geometric optics produces wrong results. Since the interest of this thesis is with the backscatter from a reflective surface, physical optics will be utilized which will approximate the boundary conditions of the wave equations.

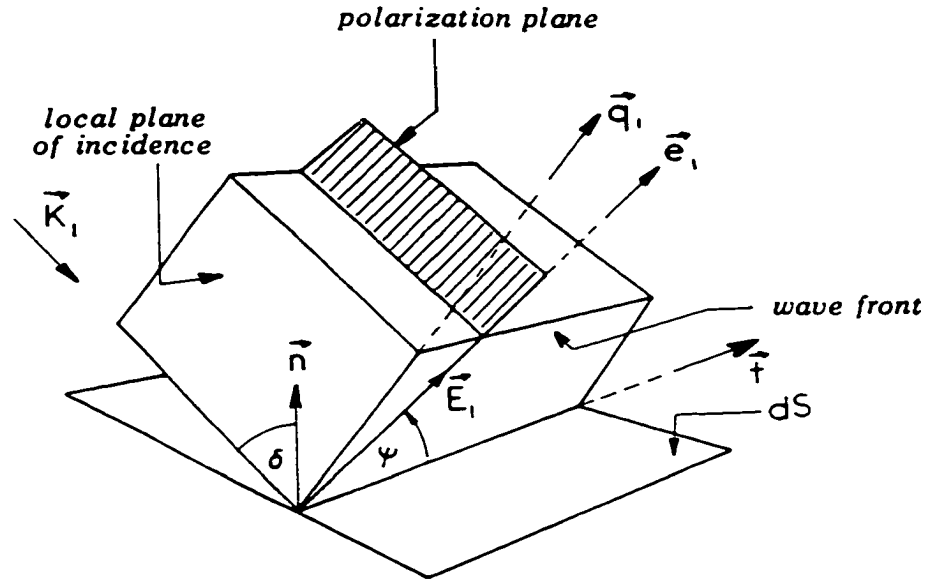


Figure 5.3. Vector diagram for an element dS at an arbitrary orientation in space [124].

The equation for the scattered field in the direction of the source (backscatter) is

$$\mathbf{E}_2 = A \iint (\mathbf{n} \cdot \mathbf{K}) [(\mathbf{e} \cdot \mathbf{t})(R^+ + R^-)\mathbf{t} - R^+\mathbf{e}] \exp(-2i\mathbf{k} \cdot \mathbf{r}) dS \quad (5.5)$$

where \mathbf{n} is the normal to the surface, \mathbf{K} is the propagation direction of the incident light, \mathbf{e} is the polarization direction, and \mathbf{t} is the intersection of the wave front with the sample which are shown in Figure 5.3. The reflected field will be elliptically polarized and can be represented by two linearly polarized waves, a linear (E_p) and cross-polarized (E_c) component,

$$E_p = \frac{A}{2} \iint \cos \delta [(R^+ - R^-) - (R^+ + R^-) \cos 2\psi] \times \exp(-2i\mathbf{k} \cdot \mathbf{r}) dS \quad (5.6a)$$

$$E_c = \frac{A}{2} \iint \cos \delta (R^+ + R^-) \sin 2\psi \exp(-2i\mathbf{k} \cdot \mathbf{r}) dS \quad (5.6b)$$

where δ is the local angle of incidence, ψ is the angle between the polarization of the incident field measured from the local plane of incidence, dS , and R^+ and R^- are Fresnel reflection coefficients. The Fresnel coefficients for two adjoining, non-

magnetic media are written as

$$R^+ = \frac{\bar{\epsilon} \cos \theta - \sqrt{\bar{\epsilon} - \sin^2 \theta}}{\bar{\epsilon} \cos \theta + \sqrt{\bar{\epsilon} - \sin^2 \theta}} \quad (5.7a)$$

$$R^- = \frac{\cos \theta - \sqrt{\bar{\epsilon} - \sin^2 \theta}}{\cos \theta + \sqrt{\bar{\epsilon} - \sin^2 \theta}} \quad (5.7b)$$

where θ is the incidence angle and $\bar{\epsilon}$ is the ratio of the permittivities between the two media, defined as

$$\bar{\epsilon} = \frac{\epsilon_r \mu_0}{\epsilon_p \mu_0} = \kappa + i60\lambda\sigma. \quad (5.8)$$

where κ is the dielectric constant, σ is the conductivity, and λ is the wavelength. The subscript r refers to the reflective surface and p to the photoelastic coating in this equation. Fresnel coefficients are important to this discussion because they provide information into the electrical properties of the media.

Considerable insight into the phenomenon of depolarized backscatter is offered by equations (5.6a-b). The integrand in equation (5.6b) indicates the parts of the surface that are responsible for the depolarization of the backscatter of radiation. Those surfaces that *do not* give rise to a cross-polarized component are $\delta = \pi/2$ (local grazing angle which will not backscatter any radiation), $\psi = 0$ or $\pi/2$ (elements so oriented that the polarization plane of the incident radiation is identical with, or perpendicular to, the local plane of incident), and $R^+ + R^- = 0$ (perfect conductor or $\mathbf{n} = -\mathbf{K}$, a mirroring element).

Further interpretation of the backscattered radiation can be done by dividing the wave into two components: a quasi-specular components returned by the mirrored elements whose normals point towards the source and diffuse components for those

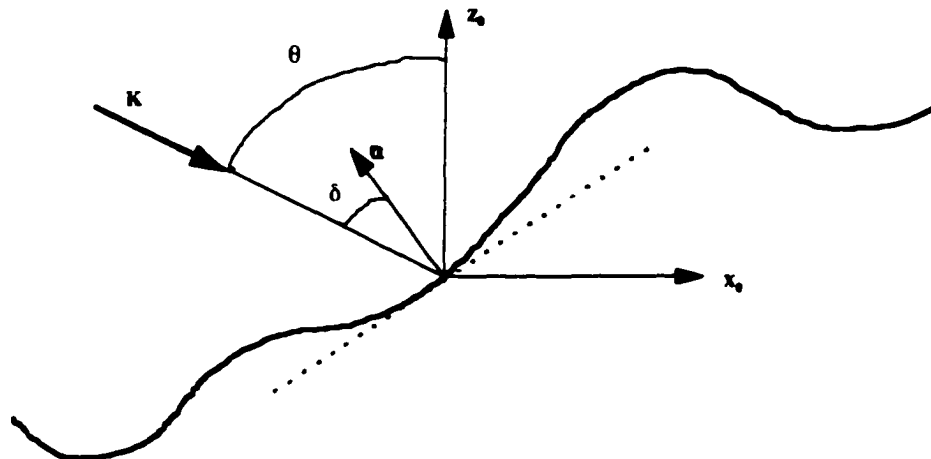


Figure 5.4. The local angle of incidence, δ , and its relation to the angle of incidence, θ . The angle of incidence is defined with respect to z_0 and constant for the whole surface whereas the local angle of incidence is defined from the normal at that location.

nonmirrored elements. Physically both components are re-radiated, but the difference lies with the quasi-specular case where the neighboring elements are reinforcing each other coherently whereas the phase for the diffuse case changes rapidly from point to point causing an incoherent addition. The magnitude of the cross-polarized component returned by the non-mirrored surface element depends on its orientation and the electrical properties of the surface. As the local angle of incidence, δ , approaches $\pi/2$, the cross-polarized component will decrease to zero.

To obtain quantitative results of the backscattered field and its polarization, the integral in equations (5.6a-b) must be evaluated. The local angle of incidence, depicted in Figure 5.4, is defined as

$$\cos \delta = \frac{Z_x \sin \theta + \cos \theta}{\sqrt{1 + Z_z^2 + Z_y^2}} \quad (5.9)$$

and the angle between the polarization plane and the local incident plane is given by

$$\cos \psi = \frac{\cos \beta^* (Z_x \cos \theta - \sin \theta) + Z_y \sin \beta^*}{\sqrt{1 + Z_z^2 + Z_y^2 - (Z_x \sin \theta + \cos \theta)^2}} \quad (5.10)$$

where the direction of incident polarization is defined by an angle β^* concluded by the incident polarization plane and the xy plane. The variables Z_x and Z_y are the partial derivatives of the surface S with respect to x and y , respectively, represented by a differential function $Z(x, y)$. The phase factors in (5.6a-b) are determined by

$$\mathbf{k} = \frac{2\pi}{\lambda} (\mathbf{x}_0 \sin \theta - \mathbf{z}_0 \cos \theta) \quad (5.11a)$$

$$\mathbf{r} = x \mathbf{x}_0 + y \mathbf{y}_0 + Z(x, y) \mathbf{z}_0. \quad (5.11b)$$

Polarization for a perfect conductor will remain constant for a given scattering direction even when the shape of the scattering surface is random because $R^+ = -R^-$. This occurs because the relative permittivity in equation (5.8) goes to infinity as $\sigma \rightarrow \infty$, for a perfect conductor, thereby reducing equation (5.7a-b) to $R^+ = 1$ and $R^- = -1$. For finite conductivity, the polarization depends on the shape of the surface. Since E_c and E_p will be used to describe the backscattered polarization, a random surface described by the variables, Z_x and Z_y , makes E_c and E_p random. The polarization of the backscattered wave is described by the cross-polarization ratio

$$P^2 = \frac{\langle E_c E_c^* \rangle}{\langle E_p E_p^* \rangle}, \quad (5.12)$$

which is the ratio of the mean cross-polarized power to the mean parallel-polarized power. Substitution of equations (5.6a-b) into equation (5.12) yields

$$\langle E_c E_c^* \rangle = \left| \frac{A}{2} \right|^2 \left\langle |\cos \delta (R^+ + R^-) \sin 2\psi|^2 \right\rangle \times \int \int \int \int \langle \exp [2i\mathbf{k} \cdot (\mathbf{r}_2 - \mathbf{r}_1)] \rangle dS_1 dS_2 \quad (5.13)$$

$$\langle E_p E_p^* \rangle = \left| \frac{A}{2} \right|^2 \left\langle |\cos \delta [(R^+ - R^-) - (R^+ + R^-) \cos 2\psi]|^2 \right\rangle \times \int \int \int \int \langle \exp [2i\mathbf{k} \cdot (\mathbf{r}_2 - \mathbf{r}_1)] \rangle dS_1 dS_2 \quad (5.14)$$

where the subscripts 1 and 2 refer to two variable points on S and the averaging in (5.13) and (5.14) is to be performed over the surface S . For the discussion of polarization, equation (5.12) can be approximated to [124]

$$P^2 \approx \frac{\langle |\cos \delta (R^+ + R^-) \sin 2\psi|^2 \rangle}{\langle |\cos \delta [(R^+ - R^-) - (R^+ + R^-) \cos 2\psi]|^2 \rangle} \quad (5.15)$$

which is valid for small illumination angles ($< 30^\circ$), very rough surfaces, and gentle slopes.

The relation between the mean square slope of the surface and depolarization is seen through equation (5.9). For a smooth surface, Z_x and $Z_y \rightarrow 0$ and the local angle of incidence approaches the illumination angle θ . For $\theta = 0$, no cross-polarization will be present. Therefore, as the mean square slope increases, δ will increasingly differ from θ resulting in more depolarization. Thus at small angles of incidence, the rougher of the two similar surfaces will depolarize more strongly. A plot of P^2 versus illumination angle for various rms slopes is shown in Figure 5.5. As the rms value increases, the cross-polarization ratio becomes larger resulting in more depolarization. Thus the cross-polarization ratio is a measure of depolarization [123].

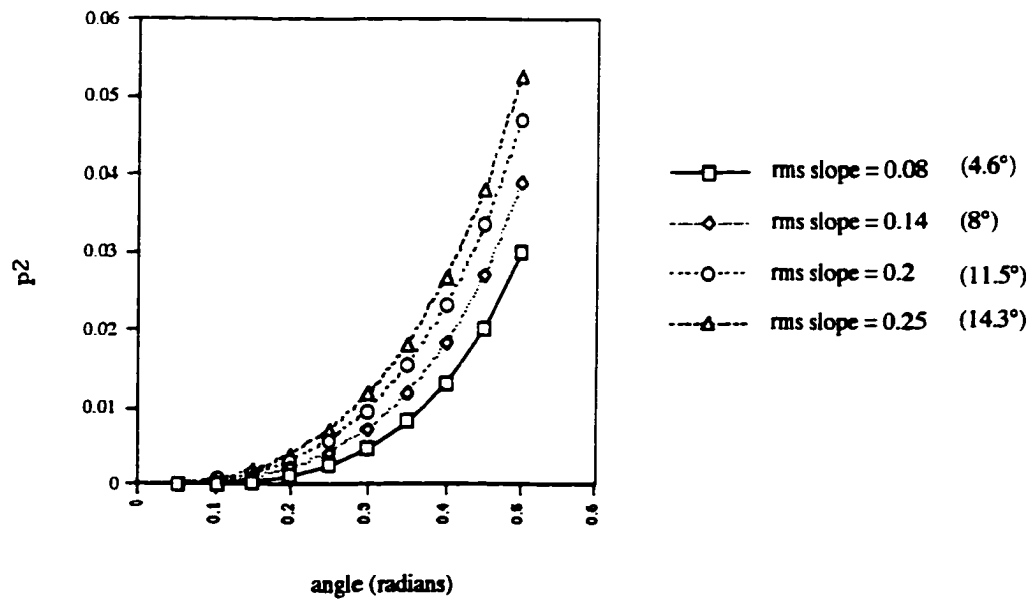


Figure 5.5. Cross-polarization ratio versus incidence angle, θ . As the rms slope increases, so does the depolarization. In this simulation, the relative permittivity was four and $\beta = 45^\circ$.

5.3.1 Depolarization of Isoclinic Fringes

In the isoclinic model, it was assumed that the reflective surface was a perfect retroreflector producing a wave of the form

$$\vec{E}'_R = [\hat{x}' \cos(\theta - \phi) e^{i\Gamma_e} + \hat{y}' \sin(\theta - \phi) e^{i\Gamma_o}] A e^{ik_o z}. \quad (5.16)$$

If the reflective layer is considered to be an imperfect retroreflector, the cross-polarized component of the wave becomes larger with increasing rms slope (roughness) leading to the depolarization of the incidence wave. The cross-polarized component in the anisotropic electromagnetic boundary value model is the extraordinary wave. Its amplitude increases because of the depolarization effects of the reflective surface. In the retroreflection case, the amplitudes of the reflective waves were D'_e and D'_o for the extraordinary and ordinary waves respectively. If the amplitude of the extraordinary wave is to increase by an amount upon reflection, then the amplitude of the ordinary wave will decrease by the same amount, in the case of a lossless medium. This results in a factor of $(1 + P)$ multiplied to D'_e and $(1 - P)$ to D'_o in equation (4.7c). The variable P will be a random number ranging from zero to one and will model the amount of energy transfer between the two waves. In addition, it was assumed that the incident light was normal to the front and back surfaces of the object. Deviation from normal incidence elongates the path length. The new path length will change from d , the thickness of the photoelastic coating, to $d \sec \psi$ where ψ is measured from the normal shown in Figure 5.6. Recalculating B'_x and B'_y in equation (4.7b) results in a new expression for the reflected wave

$$\vec{E}'_R = \hat{x}' [C_e \cos(\theta - \phi) e^{i\Omega_e} + \hat{y}' C_o \sin(\theta - \phi) e^{i\Omega_o}] e^{ik_o z} \quad (5.17)$$

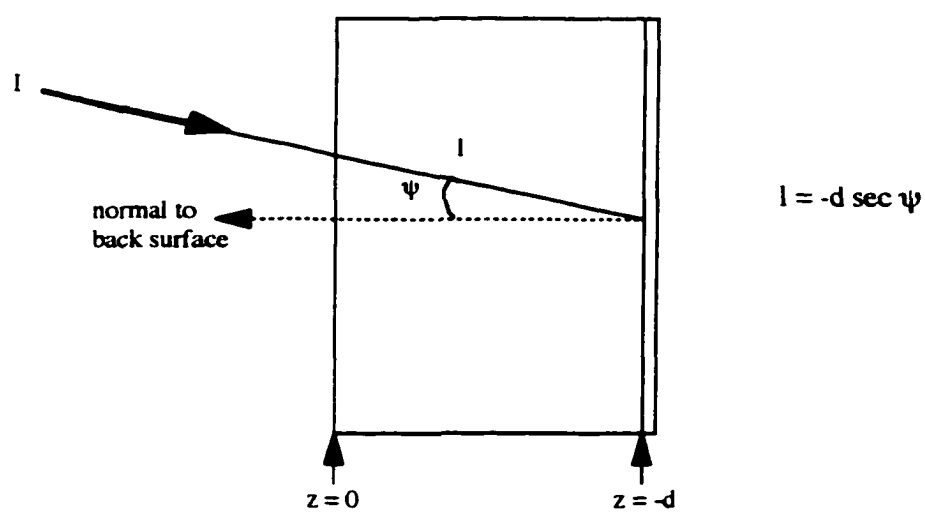


Figure 5.6. There is a change in path length due to off normal incidence. The new path length is $-d \sec \psi$.

where

$$C_e = \frac{\sqrt{N_1^2 \cos^4 \alpha + N_2^2 \sin^4 \alpha - \sin^2(2\alpha) \left[\frac{1}{2} N_1 N_2 - 16n_e^2(1+P)^2 \right]}}{\cos^2 \alpha [P + n_e(2+P)]^2 + \sin^2 \alpha [2 + P(1+n_e)]^2} \quad (5.18)$$

$$C_o = \frac{\sqrt{M_1^2 \cos^4 \beta + M_2^2 \sin^4 \beta + \sin^2(2\beta) \left[\frac{1}{2} M_1 M_2 + 16n_o^2(P-1)^2 \right]}}{\cos^2 \beta [P + n_o(P-2)]^2 + \sin^2 \beta [P(1-n_o) - 2]^2} \quad (5.19)$$

$$\Omega_e = \arctan \left[\frac{-4n_e(1+P) \sin(2\alpha)}{N_2 \sin^2 \alpha - N_1 \cos^2 \alpha} \right] \quad (5.20)$$

$$\Omega_o = \arctan \left[\frac{4n_o(P-1) \sin(2\beta)}{M_1 \sin^2 \beta + M_2 \cos^2 \beta} \right] \quad (5.21)$$

$$N_1 = -P^2 + n_e^2(2+P)^2 \quad (5.22a)$$

$$N_2 = 4(1+P) + P^2(n_e^2 - 1) \quad (5.22b)$$

$$\alpha = K_e d \sec \psi \quad (5.22c)$$

$$M_1 = P^2 - n_o^2(P-2)^2 \quad (5.23a)$$

$$M_2 = 4(1-P) - P^2(n_o^2 - 1) \quad (5.23b)$$

$$\beta = K_o d \sec \psi \quad (5.23c)$$

To observe the effects of imperfect retroreflection and off-normal incidence, equation (5.17) was converted to an intensity equation as discussed in Section 4.1. The results for a hole in plate under vertical tension are shown in Figure 5.7. Notice that as the amount of energy transfer between the waves increases due to depolarization, the fringe patterns degrade.

Knowledge of the amount of fringe degradation can be used to determine the amount of depolarization inflicted on the reflected wave thereby making it possible to rate the reflective backings. This rating system would provide a means to identify good and poor materials to be used in reflection photoelasticity and its integration with thermoelasticity. Various techniques were used to analyze these degraded fringes for a quantitative comparison between the images. One such method looked at fringe areas. Figure 5.7 shows the top portion of the 0° isoclinic fringes for the Kirsch problem. This region is made up of four lobes, two small and two large, which change size and shape as the angle from normal incidence and depolarization increase. Comparison of these lobe areas between the images provided very little quantitative information. In some cases, such as the zero depolarization and 10° off normal incidence, the small lobe substantially decreased in size in comparison with the 25% and 50% depolarization at normal incidence. The same was true for the large lobe at 5° . Even the ratio of the lobe areas between the levels of depolarization did not provide any results that could rate the reflective backings as good or poor.

The second analytical technique was with the comparison of isoclinic lines between the degraded fringes. The isoclinic lines, in increments of 5° , for a hole in a plate under uniaxial tension are shown in Figure 4.15. In the second quadrant there is a linear 0° isoclinic between the 5° and 85° lines which was selected for the comparison between the degraded images. This line corresponded to the region between the left small and large lobes seen in Figure 5.7. The degraded images were read into a Mathematica program which converted the pictures into a matrix of numbers where the value of "5" was assigned to the lobe areas and "0" everywhere else. A region

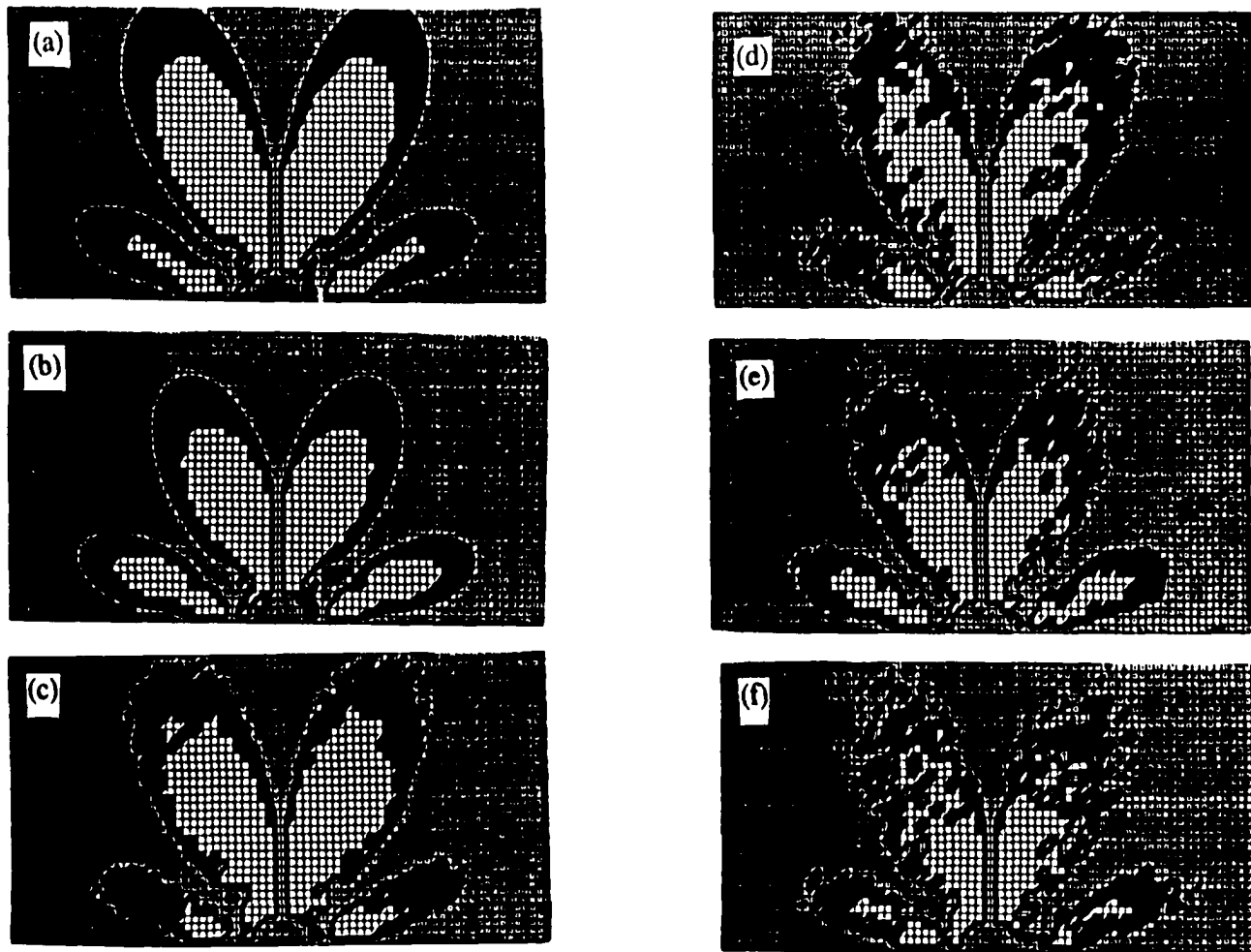


Figure 5.7. Degradation of the fringes from the Kirsch problem for (a) zero depolarization and normal incidence, (b) zero depolarization and 5° from normal incidence, (c) 25% depolarization and normal incidence, (d) 25% depolarization and 5° , (e) 50% depolarization and normal incidence, and (f) 50% depolarization and 5° .

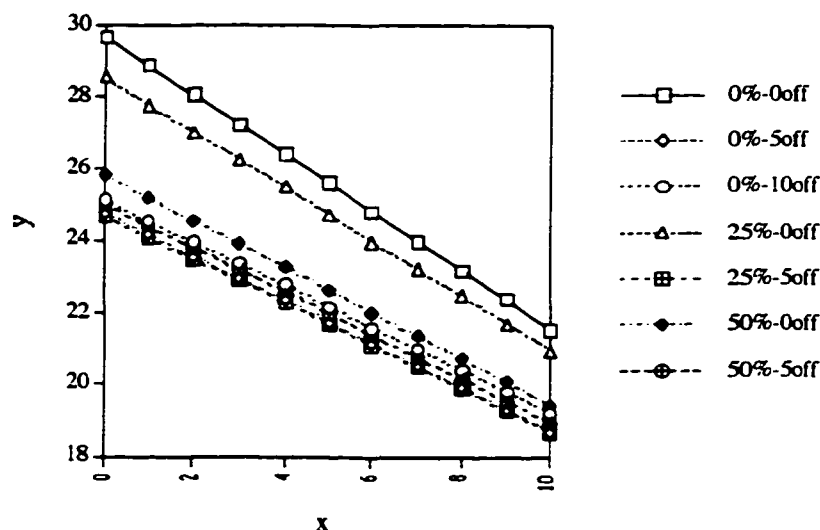


Figure 5.8. Best fit isoclinic lines for various depolarizations and angles off normal incidence for the Kirsch problem.

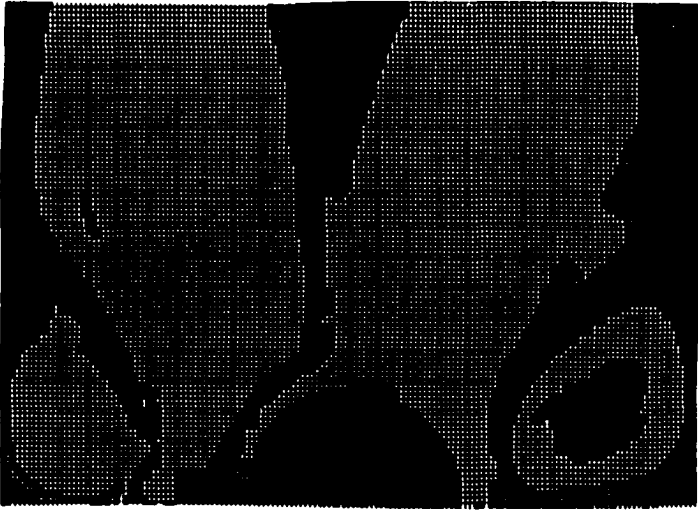
was selected in the normal incidence, no depolarization case to fit the best linear line in the “0” area between the left small and large lobes. This procedure was repeated for the remainder of the test cases – combinations of energy transfers, P , of 0%, 25%, and 50% and angles of incidence ranging from 0° to 10° – keeping the initial selected region constant in all of the images. As the amount of depolarization and oblique angle increased, the region between the lobes in this selected region changed. As a result, the best fit 0° isoclinic line moved, illustrated in Figure 5.8 which shows the results of the best fit line for all of the simulations. As the reflective backing becomes an imperfect retroreflector and slightly oblique incidence light is used, the isoclinic line shifts down. Comparison between the actual position of the isoclinic line at this location to the one observed with a particular reflective backing provides a quantitative distinction between good and bad reflective materials. Because the hole in plate under uniaxial tension is a

well known and understood problem, this geometry will be used for the comparison of reflective backings.

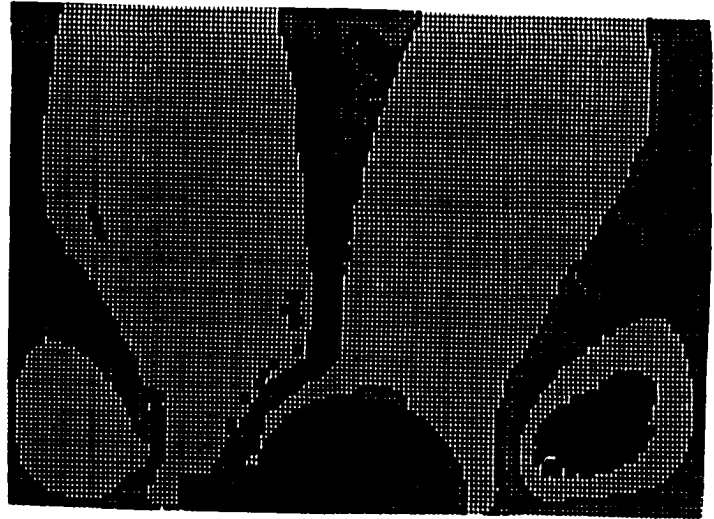
A similar analysis was done with the notched hole and two different diameter holes in a plate under uniaxial tension. For the notched hole, shown in Figure 5.9, the arced line towards the top of the drilled hole was selected for the region of comparison.

The best fit quadratic line was calculated for the same cases as with the Kirsch problem. The results, seen in Figure 5.10, again show movement of this line but with less influence on the depolarization compared with the angle off from normal incidence. For the two holes in a plate with different diameters, a linear isoclinic line was constructed in the upper right region of the smaller hole between the two lobes (identical to that of the Kirsch problem analysis). Here again there is evidence of the isoclinic line moving due to depolarization and off normal incidence as shown in Figure 5.11. This line was much more influenced by depolarization, as in the Kirsch problem, as compared with the isoclinic line in the notch hole example. This could be an indication that certain fringes are more susceptible to movement by the depolarization of the reflective backing than others. But in all cases, the location of the isoclinic line was influenced by the off normal incidence angle.

Because thermoelastic and photoelastic images are going to be combined pixel by pixel to determine the stress tensor components, movement of the isoclinic lines results in principal angles being assigned to the wrong pixels. Simulations were done to reconstruct the stress tensor using equations (4.43a-c). A location was considered where the principal direction was 0° and stress values were 943 psi, -120.9 psi, and 0 psi for T_x , T_y , and T_{xy} respectively. This stress matrix was rotated to the principal stress



(a)



(b)

Figure 5.9. Degradation of the FEA model for the notched hole at (a) zero depolarization and normal incidence and (b) 25% depolarization and normal incidence.

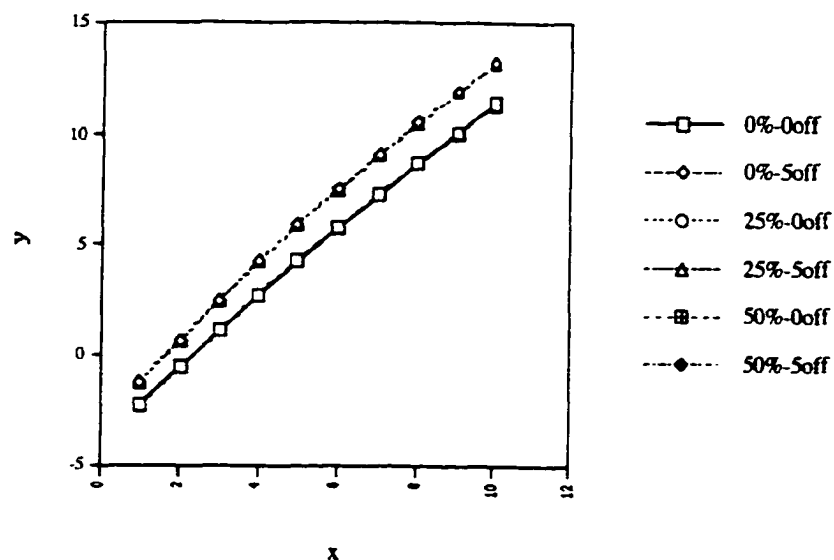


Figure 5.10. Best fit lines for various depolarizations and off normal incidence for the notched hole.

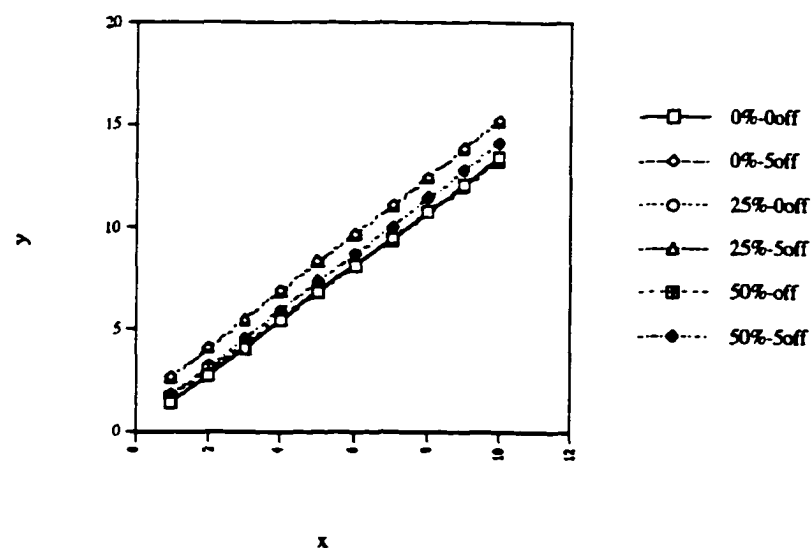


Figure 5.11. Best fit isoclinic lines for various depolarizations and angles off normal incidence for the two holes in a plate with different diameters.

axes and the sum and difference of the principal stresses were determined. These values were used for the thermoelastic and photoelastic measurements in equations (4.43a-c), and the stress tensor components were calculated. The principal angle was varied in this simulation so that its influence on the stress component could be observed. The results are given in Table 5.1.

Table 5.1. Stress tensor components subjected to variations in angle.

θ	T_x (psi)	T_y (psi)	T_{xy} (psi)
0°	943	-120.9	0
0.5°	942.92	-120.82	9.28
1°	942.68	-120.58	18.56
2°	941.70	-119.60	37.11
3°	940.09	-117.99	55.60
4°	937.82	-115.72	74.03

The first row in Table 5.1 shows the correct numerical values for each of the components. Notice that T_x and T_y at 4° are less than 5% off from the expected values whereas the value of T_{xy} at 4° is 8% that of T_x at 0° . From this it can be concluded that the simulations show that the shear stress is sensitive to errors in principal angle. Although the shear stress uncertainty is 8% at 4° , this value cannot be considered small or large because of the wide range of stress tolerance levels that structures can handle. A related question is the influence that errors in the difference of the principal stresses have on the stress components.

5.3.2 Depolarization of Isochromatic Fringes

Making the same additions to the isochromatic model, as in the depolarized isoclinic model, changes the reflective wave from

$$\vec{E}'_R = \left(\hat{x}' A_{Bx} e^{i\Lambda_e} e^{-i\pi/2} + \hat{y}' A_{By} e^{i\Lambda_o} \right) e^{ik_o z} \quad (5.24)$$

where

$$A_{Bx} = \frac{\left(\frac{A_y}{\sqrt{2}} \right) [(1 + n_e^2) + (-1 + n_e^2) \cos(2K_1 d)]}{\sin^2(K_1 d) + n_e^2 \cos^2(K_1 d)} \quad (5.25a)$$

$$\Lambda_e = \tan^{-1} \left[\frac{\varrho_e \sin\left(\frac{\pi}{4} - \theta\right) + n_e \sin(2K_1 d) \cos\left(\frac{\pi}{4} - \theta\right)}{\varrho_e \cos\left(\frac{\pi}{4} - \theta\right) - n_e \sin(2K_1 d) \sin\left(\frac{\pi}{4} - \theta\right)} \right] \quad (5.25b)$$

$$\varrho_e = n_e^2 \cos^2(K_1 d) - \sin^2(K_1 d) \quad (5.25c)$$

$$A_{By} = \frac{\left(\frac{A_y}{\sqrt{2}} \right) [(1 + n_o^2) + (-1 + n_o^2) \cos(2K_2 d)]}{\sin^2(K_2 d) + n_o^2 \cos^2(K_2 d)} \quad (5.25d)$$

$$\Lambda_o = \tan^{-1} \left[\frac{\varrho_o \sin\left(\frac{\pi}{4} - \theta\right) + n_o \sin(2K_2 d) \cos\left(\frac{\pi}{4} - \theta\right)}{\varrho_o \cos\left(\frac{\pi}{4} - \theta\right) - n_o \sin(2K_2 d) \sin\left(\frac{\pi}{4} - \theta\right)} \right] \quad (5.25e)$$

$$\varrho_o = n_o^2 \cos^2(K_2 d) - \sin^2(K_2 d), \quad (5.25f)$$

to

$$\vec{E}'_R = [\hat{x}' C_e^c e^{i\Upsilon_e} e^{-i\pi/2} + \hat{y}' C_o^c e^{i\Upsilon_o}] A e^{ik_o z} \quad (5.26)$$

where

$$C_e^c = \frac{A \sqrt{(\xi_1)^2 + (\xi_2)^2}}{[-P(1 + n_e) - 2n_e]^2 \cos^2 \alpha + [2 + P(1 + n_e)]^2 \sin^2 \alpha} \quad (5.27a)$$

$$\xi_1 = \zeta^+ F_1 \cos^2 \alpha - \zeta^- F_2 \sin 2\alpha - \zeta^+ F_3 \sin^2 \alpha \quad (5.27b)$$

$$\xi_2 = \zeta^- F_1 \cos^2 \alpha + \zeta^+ F_2 \sin 2\alpha - \zeta^- F_3 \sin^2 \alpha \quad (5.27c)$$

$$C_o^c = \frac{A \sqrt{(\xi_3)^2 + (\xi_4)^2}}{[P(1 + n_o) - 2n_o]^2 \cos^2 \beta + [2 - P(1 + n_o)]^2 \sin^2 \beta} \quad (5.28a)$$

$$\xi_3 = \zeta^+ G_1 \cos^2 \beta + \zeta^- G_2 \sin 2\beta + \zeta^+ G_3 \sin^2 \beta \quad (5.28b)$$

$$\xi_4 = \zeta^- G_1 \cos^2 \beta - \zeta^+ G_2 \sin 2\beta + \zeta^- G_3 \sin^2 \beta \quad (5.28c)$$

$$\Upsilon_e = \arctan \left[\frac{\xi_2}{\xi_1} \right] \quad (5.29a)$$

$$\Upsilon_o = \arctan \left[\frac{\xi_4}{\xi_3} \right] \quad (5.29b)$$

$$\zeta^- = (\cos \theta - \sin \theta) \quad (5.29c)$$

$$\zeta^+ = (\cos \theta + \sin \theta) \quad (5.29d)$$

$$F_1 = 2n_e^2(1 + P) + \left(\frac{1}{2}\right) P^2(n_e^2 - 1) \quad (5.30)$$

$$F_2 = 2n_e(1 + P) \quad (5.31)$$

$$F_3 = 2(1 + P) + \left(\frac{1}{2}\right) P^2(1 - n_e^2) \quad (5.32)$$

$$G_1 = 2n_o^2(P - 1) + \left(\frac{1}{2}\right) P^2(1 - n_o^2) \quad (5.33a)$$

$$G_2 = 2n_o(1 - P) \quad (5.33b)$$

$$G_3 = 2(1 - P) + \left(\frac{1}{2}\right) P^2(1 - n_o^2). \quad (5.33c)$$

Equation (5.24) was converted to an intensity equation, as done in Section 4.2 to observe the effects of imperfect retroreflection and off-normal incidence. The results for a hole in plate under uniaxial tension are shown in Figure 5.12. Notice again that as the amount of depolarization increases, the fringe patterns degrade. With the isochromatic fringes providing the difference of the principal stresses and the depolarization distorting the size and shape of the fringe, a pixel on outer edge of a fringe in the one simulation case may be totally outside of the same fringe in a more degraded images. The actual value for the difference of the principal stresses at that pixel location has changed as a result of imperfect retroreflection due to a rough surface and off normal incidence. The influence of the stress tensor elements to uncertainties in the difference of the principal stresses due to depolarization can be seen in Table 5.2.

Table 5.2. Stress tensor components subjected to variations in stresses.

$T_{x'} - T_{y'}$	T_x (psi)	T_y (psi)	T_{xy} (psi)
1063.9	943	-120.9	0
-5%	916.40	-94.3	0
-10%	889.81	-67.7	0
-20%	836.61	-14.51	0
+5%	969.60	-147.50	0
+10%	996.20	-174.10	0
+20%	1049.39	-227.29	0

It is evident that uncertainties in the difference of the principal stresses influence T_y . With errors in both the principal stress direction and the difference of the principal stresses, the reconstructed values for T_y and T_{xy} can be significantly different from their true value given in Table 5.3.

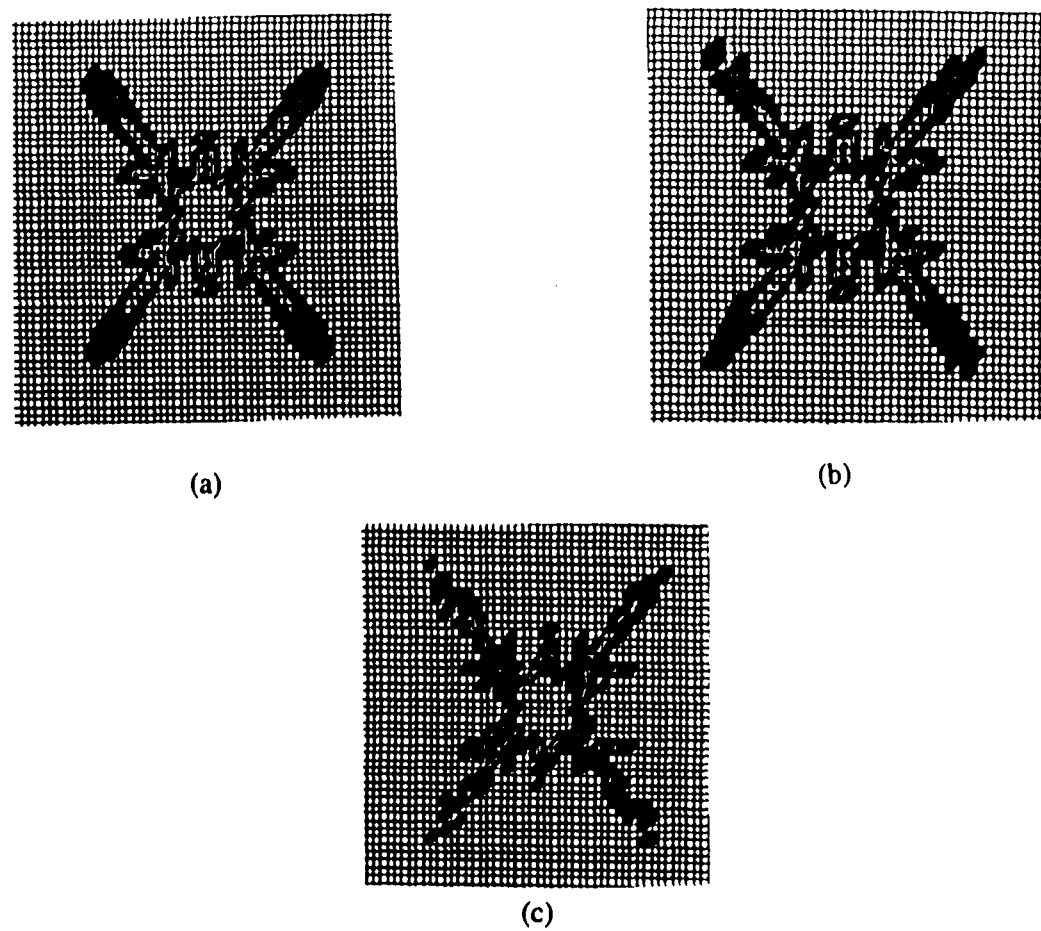


Figure 5.12. Degradation of the isochromatic fringes with (a) zero, (b) 25% depolarization, and (c) 50 % depolarization.

Table 5.3. Stress tensor components with errors in the angle and stresses.

θ	$T_{x'} - T_{y'}$	T_x (psi)	T_y (psi)	T_{xy} (psi)
0°	1063.9	943	-120.9	0
2°	+5%	968.24	-146.14	38.96
2°	+10%	944.77	-172.67	40.81
2°	-5%	915.17	-93.07	35.25
2°	-10%	888.64	-66.54	33.39

For the stress tensor components to be calculated with any certainty, the amount of depolarization has to be determined so that its influence on the resulting fringe patterns can be removed. Comparison between the location of the isoclinic fringes can not only be used to rate the reflective backing but also to determine the amount of correction needed to restore the fringe patterns to their unaltered configuration. The rating scheme will aid in the selection of materials for the reflective backing that produce the least amount of depolarization. Any remaining depolarization effect causing the fringes to move can be corrected by a computer algorithm before the information is integrated with thermoelastic measurements.

The two reflective backings used in this project, Rust-Oleum metallic paint and the Measurements Group polycarbonate sheet with reflective backing, produced identical fringe patterns under the same loading condition. Efforts to create a data base of degraded fringe patterns so as to rate the reflective surfaces as either good or poor were outside of the scope of this project. Further work with the integration of thermoelastic and photoelastic stress measurements will not only address the reflective backings causing depolarization but also technical issues associated with the collection of thermoelastic and photoelastic data, such image resolution between the two measurement systems.

Chapter 6

Summary and Future Direction

Thermoelastic and photoelastic stress analysis effectively provide information about the sum and the difference of the principal stresses, respectively. Combining these two full-field, non-contact nondestructive evaluation techniques allows the individual stress components to be measured. One of the main difficulties in merging these two measurement systems was in identifying an appropriate surface coating. Thermoelasticity demands a highly emissive surface, while photoelasticity requires a stress-induced birefringent, transparent coating with a retro-reflective backing. Two coatings have been identified that can be used for combined thermoelastic and photoelastic stress measurements: PMMA and polycarbonate. Both are clear plastic materials which produced fringe patterns when exposed to an applied load and illuminated with polarized light. The polycarbonate material was a film designed specifically for photoelastic analysis and the PMMA was a general use plexiglas. Both produced clearly defined fringe patterns when observed with a polariscope. When subjected to a cyclic load and viewed with a thermographic imager synchronized to the loading, both materials produced temperature fluctuations on the surface in response to tensile and compressive stresses induced by the applied load. The chemical make-up of the PMMA and polycarbonate is such that the clear coatings are opaque in the infrared producing a high emissive surface which allows for thermoelastic stress analysis.

Without the identification of a common coating, the two systems could not have been linked. The next step towards integrating thermoelasticity with photoelasticity measurements involved understanding the mechanisms by which these coatings exhibited fringe patterns and temperature fluctuations when exposed to an applied stress. Mechanical deformation in the object causes a local temperature change which is proportional to the sum of the principal stresses in that region. With the knowledge of the stresses over the surface of an object, a temperature map can be easily constructed by converting the stresses to principal stresses and summing the elements. On the other hand, the production of photoelastic fringes due to the induced anisotropy was not so easily modeled and became the theoretical focus of this thesis. An anisotropic electromagnetic boundary value model was developed using the electromagnetic wave theory. This model produced intensity contour maps which matched the fringe patterns observed in the laboratory. The model used material properties, such as the index of refraction and stress-optic coefficients, and the induced stress field to produce the intensity contour maps. The material properties are tabulated for most substances, and the stress field can be calculated by classical mechanical equations or from finite element analysis.

With a theoretical photoelastic model in place, an understanding of fringe production as a result of an applied stress was possible. The model assumed normally incident light and perfect reflection from the reflective backing, but laboratory conditions fall short of these assumptions. An anisotropic electromagnetic boundary value model was used to simulate fringe patterns, where the incident light was at a small angle from the normal and the reflective backing was an imperfect retro-reflector.

As the experimental conditions changed, modifications to the fringes were noted. The reflective backing becoming an imperfect retro-reflector was a result of it being a rough surface which depolarized the light wave. As the surface became rougher, more depolarization occurred which in turn degraded the photoelastic fringes. A quantitative analysis of the degraded fringes, to be used as a rating scheme for reflective backing materials, showed that the isoclinic lines shift position as a result of the depolarization and oblique incidence. This is a concern when calculating the stress components through the combination of photoelasticity and thermoelasticity because the data maps are going to be integrated at the pixel level. Small shifts in the photoelastic fringes result in incorrect information being assigned to some pixels resulting in uncertainties in the stress tensor components [126-128]. Progress in the understanding of the depolarization at the reflective backing should lead to the selection of new materials that will minimize this effect, depolarization, as well as the development of computer algorithms to correct for any remaining depolarization.

The primary impediment to the photoelastic/thermoelastic measurement system, experimentally, seems to be the expense of the thermoelastic stress measurement system and the inherent image resolution limitations of their relatively small detector array. The DeltaTherm 1000 imager used for this thesis has a spacial resolution of 128 x 128 pixels for a cost of \$150k (\$9 per pixel). The Model 030 Polariscope which used a Polaroid Digital Camera with a maximum resolution of 1600 x 1200 pixels and sells for \$5000 and the digital camera for \$1200 (total system, \$0.003 per pixel). The resolution mismatch between the two stress systems were solved through linear interpolation of the thermal images to match the photoelastic images. New

technologies are having an impact on thermal methods, especially with the advance in detector arrays. Current microbolometer focal plane arrays have a spacial resolution of 320 x 240 pixels at a projected cost of \$15k (\$0.19 per pixel). Their use in the thermoelastic community has been limited because its thermal resolution is much worse than other radiometers, 50 mK compared to the 1 mK of the DeltaTherm 1000. A poorer temperature resolution equates to a lower stress sensitivity. However, advances in computer processing have been able to bring this detector into the thermoelastic community by averaging lots of data per second which counteracts the higher thermal resolution. As the price of the thermoelastic system decreases and the spacial resolution increases, combined photoelasticity/thermoelasticity will become a more practical technique for the measurement of the stress tensor components.

This thesis demonstrates that thermoelastic and photoelastic stress measurements can be integrated to produce the full-field stress tensor components. This is a novel measurement method because past techniques could only produce this information at select points. This thesis is just the beginning of many new and exciting developments in the field of stress analysis. Besides the identification of additional materials suitable for thermoelastic and photoelastic stress analysis, a redesign of the photoelastic apparatus is possible. The polariscope is about the size of a football and its design has largely remained unchanged for decades. The polariscope consists of a lighting source, polarizers, and quarter-wave plates. The polarizers are large enough to permit recording equipment, such as digital cameras, to capture the photoelastic images. A hand-held version of a polariscope can be developed using a digital camera with a polarizers in front of the lens and the flash. The major cost with this new system would

be with the camera, which is currently priced at around \$800. One could envision walking around the lab, and the field, and snapping photoelastic images with ease. Later these images would be uploaded into a computer for automated processing of the data. A further redesign of the polariscope would size it down to the fiber-optic (mini) cameras for integration into the thermoelastic systems. This would provide simultaneous data collection between the two systems preventing problems, such as alignment and viewing angle mismatches between the two data images, from occurring. The data would be obtained, processed, and displayed immediately.

APPENDIX A Fresnel's Equation

Assume that the medium is nonconducting, magnetically isotropic, and no currents or charges present. Maxwell's equations are written as

$$\nabla \cdot \mathbf{D} = 0 \quad (\text{A.1a})$$

$$\nabla \cdot \mathbf{B} = 0 \quad (\text{A.1b})$$

$$\nabla \times \mathbf{E} = -\frac{\partial \mathbf{B}}{\partial t} \quad (\text{A.1c})$$

$$\nabla \times \mathbf{H} = \frac{\partial \mathbf{D}}{\partial t}. \quad (\text{A.1d})$$

Interpretation of these equations can be done using plane waves written as

$$\mathbf{E} = \mathbf{E}_0 \exp[i(\omega t - \mathbf{k} \cdot \mathbf{r} + \phi)] \quad (\text{A.2a})$$

$$\mathbf{D} = \mathbf{D}_0 \exp[i(\omega t - \mathbf{k} \cdot \mathbf{r} + \phi)] \quad (\text{A.2b})$$

$$\mathbf{B} = \mathbf{B}_0 \exp[i(\omega t - \mathbf{k} \cdot \mathbf{r} + \phi)] \quad (\text{A.2c})$$

$$\mathbf{H} = \mu \mathbf{B}. \quad (\text{A.2d})$$

Substituting equation (A.2a-d) into the first two Maxwell equations yields

$$\nabla \cdot \mathbf{D} = -i\mathbf{k} \cdot \mathbf{D} = 0 \quad (\text{A.3})$$

and

$$\nabla \cdot \mathbf{B} = \mu \nabla \cdot \mathbf{H} = -i\mathbf{k} \cdot \mathbf{H} = 0. \quad (\text{A.4})$$

These two equations imply \mathbf{D} , \mathbf{B} , and \mathbf{H} are perpendicular to \mathbf{k} but not necessarily to \mathbf{E} due to the relation $E_i = \epsilon_{ij} D_j$. Substitution of the plane waves into the second two Maxwell equations yields

$$i\mathbf{k} \times \mathbf{H} = i\omega\mathbf{D} \quad (\text{A.5})$$

and

$$i\mathbf{k} \times \mathbf{E} = i\omega\mathbf{B} = i\omega\mu_0\mathbf{H}. \quad (\text{A.6})$$

These equations require \mathbf{H} be perpendicular to both \mathbf{k} and \mathbf{D} as well as to \mathbf{k} and \mathbf{E} .

With \mathbf{E} not perpendicular to \mathbf{k} , the scalar product $\mathbf{k} \cdot \mathbf{E} \neq 0$. To calculate the product of the electric field and the wave vector, the cross product of \mathbf{k} with equation (A.6) yields

$$\mathbf{k} \times (\mathbf{k} \times \mathbf{E}) = \omega\mu_0\mathbf{k} \times \mathbf{H} = \omega\mu_0(-\omega\mathbf{D}). \quad (\text{A.7})$$

Rewriting this as

$$\mathbf{k}(\mathbf{k} \cdot \mathbf{E}) - \mathbf{E}(\mathbf{k} \cdot \mathbf{k}) = -\omega^2\mu_0\mathbf{D} \quad (\text{A.8})$$

and identifying the propagation constant as

$$k^2 = \left(\frac{n\omega}{c}\right)^2, \quad (\text{A.9})$$

a new expression for the dot product of $\mathbf{k} \cdot \mathbf{E}$ is developed,

$$\frac{\mathbf{k}}{k^2}(\mathbf{k} \cdot \mathbf{E}) = \mathbf{E} - \frac{c^2\mu_0}{n^2}\mathbf{D}. \quad (\text{A.10})$$

Physical interpretation of this equation begins by evaluating the components along the three principal directions. Using the j th component and multiplying both sides by k_j , an eigenvalue equation is developed,

$$\frac{k_j}{k^2}(\mathbf{k} \cdot \mathbf{E}) = \left(1 - \frac{c^2\mu_0\epsilon_j}{n^2}\right) E_j. \quad (\text{A.11})$$

Using the relation $c^2 = (\mu_0 \epsilon_0)^{-1}$, this equation can be simplified to

$$(\mathbf{k} \cdot \mathbf{E}) \frac{k_j^2}{k^2 \left(1 - \frac{\epsilon_j}{n^2 \epsilon_0}\right)} = k_j E_j. \quad (\text{A.12})$$

Since $\mathbf{k} \cdot \mathbf{E} \neq 0$, the vector product the above equation can be divided out and n^2 removed to obtain

$$\sum_{j=1}^3 \frac{k_j^2}{k^2 \left(n^2 - \frac{\epsilon_j}{\epsilon_0}\right)} = \frac{1}{n^2}. \quad (\text{A.13})$$

Defining the principal refractive index to be

$$n_j^2 = \frac{\epsilon_j}{\epsilon_0}, \quad (\text{A.14})$$

equation (A.13) can be rewritten in the form called *Fresnel's equation* [115],

$$\sum_{j=1}^3 \frac{k_j^2}{k^2 (n^2 - n_j^2)} = \frac{1}{n^2}. \quad (\text{A.15})$$

APPENDIX B Definition of Roughness

Roughness is a measure of the topographic relief of a surface. Examples of surface relief include scratches, polishing marks on optical surfaces, machining marks, grains of magnetic materials on memory disks, undulations on silicon wafers, or marks left by rollers on sheet stock. Two quantities describing the rough surface are root-mean-square (rms) roughness and correlation lengths (surface spatial wavelengths). The rms roughness determines the surface height variations measured from a mean surface level whereas the correlation length is the separation between similar features on surface, as shown in Figure B.1.

Rough surfaces are a product of scratches, digs, polishing marks, and machining marks. Scratches are present on most surfaces, and apart from improper handling, are produced by surface finishing operations. Scratches can have widths as large as $10\ \mu m$ or as small as a few tenths of a micrometer. Digs are pits remaining on surfaces that have been ground and subsequently polished. The grinding process produces irregular chips that are later removed by polishing which may also introduce tiny scratches over the surface. If an object is machined by a lathe or milling machine, the surface will show marks of the cutting tool. For sheet metal, the stock is formed by rolling between polished hardened rollers which may leave its marks on the surface of the pressed metal.

Even under the best of conditions, surfaces are always covered with dust which can be in the form of fine particles of sand or hair materials, lint from clothes, or even fine particles left from evaporating water vapor or cleaning agents. The size of dust particles can range from several micrometers down to a few angstroms also contributing to the roughness of the surface [129].

To determine the amount of scattering from a material and its angular distribution, there needs to be a well-validated theory to predict scattering from surfaces. The main statistical quantities used in characterizing smooth surfaces are the root-mean-square roughness, average roughness, and root-mean-square slope.

The most important and most used statistical parameter is the root-mean-square (rms) roughness. The mean surface line is determined by requiring the area of the surface above and below this line to be equal, seen in Figure B.1. The surface height variations are then measured from this line in the $\pm z$ direction and the rms roughness for N discrete, equally spaced, measured points is determined by

$$\text{rms} = \sqrt{\frac{1}{N} \sum_{i=1}^N z_i^2}. \quad (\text{B.16})$$

The mean surface level must be calculated in order to define the rms surface roughness. If the surface is wavy, i.e., has roughness components of long surface spatial wavelength, the value calculated for the rms roughness will in general depend on the length L used for the calculation. Further, if the data points represent the averages of height variations over small areas on the surface, the rms values will depend on the size of the areas. For these reasons, there is no unique rms roughness value for a surface.

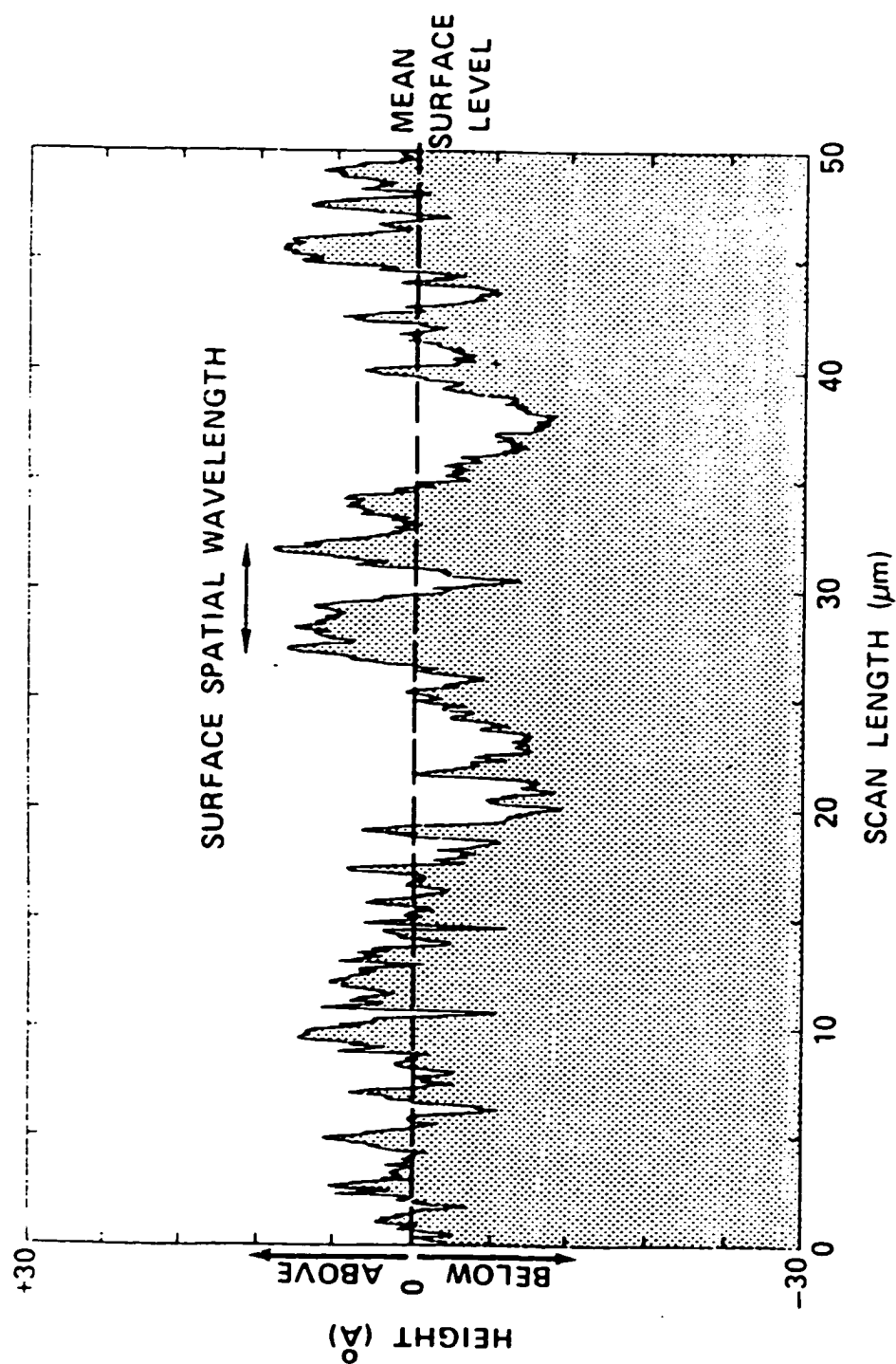


Figure B.1. Schematic representation of a rough surface [129].

Although the rms roughness is generally used to describe the finish of optical surfaces, the average roughness, R_a , is used for machined surfaces. R_a is the average of the absolute values of the surface heights z_i measured from the mean surface level expressed as

$$R_a = \frac{1}{N} \sum_{i=1}^N |z_i|. \quad (\text{B.17})$$

If the surface has a profile that contains no large deviations from the mean surface level, the values of rms and R_a will be similar. However, if there are appreciable numbers of large “bumps” or “holes,” the larger values of the measured heights will dominate the surface statistics making rms larger than R_a .

Generally there is more interest in the slopes of the surface features because they help define the local angle of incidence. When the height data have been measured relative to the mean surface level, the rms slope is defined as the square root of the mean of the squares of the slopes. Each slope is the difference between the heights of the adjacent points divided by the data sampling interval,

$$m = \sqrt{\frac{1}{N} \sum_{i=1}^N m_i^2} \quad (\text{B.18})$$

where

$$m_i = \frac{(z_{i+1} - z_i)}{\tau_0} \quad (\text{B.19})$$

and τ_0 is the (constant) difference between the data points measured along the mean surface level. If the surface is a mathematically smooth, continuous function, the surface slope is the tangent to the surface at all points. The rms slope would then be a unique, well-defined quantity for a profile of length L as long as the profile had a uniquely defined first derivative at every point [129].

APPENDIX C Derivation of the Thermoelastic Equation

The field of continuum mechanics is governed by three conservation laws – conservation of mass, momentum, and energy. Solid mechanics also abides by these laws with the additional constitutive law relating stresses to strains and temperature. For a Hookean material under a small deformation in comparison with the dimension of the object, the Law of Conservation of Mass is written as

$$\rho = \rho_0 \quad (C.20)$$

where ρ and ρ_0 are the strained and unstrained densities of the material respectively.

The Conservation of Momentum takes the form

$$\sigma_{ij,j} = -\rho_0 F_i \quad (C.21)$$

where σ_{ij} is the stress tensor and F_i is the body force per unit mass. Incorporating equations (C.1) and (C. 2) yields the Conservation of Energy

$$\rho_0 (\dot{U} - \dot{R}) = \sigma_{ij} \dot{\epsilon}_{ij} - Q_{i,i} \quad (C.22)$$

where \dot{U} is the rate of change of internal energy per unit mass, $\dot{\epsilon}_{ij}$ is the strain rate, \dot{R} is the rate of heat produced per unit mass by internal heat sources, and Q_i is the heat flux through the surface of the body whose outward directed normal is n_i . The material

response is defined as the Constitutive Law written as

$$\sigma_{ij} = 2\mu\epsilon_{ij} + (\lambda\epsilon_{kk} - \beta\Delta T)\delta_{ij} \quad (\text{C.23})$$

and

$$\beta = (3\lambda + 2\mu)\alpha, \quad \Delta T = T - T_0, \quad (\text{C.24})$$

where α is the coefficient of linear thermal expansion, λ and μ are Lamé constants, T_0 is the stress-free temperature, and δ_{ij} is the Kronecker delta. Equation (4) is generally known as the Duhamel-Neumann Law.

The above laws, together with the conditions of compatibility and boundary conditions, completely describe the system. The temperature, T , and either the stress, σ_{ij} , or the strain, ϵ_{ij} , but not both in equation (C.4) may be specified arbitrarily. The following will treat T and ϵ_{ij} as independent variables.

The Helmholtz free energy equation is written as

$$\Phi = U - TS \quad (\text{C.25})$$

where S is the specific entropy. For an elastic material Φ and S depend only on T and ϵ_{ij} so that

$$\dot{\Phi} = \frac{\partial \Phi}{\partial \epsilon_{ij}} \dot{\epsilon}_{ij} + \frac{\partial \Phi}{\partial T} \dot{T} = \dot{U} - T\dot{S} - S\dot{T}. \quad (\text{C.26})$$

Substituting equation (C.7) into equation (C.3), we obtain

$$\left(\rho_0 \frac{\partial \Phi}{\partial \epsilon_{ij}} - \sigma_{ij} \right) \dot{\epsilon}_{ij} + \rho_0 \left(\frac{\partial \Phi}{\partial T} + S \right) \dot{T} + \left\{ \rho_0 (T\dot{S} - \dot{R}) + Q_{i,i} \right\} = 0. \quad (\text{C.27})$$

For a reversible process, the second law of thermodynamics requires that

$$Q_{i,i} = \rho_0 (\dot{R} - T\dot{S}). \quad (\text{C.28})$$

This leads to the vanishing of the third term in equation (C.8) and the remaining terms independent of $\dot{\epsilon}_{ij}$ and \dot{T} ,

$$\sigma_{ij} = \rho_0 \frac{\partial \Phi}{\partial \epsilon_{ij}} \quad (\text{C.29})$$

and

$$S = -\frac{\partial \Phi}{\partial T}. \quad (\text{C.30})$$

From equations (C.10) and (C.11) it follows that

$$\dot{S} = -\frac{\partial^2 \Phi}{\partial \epsilon_{ij} \partial T} \dot{\epsilon}_{ij} - \frac{\partial^2 \Phi}{\partial T^2} \dot{T} = -\frac{1}{\rho_0} \frac{\partial \sigma_{ij}}{\partial T} \dot{\epsilon}_{ij} - \frac{\partial^2 \Phi}{\partial T^2} \dot{T}. \quad (\text{C.31})$$

Substituting equation (C.12) into equation (C.9) yields

$$Q_{i,i} = T \left(\frac{\partial \sigma_{ij}}{\partial T} \dot{\epsilon}_{ij} + \rho_0 \frac{\partial^2 \Phi}{\partial T^2} \dot{T} \right) + \rho_0 \dot{R}. \quad (\text{C.32})$$

It is customary to define a specific heat under constant strain C_ϵ such that for $\dot{\epsilon}_{ij} = 0$

$$\rho_0 C_\epsilon \dot{T} = -Q_{i,i} \quad (\text{C.33})$$

which by setting $\dot{\epsilon}_{ij} = 0$ in equation (C.13) we get

$$C_\epsilon = -\frac{\partial^2 \Phi}{\partial T^2} T. \quad (\text{C.34})$$

Hence, equation (C.13) maybe written as

$$Q_{i,i} = T \frac{\partial \sigma_{ij}}{\partial T} \dot{\epsilon}_{ij} - \rho_0 C_\epsilon \dot{T} + \rho_0 \dot{R}. \quad (\text{C.35})$$

Assuming the material properties are general functions of temperature, differentiating the constitutive law with respect to temperature yields

$$\frac{\partial \sigma_{ij}}{\partial T} = 2 \frac{\partial \mu}{\partial T} \epsilon_{ij} + \left(\frac{\partial \lambda}{\partial T} \epsilon_{kk} - \frac{\partial \beta}{\partial T} \delta T - \beta \right) \delta_{ij}. \quad (\text{C.36})$$

This derivation differs from Kelvin's approach where he assumed the elastic and thermal properties are constant where in reality they are strong functions of

temperature. Upon substituting equation (C.17) into equation (C.16),

$$Q_{i,i} = T \left[\left(\frac{\partial \lambda}{\partial T} \epsilon_{kk} - \frac{\partial \beta}{\partial T} \delta T - \beta \right) \delta_{ij} + 2 \frac{\partial \mu}{\partial T} \epsilon_{ij} \right] \dot{\epsilon}_{ij} - \rho_0 C_\epsilon \dot{T} + \rho_0 \dot{R}. \quad (C.37)$$

In the case of a stress-induced temperature field in which δT is extremely small, an order of magnitude analysis shows that while $\frac{\partial \beta}{\partial T} \delta T$ may be considered negligible compared to β , the terms $\frac{\partial \lambda}{\partial T} \epsilon_{kk}$ and $\frac{\partial \mu}{\partial T} \epsilon_{ij}$ can be of significant order. Assuming adiabatic conditions, with no internal heat sources, equation (C.18) can be rewritten as

$$\rho_0 C_\epsilon \frac{\dot{T}}{T} = \left[\left(\frac{\partial \lambda}{\partial T} \epsilon_{kk} - \frac{\partial \beta}{\partial T} \delta T - \beta \right) \delta_{ij} + 2 \frac{\partial \mu}{\partial T} \epsilon_{ij} \right] \dot{\epsilon}_{ij} \quad (C.38)$$

in terms of strain or

$$\begin{aligned} \rho_0 C_\epsilon \frac{\dot{T}}{T} = & - \left[\alpha + \left(\frac{\nu}{E^2} \frac{\partial E}{\partial T} - \frac{1}{E} \frac{\partial \nu}{\partial T} \right) \sigma_{kk} \right] \dot{\sigma}_{kk} \\ & + \left(\frac{(1+\nu)}{E^2} \frac{\partial E}{\partial T} - \frac{1}{E} \frac{\partial \nu}{\partial T} \right) \sigma_{ij} \dot{\sigma}_{ij} \end{aligned} \quad (C.39)$$

where E is Young's Modulus, ν is Poisson's ratio, and σ_{kk} is the first stress invariant.

Equation (C.20) is the statement of the thermoelastic effect relating the temperature field and the stress field.

The classical thermoelastic theory expression relating the sum of the principal stress amplitudes with the temperature change ΔT is written as

$$\Delta \sigma = - \frac{1}{K} \frac{\Delta T}{T_0} \quad (C.40)$$

where

$$K = \frac{\alpha}{\rho_0 C_\epsilon}, \quad (C.41)$$

and is called the thermoelastic constant. For small temperature changes, it is assumed that K is independent of the applied stress. But research has shown that K is strain dependent. Considering the case of uniaxial loading where $\sigma_1 = s$ and $\sigma_2 = \sigma_3 = 0$

and $\dot{\sigma}_1 = \dot{s}$ and $\dot{\sigma}_2 = \dot{\sigma}_3 = 0$. Equation (C.20) becomes

$$\rho_0 C_\epsilon \frac{\dot{T}}{T} = - \left(\alpha - \frac{1}{E^2} \frac{\partial E}{\partial T} s \right) \dot{s}. \quad (\text{C.42})$$

Assuming that both temperature and stress fluctuations are small compared to their mean values (T_0 and s_m), equation (C.23) may be linearized to give

$$\rho_0 C_\epsilon \frac{\Delta T}{T_0} = - \left(\alpha - \frac{1}{E^2} \frac{\partial E}{\partial T} s_m \right) \Delta s. \quad (\text{C.43})$$

It can be concluded through the comparison of equations (C.23) and (C.21) that the thermoelastic “constant” can be written in the form

$$K = \left(\alpha - \frac{1}{E^2} \frac{\partial E}{\partial T} s_m \right) (\rho_0 C_\epsilon)^{-1} \quad (\text{C.44})$$

which is stress depended as shown by experiment [130].

BIBLIOGRAPHY

- [1] J. E. Gordon, *Structures – or Why Things Don't Fall Down* (Da Capos Press, Inc, New York 1978).
- [2] David Brewster, "On the Laws which Regulate the Polarization of Light by Reflexion from Transparent Bodies," *Philosophical Transactions of the Royal Society of London*, pp. 125-159 (1815).
- [3] David Brewster, "On the Effects of Simple Pressure in Producing that Species of Crystallization which forms Two Oppositely Polarized Images and Exhibits the Complementary Colours by Polarized Light," *Philosophical Transactions of the Royal Society of London*, pp. 60-64 (1815).
- [4] David Brewster, "On the Communication of the Structure of Doubly Refracting Crystals to Glass, Muriate of Soda, Fluor Spar, and Other Substances, by Mechanical Compression and Dilation," *Philosophical Transactions of the Royal Society of London*, pp. 156-78 (1816).
- [5] David Brewster, "On the Production of Regular Double Refraction in the Molecules of Bodies by Simple Pressure: with Observations on the Origin of the Doubly Refracting Structure," *Philosophical Transactions of the Royal Society of London*, pp. 87-97 (1830).
- [6] David Brewster, "On the Production of Crystalline Structure in Crystallised Powders by Compression and Traction," *Transactions of the Royal Society, Edinburgh*, **20**, pp. 555-9 (1853).
- [7] James Clark Maxwell, "On the Equilibrium of Elastic Solids," *Transactions of the Royal Society, Edinburgh*, **20**, pp. 87-120 (1853).
- [8] L. N. G. Filon, "On the Dispersion in Artificial Double Refraction," *Philosophical Transactions of the Royal Society of London A*, **207**, pp. 263-306 (1907).
- [9] John Kerr, "Experiments on the Birefringent Action of Strained Glass," *Philosophical Magazine*, **26**, pp. 321-342 (1888).
- [10] E. G. Coker and S.P. Thompson, "The Design and Construction of Large Polariscopes," *Engineering*, **94**, pp. 134-135 (July 1912).
- [11] Alexander Goetz, "A Modified Optical Arrangement for Photoelastic Measurements," *Review of Scientific Instruments*, **5**, p. 20 (1934).
- [12] H.T. Jessop, "The Development of Photoelasticity in Britian," *Schweitzer Archiv*, No. 5, pp. 158-163 (May 1959).
- [13] Raymond D. Mindlin, "A Reflection Polariscopes for Photoelastic Analysis," *Review of Scientific Instruments*, **5**, pp. 224-228 (1934).

- [14] H.E. Wessman, "New Universal Straining Frame Aids Photoelastic Research," *Civil Engineering*, **8**, p. 614 (1938).
- [15] S. Redner, "New Automatic Polariscopes System," *Experimental Mechanics*, **14**, pp. 486-491 (Dec 1974).
- [16] C. P. Burger and A.S. Voloshin, "A New Instrument for Whole-Field Stress Analysis," *ISA Transactions*, **22**, pp. 85-95 (1983).
- [17] E. A. Patterson, "Automated Photoelastic Analysis," *Strain*, **24**, pp. 15-20 (Feb 1988).
- [18] Masayoshi Yamada, "High-Sensitive Computer-Controlled Infrared Polariscopes," *Review of Scientific Instruments*, **64**, pp. 1815-1821 (1993).
- [19] M. Fukuzawa and M. Yamada, "Birefringence Induced by Residual Strain in Optically Isotropic III-V Compounds Crystals," *Proceedings of SPIE-The International Society for Optical Engineering*, **2873**, pp. 250-253 (1997).
- [20] H. Lee and S. Krishnaswamy, "A Compact Polariscopes/Shearing Interferometer for Mapping Stress Fields in Bimaterial Systems," *Experimental Mechanics*, **36**, pp. 404-411 (December 1996).
- [21] Yasushi Niitsu, Kenji Gomi, and Kensuke Ichinose, "Development of Scanning Stress Measurement Methods Using Laser Photoelasticity," *JSME International Journal*, **40A**, pp. 143-148 (1997).
- [22] E. Liasi, W. North, P.I. Makrygiannis, T. Rocheleau, and G. Womack, "Photoelasticity Using Retroreflection," *Experimental Techniques*, **21**, pp. 17-19 (Jan/Feb 1997).
- [23] D. E. P. Hoy, "A Color Scanner as a Digital Recording Polariscopes," *Experimental Techniques*, **22**, pp. 26-27 (March/April 1998).
- [24] <http://www.stressphotonics.com>
- [25] A. L. Kimball, Jr., "Stress Determination by Means of the Coker Photo-Elastic Method," *General Electric Review*, pp. 73-81 (Jan 1921).
- [26] L. N. G. Filon, "On the Graphical Determination of Stresses from Photoelastic Observations," *Engineering*, pp. 511-512 (Oct. 19, 1923).
- [27] Ikuzoo Arakawa, "Some Advantages Obtained from Bakelite in Photoelastic Observations," *Proceedings of the Physico-Mathematical Society of Japan*, **7**, pp. 160-180 (1925).
- [28] Raymond D. Mindlin, "A Review of the Photoelastic Method of Stress Analysis I," *Journal of Applied Physics*, **10**, pp. 222-241 (April 1939).
- [29] Raymond D. Mindlin, "A Review of the Photoelastic Method of Stress Analysis II," *Journal of Applied Physics*, **10**, pp. 273-293 (May 1939).
- [30] Max M. Frocht, "Recent Advances in Photoelasticity," *Transactions of ASME*, **53**, pp. 135-153 (1931).

- [31] M. Hetényi, "The Fundamentals of Three Dimensional Photoelasticity," *Journal of Applied Mechanics*, **5**, pp. I149-I155 (1938).
- [32] Raymond D. Mindlin, "Optical Aspects of Three-Dimensional Photoelasticity," *Reprint from the Journal of the Franklin Institute*, **233**, pp. 349-363 (April 1942).
- [33] Daniel C. Drucker and Raymond D. Mindlin, "Stress Analysis by Three-Dimensional Photoelastic Methods," *Reprint from the Journal of Applied Physics*, **11**, pp. 724-732 (November 1940).
- [34] J. H. A. Brahtz and J.E. Soehrens, "Direct Optical Measurement of Individual Principal Stresses," *Journal of Applied Physics*, **10**, pp. 242-247 (April 1939).
- [35] J. Ward, "Recent Developments in Photoelasticity," *Transactions of the Institute of Marine Engineers*, **59**, pp. 223-235 (Dec 1947).
- [36] Raymond D. Mindlin, "Distortion of the Photoelastic Fringe Pattern in an Optically Unbalanced Polariscopes," *Reprint from the Journal of Applied Mechanics*, pp. A170-A178 (December 1937).
- [37] D. C. Drucker, "Photoelastic Separation of Principal Stresses by Oblique Incidence," *Journal of Applied Mechanics*, **65**, pp. A153-A160 (1943).
- [38] Robert M. Gray, "Initial Fringes in Photoelastic Models and Their Effects," *Experimental Stress Analysis*, **11**, pp. 115-118 (1953).
- [39] Max M. Frocht and Roscoe Guernsey, Jr., "Further Work on the General Three-Dimensional Photoelastic Problem," *Journal of Applied Mechanics*, **22**, pp. 183-189 (June 1955).
- [40] F. Zandman and Marc R. Wood, "Photostress: A New Technique for Photoelastic Stress Analysis for Observing and Measuring Surface Strains on Actual Structures and Parts," *Product Engineering*, **27**, pp. 167-178 (1956).
- [41] J. W. Dally and F. J. Ahimaz, "Photographic Method to Sharpen and Double Isochromatic Fringes," *Experimental Mechanics*, **2**, pp. 170-175 (June 1962).
- [42] S. S. Redner, "New Oblique-Incidence Method for Direct Photoelastic Measurement of Principal Strains," *Experimental Mechanics*, **3**, pp 67-72 (March 1963).
- [43] Douglas Bynum, Jr., "On the Accuracy of Fringe Multiplication with Mirrored Birefringent Coatings," *Experimental Mechanics*, **6**, pp. 381-382 (July 1966).
- [44] N. K. DasTalukder and P. Ghosh, "On Fringe Multiplication by Superimposition of Negatives," *Experimental Mechanics*, **15**, pp. 237-239 (June 1975).
- [45] R. K. Müller and L. R. Saackel, "Complete Automatic Analysis of Photoelastic Fringes," *Experimental Mechanics*, **19**, pp. 245-251 (July 1979).
- [46] Toyahiko Yatagai, Suezou Nakadate, Masanori Idesawa, and Hiroyoshi Saito, "Automatic Fringe Analysis Using Digital Image Processing Techniques," *Optical Engineering*, **21**, pp. 432-435 (May/June 1982).
- [47] A. S. Voloshin and C. P. Burger, "Half-fringe Photoelasticity: A New Approach

- to Whole-field Stress Analysis," *Experimental Mechanics* , **23**, pp. 304-313 (Sept 1983).
- [48] A. C. Gillies, "Image Processing Approach to Fringe Patterns," *Optical Engineering*, **27**, pp. 861-866 (October 1988).
 - [49] T. Y. Chen and C. E. Taylor, "Computerized Fringe Analysis in Photomechanics," *Experimental Mechanics*, **29**, pp. 323-329 (Sept 1989).
 - [50] A. S. Voloshin and A. S. Redner, "Automated Measurement of Birefringence: Development and Experimental Evaluation of the Techniques," *Experimental Mechanics*, **29**, pp. 252-257 (Sept 1989).
 - [51] A. J. Durelli and B. Ranganayakamma, "Complementary Use of Photoelasticity with Numerical Methods," *Optical Engineering*, **29**, pp. 154-159 (February 1990).
 - [52] Ph. Boulanger and M. Hayes, "Some Remarks on Photoelasticity," *Arch. Rational Mech. Anal*, **116**, pp. 199-222 (1991).
 - [53] E. A. Patterson and Z. F. Wang, "Towards Full Field Automated Photoelastic Analysis of Complex Components," *Strain*, **27**, pp. 49-56 (May 1991).
 - [54] K. Ramesh, V. R. Ganesan, and S. K. Mullick, "Digital Image Processing of Photoelastic Fringes – A New Approach," *Experimental Techniques*, pp. 41-46 (Sept/Oct 1991).
 - [55] S. J. Haake and E. A. Patterson, "The Determination of Principal Stresses for Photoelastic Data," *Strain* , **28**, pp. 153-158 (Nov 1992).
 - [56] A. Asundi, "Phase Shifting in Photoelasticity," *Experimental Techniques*, pp. 12-23 (Jan/Feb 1993).
 - [57] S. J. Haake, Z. F. Wang, and E. A. Patterson, "Evaluation of Full Field Automated Photoelastic Analysis Based on Phase Stepping," *Experimental Techniques*, pp. 19-25 (Nov/Dec 1993).
 - [58] J. Carazo-Alvarez, S. J. Haake, and E. A. Patterson, "Completely Automated Photoelastic Fringe Analysis," *Optics and Lasers in Engineering*, **21**, pp. 133-149 (1994).
 - [59] Z. F. Wang and E. A. Patterson, "Use of Phase-Stepping with Demodulation and Fuzzy Sets for Birefringence Measurements," *Optics and Lasers in Engineering*, **22**, pp. 91-104 (1995).
 - [60] Y. Morimoto, Y. Morimoto Jr., and T. Hayashi, "Separation of Isochromatics and Isoclinics using Fourier Transform," *Experimental Techniques*, pp. 13-17 (Sept/Oct 1994).
 - [61] B. Han and L. Wang, "Isochromatic Fringe Sharpening and Multiplication," *Experimental Techniques*, pp. 11-13 (Nov/Dec 1994).
 - [62] Jaime F. Cardenas-Garela, Javad Hashemi, and Augusto J. Durelli, "The Practical Use of the Hole Method in Photoelasticity," *Mechanical Research Communica-*

- tions, **22**, pp. 239-244 (1995).
- [63] C. Quan, P. J. Bryanston-Cross, and T. R. Judge, "Photoelastic Stress Analysis Using Carrier and Fast Fourier Techniques," *Optics and Lasers in Engineering*, **18**, pp. 79-108 (1993).
 - [64] N. Plouzenec, J. C. Dupre, and A. Lagarde, "Whole Field Determination of Isoclinic and Isochromatic Parameters," *Experimental Techniques*, **23**, pp. 30-33 (January/February 1999).
 - [65] A. Ajovalasit, S. Barone, and G. Petrucci, "Towards RGB Photoelasticity: Full-Field Automotive Photoelasticity in White Light," *Experimental Mechanics*, **35**, pp. 193-200 (September 1995).
 - [66] K. Ramesh and Sanjeev S. Deshmukh, "Three Fringe Photoelasticity – Use of Colour Image Processing Hardware to Automate Ordering of Isochromatics," *Strain*, **32**, pp. 79-86 (Aug 1996).
 - [67] S. J. Haake, E. A. Patterson, and Z. F. Wang, "2D and 3D Separation of Stresses using Automated Photoelasticity," *Experimental Mechanics*, **35**, pp. 269-276 (September 1996).
 - [68] B. Han and A. L. Wang, "Isochromatic Fringe Sharpening and Interpolation along an Isoclinic Contour, with Application to Fracture Mechanics," *Experimental Mechanics*, **36**, pp. 305-311 (December 1996).
 - [69] Sherri A. Sparling and Carolyn F. Small, "Photoelastic Analysis Using Chromatic Interpretation of Digitized Video," *1995 IEEE Engineering in Medicine and Biology: 17th Annual Conference*, **1**, pp. 417-418 (1997).
 - [70] E. A. Patterson, W. Ji, and Z. F. Wang, "On Image Analysis for Birefringence Measurements in Photoelasticity," *Optics and Lasers in Engineering*, **28**, pp. 17-36 (September 1997).
 - [71] Andrew D. Nurse, "Full-Field Automated Photoelasticity by Use of a Three-Wavelength Approach to Phase Stepping," *Applied Optics*, **36**, pp. 5781-5786 (August 1997).
 - [72] T. W. Ng, "Photoelastic Stress Analysis Using an Object Step-Loading Method," *Experimental Mechanics*, **37**, pp. 137-141 (June 1997).
 - [73] M. J. Ekman and A. D. Nurse, "Absolute Determination of the Isochromatic Parameter by Load-stepping Photoelasticity," *Experimental Mechanics*, **38**, pp. 189-195 (September 1998).
 - [74] K. Ramesh and S. S. Deshmukh, "Automation of White Light Photoelasticity by Phase Shifting Technique Using Color Image Processing Hardware," *Optics and Lasers in Engineering*, **28**, pp. 47-60 (September 1997).
 - [75] T. Y. Chen, "Digital Determination of Photoelastic Birefringence Using Two Wavelengths," *Experimental Mechanics*, **37**, pp. 232-236 (September 1997).
 - [76] G. Petrucci, "Full-Field Automatic Evaluation of an Isoclinic Parameter in White

- Light," *Experimental Mechanics*, **37**, pp. 420-426 (December 1997).
- [77] W. Ji and E. A. Patterson, "Simulations of Errors in Automated Photoelasticity," *Experimental Mechanics*, **38**, pp. 132-139 (June 1998).
 - [78] J. Gough, "A Description of a Property of Indian Rubber (Caoutchouc)," *Manchester Literary and Philosophical Society* (1805).
 - [79] *Thermoelastic Stress Analysis*, N. Harwood and W. M. Cummings, Eds. (Adam Hilger, Bristol, 1991).
 - [80] W. Thomson, "On the Dynamic Theory of Heat with Numerical Results Deduced from Mr. Joule's Equivalent of a Thermal Unit," *Transactions of the Royal Society of Edinburgh*, pp. 261-288 (1853).
 - [81] K. T. Compton and D. B. Webster, "Temperature Changes Accompanying the Adiabatic Compression of Steel," *Adiabatic Compression of Steel*, **5**, pp. 159-166 (1915).
 - [82] Clarence Zener, "Internal Friction in Solid – General Theory of Thermodynamic Internal Friction," *Physical Review*, **53**, pp. 90-99 (January 1, 1938).
 - [83] M. A. Biot, "Thermoelasticity and Irreversible Thermodynamics," *Journal of Applied Physics*, **27**, pp. 240-253 (1956).
 - [84] Milo H. Belgen, "Structural Stress Measurements with an Infrared Radiometer," *ISA Transactions*, **6**, pp. 49-53 (January 1967).
 - [85] Milo H. Belgen, "Infrared Radiometric Stress Instrumentation Application Range Study," NASA CR-1067 (1968).
 - [86] E. H. Jordan and B. I. Sandor, "Stress Analysis from Temperature Data," *Journal of Testing and Evaluation*, **6**, pp. 325-331 (November 1978).
 - [87] D. S. Mountain and J. M. B. Webber, *Proceedings of the Society of Photo-Optical Instrument Engineering*, **164**, pp. 189-196 (1978).
 - [88] L. R. Baker and J. M. B. Webber, "Thermoelastic Stress Analysis," *Optica Acta*, **29**, pp. 555-563 (1982).
 - [89] C. S. Welch, K. E. Cramer, J. R. Lesniak, and B. R. Boyce, "An Array Measurement System for Thermoelastic Stress Analysis," *Nontraditional Methods of Sensing Stress, Strain, and Damage in Materials and Structures*, George F. Lucas and David A. Stubbs, Eds., pp. 198-206 (American Society for Testing and Materials, 1997).
 - [90] J. McKelvie, "Consideration of the Surface Temperature Response to Cyclic Thermoelastic Heat Generation," *SPIE Stress Analysis by Thermoelastic Techniques*, **731**, pp. 44-53 (1987).
 - [91] T. G. Ryall and A. K. Wong, "Determining Stress Components from Thermoelastic Data – A Theoretical Study," *Mechanics of Materials*, **7**, pp. 205-214 (1988).
 - [92] Y. M. Huang, H. H. AbdelMohsen, and R. E. Rowlands, "Determination of Indi-

- vidual Stresses Thermoelastically," *Experimental Mechanics*, **30**, pp. 88-94 (1990).
- [93] Y. M. Huang, R. E. Rowlands, and J. R. Lesniak, "Simultaneous Stress Separation, Smoothing of Measured Thermoelastic Isopachic Information and Enhanced Boundary Data," *Experimental Mechanics*, **30**, pp. 398-403 (1990).
 - [94] Y. M. Huang and R. E. Rowlands, "Quantitative Stress Analysis Based on the Measured Trace of the Stress Tensor," *Journal of Strain Analysis for Engineering Design*, **26**, pp. 55-63 (1991).
 - [95] Jon Lesniak, *Thermographic Stress Analysis/NDE via Focal-Plane-Array Detectors*, Final Report, Contract Number NAS1-19262 (1991).
 - [96] J. Lesniak and B. Bartel, "An Elevated-Temperature TSA Furnace Design," *Experimental Techniques*, **20**, pp. 10-13 (March/April 1996).
 - [97] S. T. Lin, J. P. Miles, and R. E. Rowlands, "Image Enhancement and Stress Separation of Thermoelastically Measured Data Under Random Loading" *Experimental Mechanics*, **37**, pp. 225-231 (September 1997).
 - [98] B. J. Rauch and R. E. Rowlands, "Filtering Thermoelastically Measured Isopachic Data," *Experimental Mechanics*, **37**, pp. 387-392 (December 1997).
 - [99] S. Offermann, J. L. Beaudoin, C. Bissieux, and H. Frick, "Thermoelastic Stress Analysis Under Nonadiabatic Conditions," *Experimental Mechanics*, **37**, pp. 409-413 (December 1997).
 - [100] J. M. Dulieu-Barton and P. Stanley, "Reproducibility and Reliability of the Response from Four SPATE Systems," *Experimental Mechanics*, **37**, pp. 440-444 (December 1997).
 - [101] A. J. Durelli and K. Rajaiah, "Determination of Strains in Photoelastic Coatings," *Experimental Mechanics*, **20**, pp. 57-64 (1980).
 - [102] "Separation of Principal Strains," Operating Instructions and Technical Manual for the 030-Series Reflection Polariscopes, Measurements Group, Inc., Raleigh, North Carolina.
 - [103] S. Barone and E. A. Patterson, "Full-field Separation of Principal Stresses by Combined Thermo- and Photoelasticity," *Experimental Mechanics*, **36**, pp. 318-324 (1996).
 - [104] R. B. Agarwal and L. W. Teufel, "Epon 828 Epoxy: A New Photoelastic-Model Material," *Experimental Mechanics*, **23**, pp. 30-35 (1983).
 - [105] *Polymer Materials: An Introduction for Technologists and Scientists*, Christopher Hall, Ed. (John Wiley & Sons, New York, 1989).
 - [106] Francoise Delplancke, Harry Sendrowicz Robert Bernaerd, and Jean Ebbeni, "Simple Process for Building Homogeneous Adaptable Retarders made from Polymeric Materials," *Applied Optics*, **34**, pp. 2921-2926 (June 1, 1995).
 - [107] Alexander K. Mackenzie, "Effects of Surface Coatings on Infra-red Measurements

- of Thermoelastic Responses,” *SPIE*, **1084**, pp. 59-71 (1989).
- [108] “Principal Stress Separation in PhotoStress Measurements,” Measurements Group, Inc. Tech Note TN-708-1 (1992).
 - [109] Christopher S. Welch and Michael J. Zickel, “Thermal Coating Characterization Using Thermoelasticity,” *Review of Progress in Quantitative Nondestructive Evaluation*, **12B**, pp. 1923-1930 (1993).
 - [110] S. Barone and E. A. Patterson, “Polymer Coating as a Strain Witness in Thermoelasticity,” *Journal of Strain Analysis*, **33**, pp. 223-232 (1998).
 - [111] *Handbook on Structural Testing*, R.T. Reese and W.A. Kawahara, Eds. (Fairmount Press, Liburn, GA, 1993).
 - [112] “Instructions for Bonding Flat and Contoured Photoelastic Sheets to Test-Part Surfaces,” Instruction Bulletin IB-223-G (Measurements Group, Inc., 1982).
 - [113] W. E. Witzell, “Photostress Spray Technique Development,” REA 111-9133, Report No. ERR-AN-027 (1961).
 - [114] “Introduction to Stress Analysis by the Photostress[®] Method,” Measurements Group Tech Note TN-702-1 (Measurements Groups, Inc., Raleigh, North Carolina, 1989).
 - [115] Robert Guenther, *Modern Optics*, (John Wiley & Sons, Inc., New York, 1990).
 - [116] Jin Au Kong, *Electromagnetic Wave Theory*, Second Edition (John Wiley & Sons, Inc., New York, 1990).
 - [117] J. A. Brandão Farla, “A Perturbation Approach to the Analysis of Index Ellipsoid Deformations in Biaxial and Uniaxial Media,” *Microwave and Optical Technology Letter*, **6**, pp. 657-670 (1993).
 - [118] Y. C. Fung, *A First Course in Continuum Mechanics*, Third Edition (Prentice Hall, Englewood Cliffs, 1994).
 - [119] K. Elliott Cramer, David S. Dawicke, and Christopher S. Welch, “Thermographic Characterization of Stress During Crack Growth,” *Review of the Progress of Quantitative Nondestructive Evaluation*, **11**, pp. 2139-2146 (Plenum Press, New York, 1992).
 - [120] *DeltaTherm User’s Guide* (Stress Photonics Inc. Madison, WI, March 1998).
 - [121] “Calibration of Photoelastic Coatings,” Measurements Group Tech Note TN-701 (Measurements Groups, Inc., Raleigh, North Carolina, 1977).
 - [122] N. Plouzenec, J.C. Dupré, and A. Lagarde, “Whole Field Determination of Isoclinic and Isochromatic Parameters,” *Experimental Techniques*, **23**, pp. 30-33 (January/February 1999).
 - [123] Max Mark Frocht, *Photoelasticity, Volume 1* (John Wiley & Sons, New York, 1941).
 - [124] Petr Beckmann, *The Depolarization of Electromagnetic Waves* (The Golem Press,

Boulder, Colorado, 1968).

- [125] Petr Beckmann and André Spizzichino, *The Scattering of Electromagnetic Waves From Rough Surfaces* (Artech House, Inc., Norwood, MA, 1987).
- [126] Deonna Woolard and Mark Hinders, "Stress Separation Errors Resulting from Imperfect Backings," *Proceedings of SEM Annual Conference on Theoretical, Experimental, and Computational Mechanics*, pp. 605-608 (SEM 1999).
- [127] D. F. Woolard and M. K. Hinders, "Coating for Combined Thermoelastic and Photoelastic Stress Measurement," *Nondestructive Evaluation of Bridges and Highways III*, Steven B. Chase, Editor, Proceedings of SPIE, **3587**, pp. 88-96 (1999).
- [128] Deonna Woolard, Mark Hinders, and Christopher Welch, "Combined Thermoelastic and Photoelastic Full-Field Stress Measurement," *Review of Progress in Quantitative Nondestructive Evaluation*, **18**, pp. 1431-1438 (Plenum Press, New York, 1999).
- [129] Jean M. Bennett and Lars Mattsson, *Introduction to Surface Roughness and Scattering* (Optical Society of America, Washington, D.C., 1989).
- [130] A. K. Wong, R. Jones, and J. G. Sparrow, "Thermoelastic Constant of Thermoelastic Parameter," *Journal of Physical Chemistry in Solids*, **48**, pp. 749-753 (1987).

Vita

Deonna Faye Woolard

Born in Weirton, West Virginia, on November 27, 1969 to Diane and William C. Johnson. Was the Salutatorian of the 1988 graduating class from Weir High School, Weirton, West Virginia. Graduated *Magna Cum Laude* from Bethany College, Bethany, West Virginia with a Bachelor of Science in Physics, May 1992. Received her Masters Degree in Physics from the College of William and Mary, Williamsburg, Virginia in December 1994 and her Doctorate of Philosophy from the same institution in December 1999. She has accepted a tenure-track assistant professor position in the Department of Physics at Randolph-Macon College, Ashland, Virginia.